Superprotonic Solid Acid Phase Transitions and Stability

Thesis by

Lisa Cowan

In Partial Fulfillment of the Requirements

for the Degree of

Doctor of Philosophy

California Institute of Technology

Pasadena, California

2007

(Defended May 9, 2007)

Acknowledgements

I have a large debt of gratitude owed to many people and I would like to let this section serve as an account of this indebtedness. I hope to return these favors and to emulate the nurturing spirit that surrounded me while at Caltech.

I would like to thank my advisor, Dr. Sossina Haile, for all of her guidance and support that allowed me to complete work I could be proud of with the freedom to find my own path. I will miss looking over puzzling data with her as she always had suggestions that would lead us to a cohesive explanation.

I have been very fortunate to have many great collaborators. I would like to sincerely thank Dr. Thomas Proffen for his help at Los Alamos, for answering countless emails regarding data analysis and for being a friend. Dr. Sonjong Hwang's friendship and expertise saved me during my last-minute panicked NMR requests which would have ended up in disaster otherwise. Dr. William A Goddard III, Dr. Adri van Duin, Dr. Yun Hee Jang, and Dr. Boris Merinov guided me through QC simulation details and without their help I would never have been able to even dream of doing such work. Dr. Oc Hee Han and Dr. Kee Sung Han of KBSI welcomed me into their lab for a summer and helped me extend my understanding of NMR (funded by NSF EAPSI). I am indebted to Dr. Clare Grey, Dr. Luming Peng and Lesley Holmes at Stony Brook as well as Dr. Steve Greenbaum and Dr. Jay Jayakody at Hunter College for their help on NMR measurements. Dr. Alex Navrotsky and Riham Morcos were invaluable towards acquiring enthalpy data on $Rb_3H(SO_4)_2$ samples and I am honored by their collaboration.

I am thankful for Dr. George Rossman and Liz Miura's help on Raman and IR spectroscopy presented in this work. Dr. Janet Hering's freeze dryer was an essential piece

of equipment for the preparation of my deuterated samples and I greatly appreciate the unlimited access I had to the machine and her students' patience and respect for my work (Dr. Tao Cheng, Rich Wildman, Dr. Tom He, and Arthur Fitzmaurice). I am very appreciative of access to Dr. Jane Raymond's melting point apparatus throughout my Ph.D. I greatly appreciate Richard Gerhart (aka: The Glass Man) and Mike Vondrus (aka: Machinist Extraordinaire) for filling my rushed, frantic orders and providing parts to build my own experimental setup. I am also very grateful for all of the help and friendship from the administrative staff: Fran Matzen, Linda Scott, Irene Loera and Pam Albertson in the materials science department, as well as Tess Legaspi and Gloria Brewster in the registrar's office, Cheryl Hawthorne and Angela Wood in the career development center, and Divina Bautista, Alice Sogomonian, Jeannie Holloway, and Phyllis Belisle in the health center. I would also like to thank Dr. George Rossman, Dr. William Goddard, Dr. Brent Fultz and Dr. Rob Phillips for reading my thesis.

I have had some of the best friends and lab mates possible throughout my graduate and undergraduate years at Caltech. I am lucky to have known and worked with Dr. Wei Lai, Dr. Sundeep Mukherjee, Dr. Peter Babilo, Dr. Stacey Boland, Justin Ho, Dr. Chris Veazey, Dr. Calum Chisholm, Dr. Dane Boysen, Dr. Tetsuya Uda, Mikhail Kislitsyn, Ryan Merle, Merle Rodriguez, Gisela Lentz, Jennifer Mederos, Dr. Mary Thundathil, Kenji Sasaki, Dr. Jian Wu, Dr. Kate Campbell, Dr.^{2} Yvette Tanhehco, Dr. Joanna Dodd, Rebecca Stevens, Dr. Emilio Castano-Graff, Martin Smith-Martinez, Sam Mandegaran, Peijung Tsai, Dr. Channing Ahn, Peter Nguyen, Dr. Fatemeh Jalayer, Dr. Eva Kanso, Dr. Maryam Fazel, Dr. Behnam Analui, Dr. Hossein Hashemi, Pei-Hua Hung, Mary Louie, William Chueh, Dr. Eric Toberer, Dr. Phil Bell, Dr. Sam Davila, and Dr. Jessica Wuu.

Dr. Hany Farid was my mentor in the NASA/Sharp+ summer program at the University of Pennsylvania during the summers of ’95 and ’96. Because his mentorship has shaped my life and helped me appreciate research, I must acknowledge him in my Ph.D. thesis. I am very grateful to have worked with him and the impact of his guidance cannot be overestimated. Thank you, Hany.

I would not have made it this far without the support of my family. I am very grateful for all of my mother’s help and for having her as an inspiration in my life. I would also like to thank my brother and father for their support during my graduate work and especially for teaching me how to use a soldering iron before I knew how to tie my shoes. My boyfriend, Dr. Kazu Suzuki, was especially handy at helping me dry my samples (with a hair dryer, some heat lamps and a heating mantle) for neutron diffraction at 3 a.m. the morning they were to be shipped as well as countless late nights of data analysis and experiments. I could not have done this without you.

Abstract

Solid acid proton conductors are viable alternatives to current fuel cell electrolytes. Incorporating solid acid electrolytes, next generation fuel cells would not require humidification of the electrolyte, as in proton exchange membrane fuel cells, and could operate at higher temperatures which would improve catalysis rates. Engineering the properties of these materials for fuel cell electrolyte applications requires an understanding of the structural and chemical parameters that support superprotonic phase transitions over melting or decomposition.

In this thesis, the structures of three superprotonic solid acids are presented, and for the first time, a distinction is possible between local versus average structure. An adapted model for configurational entropy based on Pauling's entropy rules for ice is incorporated to describe the entropy of superprotonic solid acids. Insights from local structural information alleviate discrepancies between this model and experimentally determined entropy values. With clarifications from this work, the calculated configurational entropy of the superprotonic structures of CsD_2PO_4, $RbDSeO_4$, and $CsDSO_4$, agree well with experimentally determined entropy values.

A study of chemical intermediates, $Cs_xRb_{1-x}H_2PO_4$, provides valuable insight into the nature of the cation size effect on superprotonic phase transitions within an isostructural system. For compounds in the series that do exhibit a superprotonic phase, CsH_2PO_4 – $Cs_{0.3}Rb_{0.7}H_2PO_4$, the magnitude of proton conductivity remains neutral to rubidium incorporation. Altering the effective cation size shows a profound impact on transition temperature for compounds with high rubidium content ($x < 0.5$) while preserving the overall conductivity of the high-temperature and low-temperature phases. X-ray diffraction, thermal analysis, Raman, IR, ^{133}Cs, ^{87}Rb and ^{1}H-NMR spectroscopy all attest to the gradual variation in structural properties across the composition range.

The complicated high-temperature properties of $Rb_3H(SO_4)_2$ have been misinterpreted in earlier literature as a superprotonic phase transition. This work presents a careful analysis of a conglomeration of data from different techniques which definitively conclude that at ambient pressure, $Rb_3H(SO_4)_2$ degrades via phase separation, $Rb_3H(SO_4)_2 \rightarrow RbHSO_4 + Rb_2SO_4$.

Table of Contents

Appendix

List of Figures

List of Tables

Chapter 1 Introduction

The overarching theme of this work is to elucidate the structure of superprotonic solid acids. Structural information delimits the number of configurations available to oxyanion tetrahedra as well as the number of ways hydrogen bonds can form. The overall number of configurations in superprotonic solid acids determines the configurational entropy, and the sampling of these different configurations facilitates the unusually high proton conductivity in these materials. Verifying current models for determining configurational entropy is important to understanding superprotonic solid acid phase transitions. Solid acid phase stability and noteworthy changes in physical parameters prior to the phase transition are also considered.

This chapter will provide a brief explanation of solid acids and superprotonic transitions as well as a method to evaluate configurational entropy, and a summary of noteworthy conclusions from this work.

1.1 Overview of Solid Acids and Superprotonic Phase Transitions

Solid acids are chemical intermediates between normal salts and normal acids.

$$\tfrac{1}{2}\, Cs_2SO_4 \text{ (salt)} + \tfrac{1}{2}\, H_2SO_4 \text{ (acid)} \longrightarrow CsHSO_4 \text{ (solid acid).}$$

Solid acid properties are also intermediate between those of an acid and a salt in that they are brittle and insulating but are known to have high ionic conductivity ($\sim 10^{-2}\ \Omega^{-1}\ \mathrm{cm}^{-1}$). At room temperature, most solid acids are monoclinic in symmetry. At elevated temperatures (~ 100 – 300°C), some solid acids undergo a first-order phase transformation to higher symmetry. In the higher symmetry phase, oxygen and hydrogen atom sites are disordered which allows tetrahedral oxyanion groups to reorient ($\sim 10^{11}$ Hz). Tetrahedral motion facilitates inter-tetrahedral proton hopping ($\sim 10^{9}$ Hz) [1] which leads to high proton conductivity in the disordered high-temperature phase. Across the phase transition from the low-symmetry monoclinic phase to the higher symmetry, disordered phase, proton conductivity increases by several orders of magnitude in superprotonic solid acids.

Fundamental physical and chemical characteristics of solid acids have attracted attention due to interesting changes in the hydrogen bonding network in different phases of these materials. Earlier solid acid studies focused on the ferroelectric to paraelectric phase transition at temperatures below room temperature (e.g., KH_2PO_4, $Cs_3H(SeO_4)_2$). In 1981, the first superprotonic phase transition was discovered in $CsHSO_4$ [2, 3].

Over the past few years, much attention has been focused on the application of these novel materials as electrolytes in next generation fuel cells with the ultimate goal of replacing the combustion engines in automobiles (Figure 1-1). Solid acids have advantages over the conventional proton exchange membrane (PEM) fuel cells. PEM fuel cells require humidification which limits the operating temperature to under 100°C. As solid acids can operate at higher temperatures, catalysis rates would be improved, relative to PEM fuel cells, with the possibility of eliminating the necessity of precious metals altogether. Solid acids are water soluble which is a disadvantage for use in fuel cells that will need to be addressed in solid acid fuel cell systems.

Figure 1-1. The most ambitious application of solid acids is as an electrolyte in a fuel cell that would replace combustion engines in cars. Solid acid electrolytes have advantages over current fuel cell technology (PEM) in that they can operate at higher temperatures and are gas impermeable.

1.2 Background

Configurational Entropy

Configurational entropy of solid acid structures is derived from the number of ways that hydrogen bonds and tetrahedral phosphate, sulfate or selenate groups can orient. A model has been presented which draws on Pauling's Ice Rules and adapts those rules to count the number of configurations in the superprotonic phase [4, 5]. This approach is necessary whenever the orientations of the oxyanion tetrahedral groups are independent of the hydrogen bonds that the group forms.

Chapters 3, 4 and 5 address the configurational entropy of the superprotonic phase of solid acids $CsDSO_4$, $RbDSeO_4$, and CsD_2PO_4, respectively. These three superprotonic structures provide examples in which the selenate tetrahedral orientations are fixed by the location of the hydrogen bonds ($RbDSeO_4$), the sulfate orientations are independent of hydrogen atom positions and hydrogen bonding follows a simple model ($CsDSO_4$), and phosphate orientations and hydrogen bonding are independent but neither are straightforward (CsD_2PO_4). The modified ice rules are necessary to evaluate the number of configurations in the high-temperature phase of $CsDSO_4$ and CsD_2PO_4 while $RbDSeO_4$ does not necessitate this level of sophisticated counting.

To present the modified Ice Rules as they apply to counting the configurations of solid acids in the disordered superprotonic phase, consider $CsDSO_4$. $CsDSO_4$, the simplest case with independent hydrogen bonding and tetrahedral configurations, has been described in three different structures. In Chapter 3, neutron diffraction data identifies one structure, the Jirak model [6], as the best description of the sulfate tetrahedra disorder. For this example, we will consider the number of configurations implied by the Jirak model.

The modified ice rules, as they apply to $CsHSO_4$ are as follows [4]:

(1) one proton is associated with each tetrahedron;
(2) one proton occupies each hydrogen bond that is formed;
(3) hydrogen bonds are directed towards oxygen atoms of neighboring tetrahedra;
(4) interaction between non-neighboring HSO_4 tetrahedra does not influence the distribution of hydrogen bond configurations.

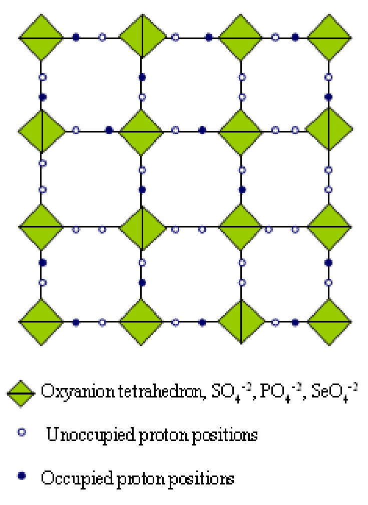

Figure 1-2. Cartoon diagram of tetrahedral orientations and hydrogen bonding in CsHSO4 – Jirak example with two tetrahedral orientations and four hydrogen bonding directions

The Jirak structure describes each sulfate group with four neighboring sulfate groups providing four directions along which hydrogen bonds can be formed. Each sulfate group can reside in one of two orientations, independent of any distribution of hydrogen bonds. Projected onto two dimensions, the structure schematically appears as in Figure 1-2. The number of configurations available to $CsHSO_4$ is the product of the number of hydrogen bond configurations multiplied by the number of sulfate group orientations.

When a hydrogen atom participates in a hydrogen bond in this structure, it has 4 options to choose from with a ¾ probability that the bonding direction (option) is available. The contribution to configurational entropy from hydrogen bonding,

$$\Omega_H = \begin{pmatrix} 4 \\ 1 \end{pmatrix} \left(\frac{3}{4} \right) = 3 \text{ hydrogen bonding configurations.}$$

There are 2 tetrahedral configurations in the Jirak structure which results in an the overall number of configurations,

$$\Omega = \begin{pmatrix} \#of \\ proton \\ configurations \end{pmatrix} \times \begin{pmatrix} probability \\ proton \\ site\, is\, open \end{pmatrix}^{(\#of\ protons)} \times (\#of\ oxygen\, positions)$$

$$\Omega = \Omega_H\ \Omega_{tetradehral} = 3 \times 2 = 6\,.$$

The configurational entropy of this phase,

$$S_{config} = R\ln\Omega = 8.314\frac{J}{mol\,K}\ln(6) = 14.9\frac{J}{mol\,K}\,,$$

is the implied transition entropy because the low-temperature phase is completely ordered ($S_{config} = R\ln 1 = 0$). If the low-temperature phase were disordered, the configurational entropy associated with the low-temperature phase would have to be subtracted off to yield the transition entropy. Other disordered solid acids can be evaluated in a similar fashion adapting ice rule (1) to accommodate the number of protons associated with each tetrahedron.

1.3 Summary of Conclusions

Inconsistencies in the literature surround the high-temperature properties of CsH_2PO_4. The decomposition behavior of the material without proper humidification or efforts to minimize dehydration effects, such as sealing reactor containers, has led researchers to refute the existence of the superprotonic phase transition. This work presents neutron diffraction data that has enabled the assignment of deuterium positions in the structure while providing insight into the local structure of the material through pair distribution function analysis.

This work is the first to present neutron pair distribution function (PDF) analysis of any solid acid material in the superprotonic phase. PDF data was collected on $CsDSO_4$, $RbDSeO_4$, and CsD_2PO_4. The PDF shows a striking loss of long-range correlations in the superprotonic phase, suggesting that despite high crystallinity and mechanical integrity, local superprotonic structure is disordered comparable to a glass. This loss of long-range atom pair correlations is most noticeable in the case of CsH_2PO_4. An approach for determining the configurational entropy of this compound necessitates considering configurations that would not be expected from the average structure description (Bragg diffraction), while configurational entropy discussions on other compounds, $RbDSeO_4$ and $CsDSO_4$, fit within the constructs of the average structure description. Coincidentally, long-range correlations, although reduced in $RbDSeO_4$ and $CsDSO_4$ are not as severely diminished as in the high-temperature phase of CsH_2PO_4.

Debate over the high-temperature structure of $CsDSO_4$ has been resolved utilizing high-resolution neutron powder diffraction data [6-8]. Discussed in Chapter 3, the Jirak structure assigns a single crystallographic oxygen and deuterium position to describe the disorder of the sulfate tetrahedra. The Jirak structure was compared to split deuterium and oxygen models. A Hamilton's test on the significance of refined parameters indicates the additional oxygen and deuterium sites do not improve the refinement. Experimentally measured transition entropy values also agree well with the value of the configurational entropy present in the Jirak structure.

$RbHSeO_4$ high-temperature structure has been identified in the $I4_1/amd$ space group [6-8], discussed in Chapter 4. Despite differences in the low-temperature structure of $RbHSeO_4$ (B1 symmetry) and $CsHSO_4$ ($P2_1/c$ symmetry), the high-temperature phases of these two materials are very similar. Refinement of the $CsHSO_4$ structures (single vs. split site models) against $RbHSeO_4$ neutron diffraction data as well as a Hamilton's test indicate the superprotonic phase of $RbHSeO_4$ is best described in Merinov's split deuterium and split oxygen site model [7]. Experimentally measured transition entropy values agree well with the value of the configurational entropy present in the Merinov structure.

Cation size effects have been observed in solid acid compounds, e.g., CsH_2PO_4 exhibits a superprotonic phase transition while RbH_2PO_4 does not. An increase in cation size is also known to lower the superprotonic phase transition temperature. A generally accepted interpretation of these results is that larger cations provide more space for the sulfate, selenate, phosphate tetrahedral to reorient. Differences in structural transformations and symmetries between different compounds complicate the study of the cation size effect. Chapter 6 presents a study on chemical intermediates $Cs_xRb_{1-x}H_2PO_4$ shown to crystallize in the CsH_2PO_4 structure, $P2_1/m$, for compositions CsH_2PO_4 through $Cs_{0.2}Rb_{0.8}H_2PO_4$. This large composition range maintains the same crystallographic symmetry and allows comparisons of properties to be attributed solely to a difference in average cation size. X-ray diffraction, thermal analysis, Raman, IR, ^{133}Cs, ^{87}Rb and ^{1}H-NMR spectroscopy all attest to the gradual variation in structural properties across the composition range. The limiting effective cation radius for a superprotonic transition for this series has been determined to be $R_{sp} \geq 1.649$ Å.

Solid acid degradation unfortunately can be misconstrued as a superprotonic transition and vice versa. To complicate matters, observing the superprotonic phase prior to decomposition in some cases requires very precise temperature control and patience, e.g., $RbHSeO_4$, superprotonic phase is clearly discernable by powder X-ray diffraction in the narrow temperature range from 170°C – 176°C. The complicated high-temperature properties of $Rb_3H(SO_4)_2$ which are misleading have been misinterpreted in the literature as a superprotonic phase transition [9, 10]. Chapter 7 presents a careful analysis of a conglomeration of data from different techniques which definitively conclude that at ambient pressure, $Rb_3H(SO_4)_2$ phase separates, $Rb_3H(SO_4)_2 \rightarrow RbHSO_4 + Rb_2SO_4$.

1.4 References

1. Munch, W., et al. A Molecular-Dynamics Study of the High-Proton Conducting Phase of $CsHSO_4$. Solid State Ionics, 1995, **77**: 10 – 14.

2. Baranov, A.I., Shuvalov, L. A. Shchagina, N. M. JETP Lett. 1982, **36**: 459 – 462.

3. Komukae, M., et al. Dielectric and Thermal Studies on New Phase-Transitions of $CsHSO_4$. Journal of the Physical Society of Japan, 1981, **50**(10): 3187 – 3188.

4. Chisholm, C.R.I. and S.M. Haile. Entropy Evaluation of the Superprotonic Phase of $CsHSO_4$: Pauling's Ice Rules Adjusted for Systems Containing Disordered Hydrogen-Bonded Tetrahedra. Chemistry of Materials, 2007, **19**(2): 270 – 279.

5. Haile, S.M., et al. Solid Acid Proton Conductors: From Laboratory Curiosities to Fuel Cell Electrolytes. Faraday Discussions, 2007, **134**: 17 – 39.

6. Jirak, Z., et al. A Neutron-Diffraction Study of the Superionic Phase in $CsHSO_4$. Physica Status Solidi a-Applied Research, 1987, **100**(2): K117 – K122.

7. Merinov, B.V. Localization of Hydrogen Atoms in Protonic Conductors with a Dynamical Disordered Network of Hydrogen Bonds: Effect of Anomalous Manifestation of Hydrogen Atoms on Electron-Density Maps. Kristallografiya, 1997, **42**: 906 – 917.

8. Zetterstrom, P. et al. Structure and Proton Conduction in $CsDSO_4$. Solid State Ionics, 1999, **116**(3 – 4): 321 – 329.

9. Lim, A.R., et al. Ferroelastic Domain Switching Behaviors of Superionic Conductor $M_3H(SO_4)_2$ (M=K, Rb, and NH_4) Single Crystals. Journal of Applied Physics, 2006, **99**(5).

10. Suzuki, K. and S. Hayashi, H-1 NMR Study of Proton Dynamics in the Inorganic Solid Acid $Rb_3H(SO_4)_2$. Physical Review B, 2006, **73**(2).

Chapter 2 Experimental Techniques

2.1 Synthesis

Crystalline powder solid acid samples were synthesized by solvent-induced precipitation, evaporating, or freeze drying an aqueous solution containing metal carbonates (approx. 99% purity) or metal sulfates, where appropriate, and the acid of choice:

$$M_2CO_3 + H_nXO_4 + H_2O \xrightarrow{\uparrow H_2O, CO_2} M_aH_b\left(XO_4\right)_c$$

where M = [Cs, Rb, K, Na, Tl, NH_4, $NH_2CH_2CH_2NH_2$] and X = [S, Se, P, As]. Methanol and acetone solvents were used independently to precipitate solid acid samples. Once in solid form, solid acid samples were vacuum filtered over ceramic filters and rinsed with methanol or acetone. In many cases, excess acid was necessary to ensure phase purity. Most synthesis took place under ambient conditions. Whenever single crystal samples were necessary, the aqueous solution of the stoichiometric composition was allowed to evaporate off water slowly, either at ambient conditions or in a refrigerator.

Neutron diffraction studies in this work required deuterated analogs of solid acid samples. Sample deuteration for this work was achieved (> 99% deuteration) by dissolving phase pure solid acid samples in D_2O and then freeze drying the solution. This process was repeated until there was no detectable ^1H NMR peak in the sample. A list of recipes for the solid acids of interest and a deuteration method is outlined in the Appendix.

2.2 X-Ray Powder Diffraction

Powder samples were phase identified via X-ray diffraction (XRD) analysis at room temperature on a Philips diffractometer (X'Pert Pro) using Cu Kα radiation. Intensities were usually obtained in the 2θ range between 10° and 90° with a step size of 0.02° and a measuring time of 10.8 seconds at each step (scan speed 0.05 °/s, utilizing a small area detector). High-temperature scans were achieved using an Anton Paar HTK 1200 oven over a temperature range from room temperature to 300°C. Philips X'Pert Plus software was utilized to perform Reitveld refinements of the unknown phases [1, 2]. Silicon and nickel standards were utilized where appropriate.

2.3 Neutron Powder Diffraction

High-resolution neutron powder diffraction measurements were collected at the Los Alamos Neutron Scattering Center (LANSCE) on the NPDF instrument [3]. Approximately 7 grams of each deuterated solid acid sample were carefully packed in a glove box into cylindrical vanadium cans and sealed with lead wire. Powder diffraction data were collected for 6 hours, at room-temperature and at higher temperatures exhibiting a superprotonic phase. Rietveld refinements were completed with the GSAS Rietveld code [4, 5].

2.4 NMR Spectroscopy

NMR measurements were performed on a Bruker DSX 500 MHz spectrometer and a Bruker DSX 400 instrument (Bruker Analytische Messtechnik GmbH, Germany) at 9.4 T. Magic angle spinning (ω_{MAX}=15 kHz), as well as static probes, were utilized. MestreC software was used to manipulate and analyze NMR spectra [6].

2.5 Impedance Spectroscopy

The conductivity of pressed pellet samples (usual conditions: P = 4 tons, diameter = 10 mm, 5 minutes pressing time) were measured under dry and wet nitrogen in the temperature range of room-temperature to 270°C. Silver electrodes were painted onto the surfaces of pressed sample pellets with silver paint (Ted Pella). A.C. impedance data were collected over the frequency range of 20 Hz – 1 MHz using an HP 4284 precision LCR meter at an applied voltage of 50 mV. Zview (Scribner Associates Inc.), a least-squares refinement program, was utilized to fit the acquired impedance data to several different equivalent circuits including (RQ), (R1Q1)(R2Q2), (R1)(R2Q2), etc., where R is resistance and Q is constant phase element with impedance $Z_Q = (Y(j\omega)^n)^{-1}$; where $j = \sqrt{-1}$, ω = frequency, Y and n are constants, and n ranges between 0 and 1 [7].

2.6 Thermal Analysis

2.6.1 Simultaneous Differential Scanning Calorimetry and Thermogravimetric Analysis

Thermal analysis utilized in characterizing the phase transitions and chemical stability of solid acids was primarily carried out on a Netzsch STA 499 C thermal analyzer equipped with a Pfeiffer Vacuum Thermal Star attachment. This setup was used to simultaneously collect differential scanning calorimetry (DSC), thermogravimetric (TG), as well as mass spectroscopy data. This data allowed for the enthalpy of phase transitions and weight change for the samples to be determined directly, as well as for identification of gasses evolved from the sample.

2.6.2 Drop Solution Calorimetry

To determine the enthalpies of formation, high-temperature drop solution calorimetry in molten sodium molybdate solvent ($3Na_2O{\cdot}4MO_3$) was performed in a custom built Tian-Calvet microcalorimeter operating at 702 ^{o}C [8]. Pressed powder pellets, 15 mg, were dropped from room temperature into molten sodium molybdate solvent. An oxidizing atmosphere was maintained by flushing the solvent chamber with oxygen gas at 100 ml/min. A voltage change in the thermopile was recorded and integrated over time. A calibration factor based on the heat content of 15 mg Al_2O_3 pellets was employed to convert the integrated voltage versus time to enthalpy. The solution calorimetry of sulfates in $2Na_2O.4MoO_3$ solvent at 702 ^{o}C has been carried out previously [8]. All of the samples in this study dissolved in approximately 40 minutes.

2.6.3 Thermomechanical Analysis

A Perkin Elmer TMA 7 Thermomechanical Analyzer was utilized for all thermomechanical tests recording changes in probe position under an applied force at various temperatures. Changes in probe position were used to signify and in some cases distinguish between a solid to solid phase transition and a solid to liquid phase transition.

2.7 Raman Spectroscopy

A Renishaw Ramascope spectrometer was used to collect unpolarized Raman spectra at ambient temperature from randomly oriented specimens. Data was collected at 135° scattering geometry. The spectrometer is equipped with a back-illuminated, liquid-

N_2-cooled CCD detector in the range of 100 to 2000 cm^{-1} providing an intrinsic resolution of 1.5 cm^{-1} with calibrations accurate to ±1 cm^{-1}. The Raman spectra were excited by the 514.5 nm line of an Ar^+ laser focused down to a 5 μm spot on the sample.

2.8 Infrared Spectroscopy

All IR measurements were executed on a Nicolet Magna 860 FTIR spectrometer. Polarized transmission spectra were recorded from 4000 to 400 cm^{-1} by averaging 400 or more scans with 2 cm^{-1} resolution, using a GLOBAR infrared light source, a KBr beamsplitter, a wire-grid on CaF_2 polarizer, and an MCT-A detector.

2.9 Melting Point Apparatus

A Thomas Hoover Uni-Melt Capillary Melting Point Apparatus was used in conjunction with Thomas Scientific melting point standards—anthracene (m.p. 216°C) and hydroquinone (m.p. 172°C)—to visibly identify melting points of solid acid samples. Some solid acid samples suffer from incongruent melting which made access to a melting point apparatus indispensable.

2.10 References:

1. X'Pert Plus. Philips Analytical B.V.: Almelo, 1999.
2. X'Pert HighScore. Philips Analytical B.V.: Almelo, 2002.
3. Proffen, T. 2007 [cited 2007 5/01/07]; Available from: http://lansce.lanl.gov/lujan/instruments/NPDF/index.html.
4. Larson, A.C., and R.B. Von Dreele. "General Structure Analysis System (GSAS)." Los Alamos National Laboratory Report LAUR 86-748 (2000), 2001.

5. Toby, B.H., EXPGUI, a graphical user interface for GSAS. Journal of Applied Crystallography, 2001, 34: 210 – 213.

6. MestReC: NMR Data Processing Made Easy. Mestrelab Research: A Coruna, 2006.

7. Johnson, D. ZView. Scribner Associates, Inc., 2000.

8. Navrotsky, A. Progress and new directions in high temperature calorimetry revisited. Physics and Chemistry of Minerals, 1997, 24(3): 222 – 241.

Chapter 3 $CsHSO_4$

This chapter will present the three best structural models reported in the literature for the superprotonic phase of $CsHSO_4$ (Jirak, Belushkin, and Merinov) [1-3]. Each model's refinement against new high-resolution neutron powder diffraction data will be compared in order to establish which structure best describes the superprotonic phase of $CsDSO_4$. Insights of local structural information from neutron pair distribution function data in the superprotonic phase will also be considered. Entropy calculations based on the three models will be contrasted with experimental data.

3.1 Introduction

Solid acid compounds of $MHXO_4$ stoichiometery, where M = Cs, Rb, NH_4 and X = S, Se, exhibit a superprotonic phase transition in which the proton conductivity jumps by 3 – 4 orders of magnitude. In this first-order phase transition, the compound exists in the energetically favored structure (monoclinic) and switches to an entropically favored structure (tetragonal) at elevated temperatures (T_{sp} = 414 K for $CsHSO_4$). A notable feature of the entropically favored structure is the partial occupancies of the oxygen and deuterium atom positions which allow the compound to sample each configuration. This sampling of configurations, or sulfate/selenate tetrahedral librations (frequency ~ 1×10^{12} Hz), enables protonic conductivity comparable to that of a liquid via the Grotthus mechanism. In the Grotthus mechanism, proton migration proceeds by dipole ($H_nSO_4^{n-2}$) reorientation, structural relaxation and proton hopping. Despite sharp crystalline Bragg diffraction patterns, this work presents pair distribution function analysis of solid acids revealing a slight loss of long-range order in the high-temperature phase, commensurate with other liquid-like properties of superprotonic solid acids, such as high proton conductivity. As Bragg diffraction describes the average structure of a compound, PDF analysis describes structure on a local scale.

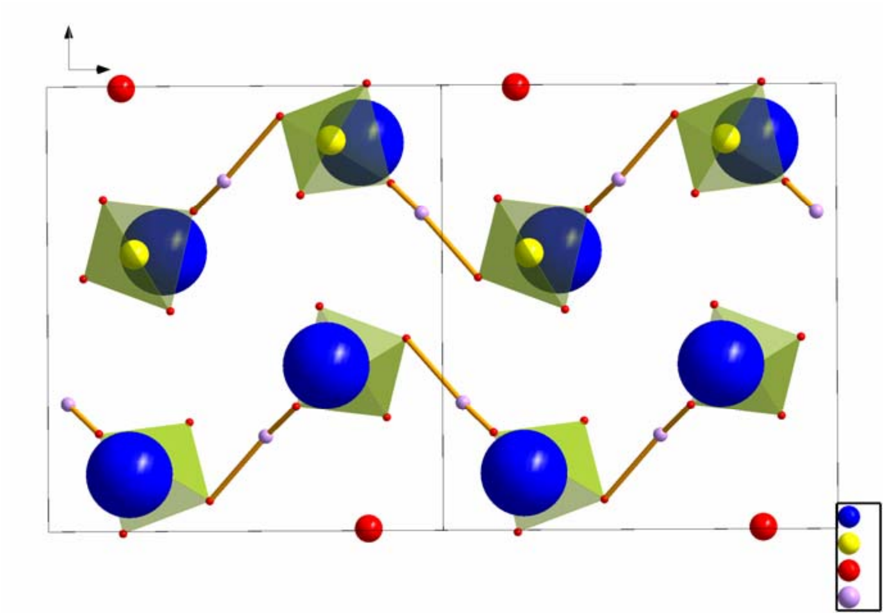

Figure 3-1. $CsDSO_4$ monoclinic refined structure at 333 – 313K. Hydrogen bonds form zigzag chains along the c-axis of the unit cell.

In the monoclinic room temperature phase of $CsHSO_4$, sulfate groups are linked by fully ordered hydrogen bonds forming one-dimensional zigzag chains. For configurational entropy calculations, this low-temperature phase can be considered to have zero configurational entropy. The positions of oxygen atoms are fixed and the hydrogen bonds are asymmetric with a single minimum (Figure 3-1).

An accurate description of the structure of the superprotonic phase is necessary to enumerate the number of configurations that the sulfate or selenate tetrahedra are allowed to sample in order to compare configurational entropy with experimentally measured entropy changes. The goal of this chapter is to determine which structure best describes the superprotonic phase of $CsHSO_4$, based on high-resolution neutron powder diffraction data, and then to compare implied configurational entropies for these models with experimental data. The most important difference between the Jirak, Belushkin, and Merinov models of $CsHSO_4$ are the details of the sulfate group orientations which have direct implications on the configurational entropy.

The high-temperature structures proposed by Jirak, Belushkin, and Merinov each place cesium and sulfur in the 4a or 4b crystallographic sites of the $I4_1/amd$ space group with lattice parameters a ~ 5.7Å, c ~ 14.2 Å [1-3] (Table 3-1). The structures diverge in their assignment of the oxygen and deuterium positions. The Jirak structure utilizes a 50% occupied 32i site for the oxygen atomic coordinate and a 25% occupied 16f site for the deuterium position. This arrangement yields two tetrahedral confirmations, traced in light blue in Figure 3-2 (left).

The Merinov structure assigns one oxygen atom position to a 32i site (0.25 occupancy) and another oxygen position to a 16h site with 0.5 occupancy. The corresponding deuterium sites lie on 16f (0.21 occupancy) and 8e (0.09 occupancy) crystallographic positions. The Belushkin structure also splits the oxygen sites into two 32i sites with 25% occupancy each and the deuterium positions into a 16f (0.246) and 8e (0.094) site. Previous work in determining the configurational entropy of each model considered the 8e position in both the Belushkin and Merinov structures a negligible contribution and ignored it to simplify counting hydrogen bonding configurations. The refinement presented in this work confirms that the 8e site is negligible, as the occupancy in both Belushkin and

Merinov structures is reduced to under 0.03, which results in approximately 1/5 of a total deuterium atom in a unit cell, Z = 4. The original occupancies in the Belushkin and Merinov structures exceed normally expected constraints of four hydrogen atoms per unit cell.

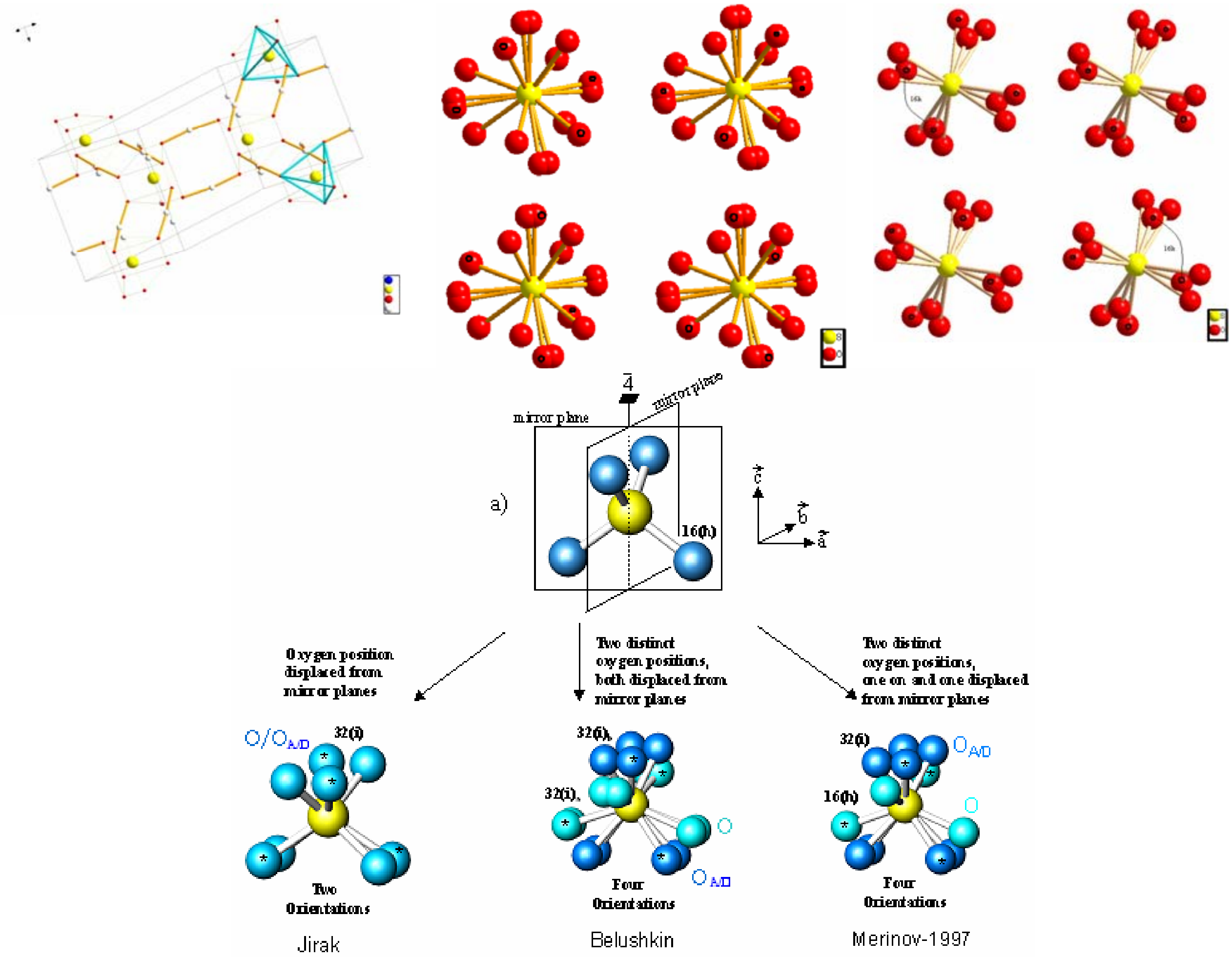

Figure 3-2. Jirak (top left), Belushkin (top center), and Merinov (top right) sulfate tetrahedral orientations. The Jirak diagram is a fragment of a unit cell with the Cs atoms and deuterium atoms that are not hydrogen bonded deleted for clarity. The diagram shows the two tetrahedral orientations possible in the Jirak structure. Merinov and Belushkin structures each have four tetrahedral orientations, oxygen atoms participating in a tetrahedron are marked by "o." The Merinov structure has oxygen positions in the 16h site with 0.5 occupancy and the other oxygen site, 32i, has 0.25 occupancy (illustrated in the diagram). (bottom) Sulfate tetrahedral arrangements proposed by each structure.

Jirak Structure

Atom	Site	x	y	z	Site Occ.
Cs	4b	0.5	0.25	0.125	1
S	4a	0	0.75	0.125	1
O	32i	0.201(3)	0.678(8)	0.067(1)	4
D	16f	0.19(1)	0.5	0	1

Belushkin Structure

Atom	Site	x	y	z	Site Occ.
Cs	4b	0.5	0.25	0.125	1
S	4a	0	0.75	0.125	1
O	32i	0.0559(9)	0.5860(6)	0.2038(2)	2
O	32i	0.0273(15)	0.4928(6)	0.1607(3)	2
D	16f	0.25	0.5860(6)	0.25	0.98(28)
D	8e	0	0.25	0.1607(3)	0.188(14)

Merinov Structure

Atom	Site	x	y	z	Site Occ.
Cs	4a	0	0.75	0.125	1
S	4b	0.5	0.25	0.125	1
O	32i	0.6655(70)	0.3097(70)	0.0475(25)	2.00(8)
O	16h	0.7403(59)	0.25	0.0870(26)	2.04(12)
D	16f	0.666	0.5	0	0.84
D	8e	0	0.25	0.087	0.18

Table 3-1. Original Structures Proposed for $CsHSO_4$

3.2 Synthesis and Characterization Methods

$CsHSO_4$ powder samples were precipitated out of a solution containing stoichiometric amounts of Cs_2SO_4 and H_2SO_4 with acetone. The resulting powder was vacuum filtered and dried in an oven at 90°C. X-ray diffraction patterns were collected to verify phase purity after original synthesis and deuteration (Phillips X'Pert Pro, Cu Kα radiation, 0.02° steps, 11 s/step).

As hydrogen crystallographic positions are not reliably probed by X-rays, neutron diffraction data was sought to determine the location of the hydrogen atoms in the unit cell. $CsHSO_4$ is known to be isomorphic to its deuterated analog, $CsDSO_4$. Sample deuteration was achieved (> 99% deuteration) by the following method:

1. Dissolve phase pure solid acid sample, $CsHSO_4$, in D_2O.
2. Freeze dry resulting solution in a flask isolated from ambient air with a glass valve between flask and freeze dryer.
3. Inject D_2O with a syringe through a rubber diaphragm to cover inlet orifice and isolate sample from ambient air. Make sure all solid acid is dissolved and then freeze dry.
4. Repeat step 3 at least five times to ensure high deuteration level. Check deuteration level with ^{1}H and ^{2}H NMR, as in Figure 3-3. For neutron diffraction data and especially for pair distribution function data, deuteration levels should be > 99%. (Note: ^{1}H NMR is an especially sensitive indicator of the presence of crystallographic hydrogen.)

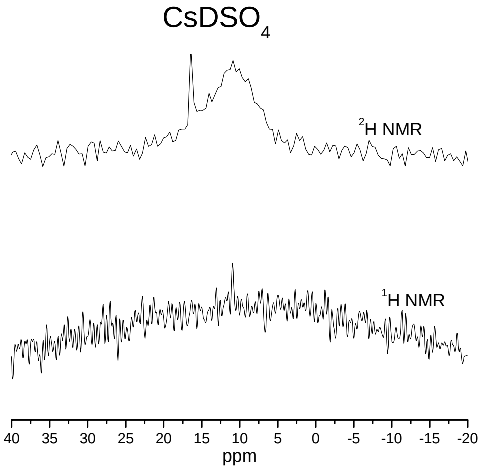

Figure 3-3. Verification of deuteration level on $CsDSO_4$ prior to neutron diffraction experiments. The small ^{1}H signal at 11 ppm indicates presence of hydrogen in the structure and incomplete deuteration. Prior to neutron diffraction analysis, this sample was redeuterated.

3.3 Low- and High-Temperature Structure & Refinement Results

High-resolution neutron powder diffraction measurements were collected at the Los Alamos Neutron Scattering Center (LANSCE) on the NPDF instrument. Approximately 7 grams of $CsDSO_4$ powder solid acid sample were carefully packed in a glove box (Ar atmosphere) into a 3/8" diameter cylindrical vanadium can and sealed with lead wire. Powder diffraction data were collected for 6 hours for the low-temperature phase (T = 333 – 313K), and 6 hours in the superprotonic phase (T = 428K). Rietveld refinements were completed with the GSAS Rietveld code [4, 5].

3.3.1 Refinement at 333 – 313K

Neutron diffraction data collected in the temperature range, T = 333 – 313 K, were used to refined the Chisholm (2000) structure, $P2_1/c$ for completeness [6] (Tables 3-2 & 3-3, Figure 3-4). Overall, 147 variables were refined and the background was fit graphically using a shifted Chebyschev with 36 terms for each histogram. Refined parameters include cell parameters, U_{ani}, atom coordinates for all atoms, absorption/extinction, scaling, profile parameters, March-Dollase preferential orientation ratios and fractions for the {100} directions. In estimating standard uncertainties, U_{ani} and atomic coordinates were refined concurrently. The final refinement converged to $\chi^2 = 4.407$ for 67 variables.

	333-313K	428K
Space group:	$P2_1/c$	$I4_1/amd$
a (Å)	7.79579(11)	5.74146(26)
b (Å)	8.14963(11)	5.74146(26)
c (Å)	7.73332(11)	14.3007(14)
β	110.9423(10)	90

Z	4	4
V (Å)	458.864(7)	471.41(5)
R_p x 100	2.18	3.15 Jirak 2.98 Belushkin 2.90 Merinov
R_{wp} x 100	3.01	5.14 Jirak 5.00 Belushkin 4.97 Merinov
χ^2	4.407	5.68 Jirak 5.377 Belushkin 5.292 Merinov

Table 3-2. Crystal Data and Structure Refinement Parameters for $CsDSO_4$ at 333 – 313K and 428K

Atom	x	y	z	U_{11}	U_{22}	U_{33}	U_{12}	U_{13}	U_{23}
Cs	0.21541(29)	0.12817(30)	0.20548(29)	0.0209(13)	0.0282(11)	0.0285(13)	0.0012(11)	0.0088(10)	0.0031(11)
S	0.7514(5)	0.1225(4)	0.2800(5)	0.0194(20)	0.0083(17)	0.0236(21)	-0.0297(17)	-0.0080(16)	-0.0041(18)
O1	0.5886(4)	0.2200(4)	0.1286(4)	0.0319(16)	0.0691(22)	0.0414(15)	0.0123(15)	0.0064(13)	0.0215(15)
O2	0.66637(33)	0.06827(31)	0.40876(32)	0.0491(16)	0.0431(15)	0.0289(14)	0.0009(10)	0.0261(12)	0.0097(11)
O3	0.89586(30)	0.25486(29)	0.85815(30)	0.0362(13)	0.0308(14)	0.0499(17)	0.0209(12)	0.0124(13)	0.0113(12)
O4	0.8079(4)	0.99527(28)	0.1888(4)	0.0762(21)	0.0287(14)	0.0525(17)	0.0042(13)	0.0413(15)	-0.0101(12)
D1	0.6330(4)	0.28695(30)	0.0512(4)	0.0639(18)	0.0472(16)	0.0452(18)	-0.0036(13)	0.0291(14)	0.0054(13)

Table 3-3. Atomic Coordinates and Thermal Displacement Parameters of $CsDSO_4$ at 333 – 313K

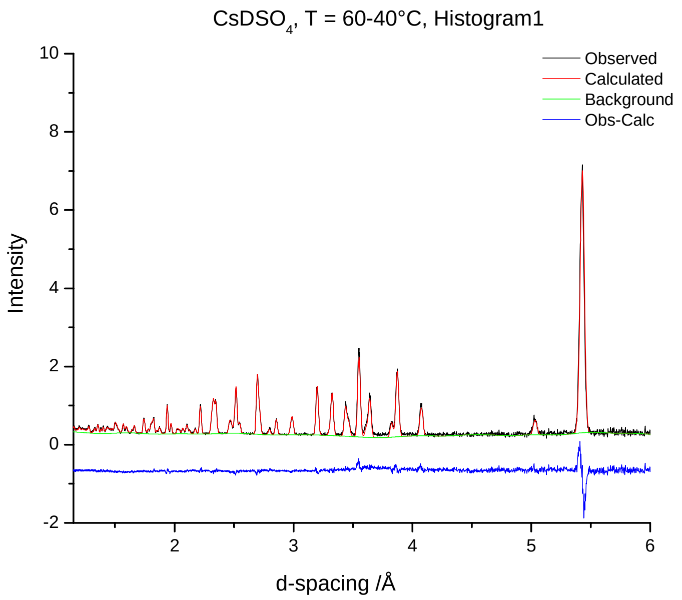

Figure 3-4. Neutron diffraction refinement results for $CsDSO_4$, T = 333 – 313K (60 – 40°C), bank 1

The monoclinic phase refinement results agree well with published data. Thermal parameters from the room-temperature refinement will be compared to that of the tetragonal high-temperature phase refinement for reference. Refinement results for the monoclinic phase are included in Tables 3-2 and 3-3, and Figure 3-3.

Neutron pair distribution function (PDF) data for $CsDSO_4$ in the monoclinic phase indicate excellent agreement between the average structure and local structure as well as long-range atom pair correlations (Figure 3-5 (left)). D – O bond distances determined by atom pair correlations from peak positions in the PDF match that of the average structure determined by Rietveld refinements (Figure 3-5 (right)). As the deuterium atom is not expected to be very mobile in this phase, it makes sense that the D – O bond distance is preserved between average and local structural descriptions.

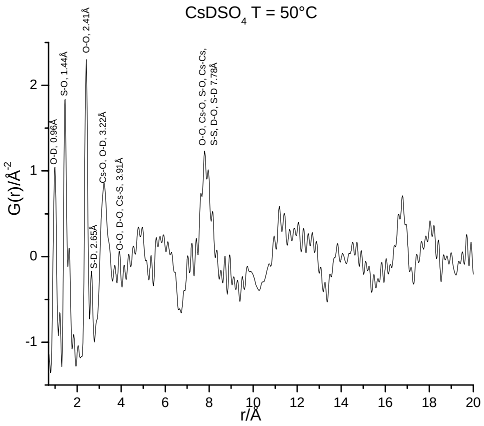

Bond	PDF Bond Length, Å	Bragg Diffraction Structural Refinement Bond Length, Å
D – O	0.96	0.96
S – O	1.44	1.41,1.44, 1.47, 1.59
O – D	1.65	1.697
O – O	2.41	2.38, 2.44
S – D	2.65	2.68
Cs – O	3.22	3.12, 3.69, 3.88
O – D	3.22	3.36

Figure 3-5. (left) Pair distribution function plot of $CsDSO_4$, T = 333 – 313K (60 – 40°C) illustrates long-range order. Structural features identified include the bond distances associated with the sulfate tetrahedra as well as features at a distance of 18 Å. (right) Atom pair distances inferred from the PDF plot are compared to analogous distances calculated from the crystal structure. Average versus local atom distances agree to the picometer in length for small atom pair distances.

3.3.2 Refinement at 428 K, (155°C)

Neutron diffraction data collected at T = 428 K were used to refine the Jirak, Merinov, and Belushkin $CsHSO_4$ structures in the $I4_1/amd$ space group. The least-squares refinement began by preparing a generic refinement without oxygen or deuterium positions. The generic least-squares refinement included lattice parameters, U_{ani}, atom coordinates for cesium and sulfur atoms, absorption/extinction, scaling, and profile parameters. The background was graphically fitted to a 36-term shifted Chebyschev polynomial for each histogram. In the initial stages, each of the atomic coordinates, thermal, and lattice parameters were refined independently and successively updated in subsequent cycles. The final generic refinements each converged to $\chi^2 = 14.32$ for 6 variables.

Once the generic refinement was prepared, each structure was subjected to a refinement using the profile parameters and fitted background from the generic refinement. The least-squares refinement on each structure included only the anisotropic thermal parameters for all atoms and atomic coordinates. In the case of the Belushkin and Merinov structures, the fractional occupancy of the split deuterium positions was also refined with the constraint that the structure contain the stoichiometric number of deuteriums (Z=4, $CsDSO_4$, 4 total deuteriums per unit cell). The Merinov structure final refinement converged to $\chi^2 = 5.292$ for 10 variables (91 variables refined overall). The Belushkin structure final refinement converged to $\chi^2 = 5.377$ for 23 variables (94 variables overall), while the final Jirak refinement converged to $\chi^2 = 5.68$ for 18 variables (80 overall) (Table 3-2, Figure 3-6). Thermal parameters and atom coordinates were refined separately in the final refinement to allow for standard uncertainties to be determined for each set of parameters while preserving the stability of the refinement (Table 3-4).

The difference in χ^2 between the three structures is not significant enough to decide which structure is the best description of $CsHSO_4$. The Belushkin and Merinov structures incorporate a split oxygen and deuterium site model which adds more parameters for refinement so the χ^2 value is not necessarily a valid comparison of the three structures. As χ^2 is not significantly better, including the split atom positions, the Jirak structure may describe the high-temperature structure more accurately than the Belushkin and Merinov structures.

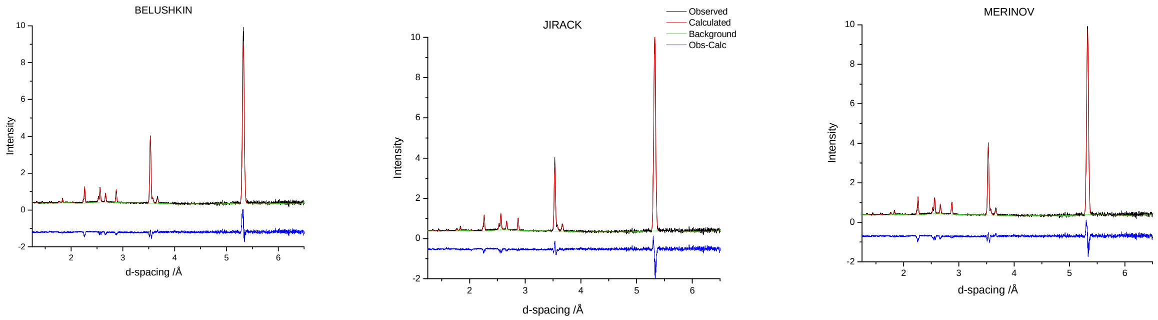

Figure 3-6. Neutron diffraction refinements of $CsDSO_4$, T = 428K (155°C), bank 1 into Belushkin (left), Jirak (center), and Merinov (right) structures. Experimental results are indicated in black, refined pattern in red, background in green, and difference curve in blue. Comparing the three structures via the difference curve is inconclusive.

The three refinements yield differences curves which are not identical but are not different enough to support one structure over the other as a superior fit for the high temperature phase of $CsDSO_4$ (Figure 3-6). Employing a Hamilton test on the significance of the R factor for the three refinements can help determine if the oxygen and deuterium positions are constrained to a single site, according to these refinements[7].

The Hamilton's test indicates whether the addition of parameters to a least-squares refinement results in a significant improvement or significant worsening of the agreement between observed and calculated structure factors. In this test, a ratio of generalized R factors is compared to tabulated values to determine the significance level at which a model can be rejected or accepted. As the ratio of R factors is relatively insensitive to how the R factors are computed, we employ a ratio of the weighted R factors, $\Re = \frac{R_{1_{wp}}}{R_{0_{wp}}}$, where

$R_{wp} = \left[\frac{\sum_i w_i \left(|F_i|_o - |F_i|_c \right)^2}{\sum_i w_i |F_i|_o^{\,2}} \right]$, $R_{1_{wp}}$ is the weighted R factor for a structure resulting from a refinement with restraints on some of the parameters and $R_{0_{wp}}$ is that of an unrestricted least-squares refinement.

As the Merinov and Belushkin structures split the oxygen and deuterium sites, either of these models can be used as the unconstrained model. The Jirak model constrains the oxygen and deuterium sites to a single site each.

(Jirak) O and D atoms have a single crystallographic site each: O—32i, D—16f.

(Merinov) The O atoms are split into two sites: 32i and 16h, and the D site is split between a 16f site and a 8e site.

(Belushkin) The O atoms are split into two 32i sites and the D atoms are split into 16f and 8e sites.

The number of parameters refined in these three cases were $m_{\mathrm{Jirak}} = 80$, $m_{\mathrm{Merinov}} = 91$, and $m_{\mathrm{Belushkin}} = 94$. There were 257 reflections. The weighted R factors achieved were $R_{\mathrm{Jirak}} = 0.0514$, $R_{\mathrm{Merinov}} = 0.0497$, and $R_{\mathrm{Belushkin}} = 0.05$.

Let us test the hypothesis:

H_0: O and D each reside on a single crystallographic site.

To test this hypothesis, the weighted R factor for the restrained model (Jirak) corresponds to the hypothesis and the unrestrained model (Belushkin or Merinov). The appropriate R-factor ratio is

$$\Re = \frac{R_{Jirack}}{R_{Merinov}} = \frac{0.0514}{0.0497} = 1.034$$

$$\Re = \frac{R_{Jirack}}{R_{Belushkin}} = \frac{0.0514}{0.05} = 1.028.$$

The dimension of the hypothesis is in the first case, $\mathrm{m}_{\mathrm{Merinov}} - \mathrm{m}_{\mathrm{Jirack}} = 11$ and in the second case, $\mathrm{m}_{\mathrm{Belushkin}} - \mathrm{m}_{\mathrm{Jirack}} = 14$, and the number of degrees of freedom for the refinement is $\mathrm{n} - \mathrm{m} \approx 163$. Values of $\Re$ interpolated from the Hamilton tables—

$$\Re_{11,163,0.005} = 1.084$$

$$\Re_{11,163,0.1} = 1.053$$

$$\Re_{11,163,0.25} = 1.042$$

$$\Re_{11,163,0.5} = 1.031$$

—suggest that the error in rejecting the hypothesis of oxygen and deuterium atoms each occupying a single crystallographic site is on the order of 50%.

The Hamilton test applied to evaluate the significance of added O and D sites suggests that a single O and D site hypothesis cannot be rejected at the 50% significance level. The results of this neutron diffraction experiment do not reject the Jirak model.

The refinements of the 8e deuterium position in the Belushkin and Merinov structures resulted in a decrease of the original occupancy ~ 0.09 → 0.028 or 0.027 occupancy (Tables 3-1 & 3-5). This confirms that this site's contribution is negligible to the configurational entropy according to this set of neutron diffraction data.

The thermal parameters of the three refined structures vary widely for the oxygen and deuterium sites. In the Jirak model, U_{iso} for the oxygen and deuterium sites is 0.303 Å^2 and

0.176 Å^2 respectively, which implies a thermal motion displacement of approximately ½ Å. The Merinov thermal parameters for oxygen and deuterium sites are 0.412 Å^2 (32i) and 0.3751 Å^2 (16h), and 0.529 Å^2 for the deuterium 16f site. The thermal parameter for the 8e deuterium site is 0.019 Å^2, which is too low for a deuterium atom at elevated temperatures, which is expected to be very mobile. (The room temperature structure's deuterium thermal parameter refined to 0.0495 Å^2, for reference.) The Belushkin parameters for oxygen and deuterium are also high: 0.505 Å^2 and 0.36718 Å^2 (32i—O), 0.602 Å^2 (16f—D), and 0.386 Å^2 (8e—D). Independently, these thermal parameters could not disqualify a structure; however, the high Belushkin and Merinov thermal parameters could be compensating for a poor atomic coordinate assignment.

Of the three models, shown in Figure 3-7, the Jirak structure is deemed the best suited to describe the average structure of superprotonic conductor, $CsDSO_4$. Despite the Jirak model's usual R_p, R_{wp}, and χ^2 statistics, the Hamilton test, along with an analysis of the refined thermal parameters supports the Jirak model as the best crystallographic description of $CsDSO_4$.

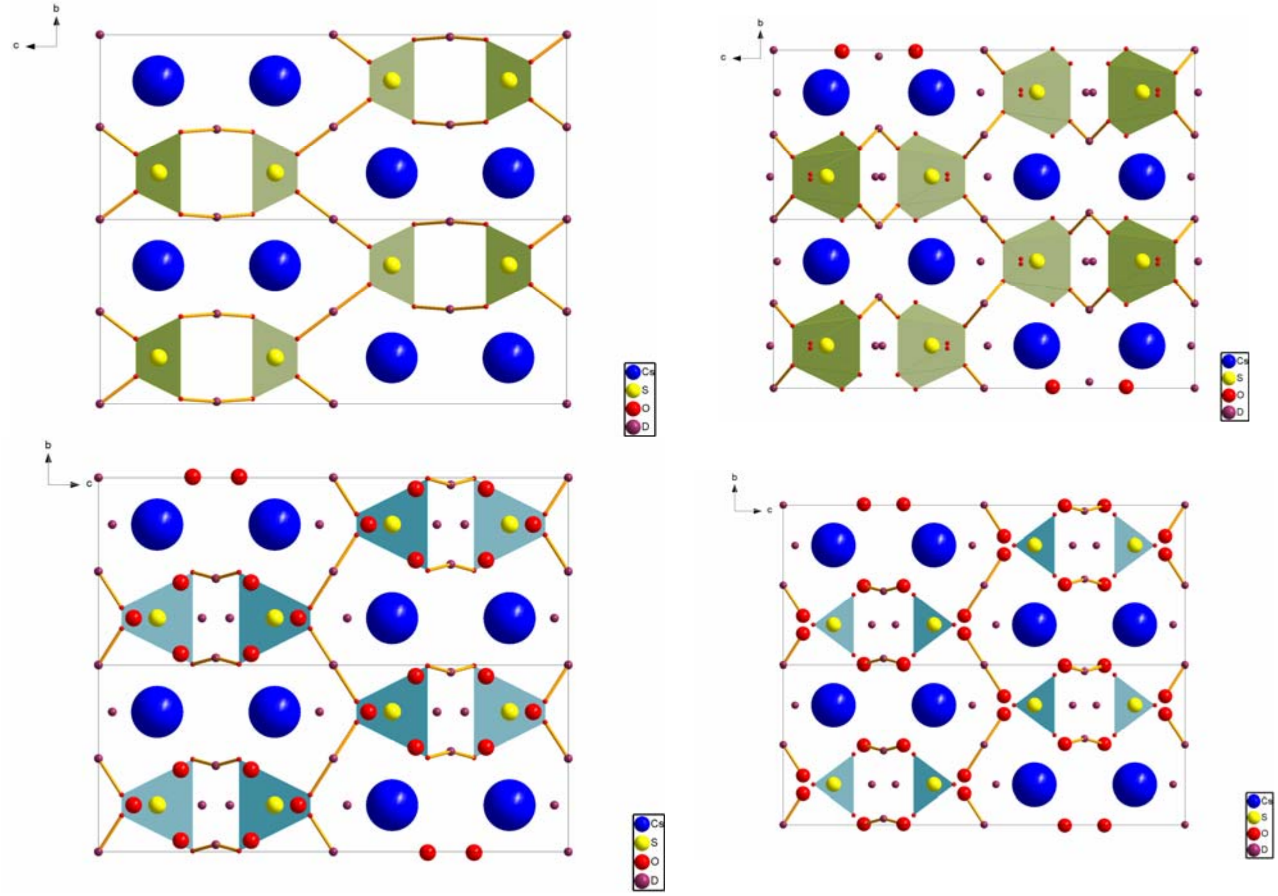

Figure 3-7. CsDSO$_4$ structures: Jirak (top left), Belushkin (top right), Merinov (bottom left, large tetrahedra, bottom right, smaller tetrahedra). Tetrahedra in the Merinov structure represent 12 oxygen sites which comprise 4 tetrahedral orientations. The sites included in the smaller tetrahedra on the right have occupancy of ½ while the sites indicated in the larger tetrahedra on the left have ¼ occupancy. The actual tetrahedral configurations sample two of the ½ occupancy sites for two sets of ¼ occupancy oxygen sites.

Jirak Structure

Atom	Site	x	y	z	Site Occ.	U_{11}	U_{22}	U_{33}	U_{12}	U_{13}	U_{23}
Cs	4b	0.5	0.25	0.125	1	0.342(4)	0.342(4)	0.279(6)	0	0	0
S	4a	0	0.75	0.125	1	0.0664(19)	0.0664(19)	0.723(19)	0	0	0
O	32i	0.2231(5)	0.6474(8)	0.07689(21)	4	0.2157(21)	0.368(11)	0.326(4)	0.0278(31)	0.1945(24)	-0.0204(35)
D	16f	0.2378(11)	0.5	0	1	0.291(7)	0.193(6)	0.0458(29)	0	0	0.0018(35)

Belushkin Structure

Atom	Site	x	y	z	Site Occ.	U_{11}	U_{22}	U_{33}	U_{12}	U_{13}	U_{23}
Cs	4b	0.5	0.25	0.125	1	0.1519(18)	0.1519(18)	0.366(7)	0	0	0
S	4a	0	0.75	0.125	1	0.230(5)	0.230(5)	0.0540(33)	0	0	0
O	32i	0.1174(14)	0.5773(6)	0.2042(4)	2	0.800(30)	0.202(6)	0.513(11)	-0.312(11)	-0.363(15)	0.311(6)
O	32i	0.0099(13)	0.4938(11)	0.1646(4)	2	0.227(6)	0.486(11)	0.388(13)	-0.219(8)	-0.214(11)	0.295(9)
D	16f	0.25	0.4644(23)	0.25	0.9456	0.800(29)	0.702(31)	0.305(18)	0	0.400(23)	0
D	8e	0	0.25	-0.245(6)	0.0542	0.80(27)	-0.090(17)	0.45(23)	0	0	0

Merinov Structure

Atom	Site	x	y	z	Site Occ.	U_{11}	U_{22}	U_{33}	U_{12}	U_{13}	U_{23}
Cs	4a	0	0.75	0.125	1	0.14931	0.14931	0.32676	0	0	0
S	4b	0.5	0.25	0.125	1	0.17506	0.17506	0.08063	0	0	0
O	32i	0.7447(11)	0.3059(6)	0.0496(4)	2	0.800(14)	0.093(4)	0.345(5)	-0.028(4)	0.400(8)	-0.0754(30)
O	16h	0.6905(6)	0.25	0.07510(30)	2	0.1540(31)	0.737(11)	0.234(6)	0	0.171(4)	0
D	16f	0.7150(18)	0.5	0	0.9429	0.8	0.26537	0.52133	0	0	0.28615
D	8e	0	0.25	0.2208(10)	0.0571	0.04811	0.09743	-0.09	0	0	0

Table 3-4. Refined Atomic Coordinates and Thermal Displacement Parameters of CsDSO4 at 428K in the Jirak, Belushkin, and Merinov structures

	Jirak		**Belushkin**				**Merinov**			
Number of Orientations	**2**		**4**				**4**			
Oxygen site	**32i**		**32i**		**32i**		**32i**		**16h**	
Occupancy	**0.5**		**0.25**		**0.25**		**0.25**		**0.5**	
Proton site	**16f**		**16f**		**8e**		**16f**		**8e**	
Occupancy	**0.25**		**0.2364**		**0.0271**		**0.23573**		**0.02855**	
d(S – O) (Å)	**1.57**		**1.576**		**1.652**		**1.30**		**1.79**	
$\angle$ O – S – O (°)	**101.0**	**127.9**	**96.7**	**102.5**	**107.4**	**126.0**	**100.4**	**106.1**	**113.5**	**118.5**

Table 3-5. Jirak, Belushkin, and Merinov Models Contrasted in Terms of Tetrahedral Orientations, Oxygen, and Deuterium Site Occupancy and Tetrahedral Geometery

3.4 Pair Distribution Function Analysis

An important distinction of pair distribution function (PDF) analysis is that the data depicts local structure information as Bragg diffraction describes average structure information. The D-O atom pair distance in the PDF is a very normal bond length of 0.97 Å, while the same bond lengths, according to refined structures of the average positions, claim at least 1.20 Å by the most conservative estimate in the three structures (Figure 3-8). This discrepancy can only attest to the deuterium’s motion in the superprotonic phase but not help confirm the validity of any of the crystallographic models.

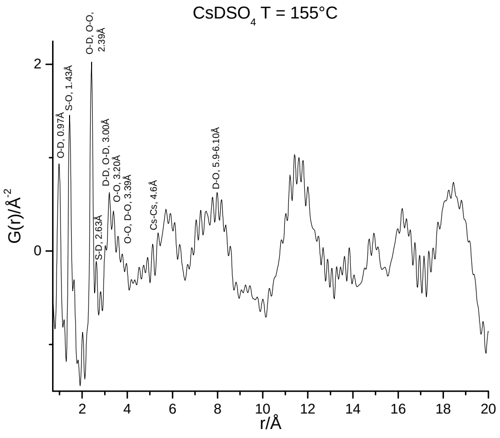

Bond	PDF Bond Length, Å	Bragg Diffraction Structural Refinement Bond Length, Å
D – O	0.97	1.39 Jirak 1.20 Belushkin 1.33 Merinov
S – O	1.43	1.57 Jirak 1.58 Belushkin 1.30, 1.80 Merinov
O – D	2.39	2.31 Jirak 2.01 Belushkin 1.78 Merinov
O – O	2.39	2.42 Jirak 2.14, 2.40, Belushkin 2.40 Merinov
S – D	2.63	2.67 Jirak 2.83 Belushkin 2.21 Merinov

Figure 3-8. PDF plot of CsDSO$_4$ in the superprotonic phase, T = 428K (155°C). Peak positions from the PDF are compared to crystallographic atom distances in each of the three proposed structures. As the PDF captures the local, and Bragg diffraction conveys the average structural information, D-O bond distances are lengthened in the average picture as the deuterium is in motion.

Other atom pair distances in the pair distribution function also cannot support one structure's accuracy because differences between local structure and average structure are greater than the differences between the three structures under consideration. A striking interpretation of the PDF data from CsDSO$_4$ is that, in comparison to the PDF taken in the lower-temperature phase (Figure 3-4), peaks at longer pair distances than around 3 Å are smoothed out more than the thermal parameters refined would suggest. The thermal parameter for cesium in the Jirak structure, for example, is U_{iso} = 0.321 barn, which translates to an average displacement of 0.57 Å. The peaks present in the PDF at distances greater than 3 Å, i.e., outside the sulfate tetrahedron, are smoothed on the order of 2 Å. While it is possible that several atom pair distances each add an additional average thermal displacement to contribute to the overall broadness of these features, a local picture of a crystalline material is expected to have less variability in atom distances.

3.5 Entropy Evaluations

As there is a range in literature values (11.0 – 14.3 J mol^{-1} K^{-1}) for the entropy of the superprotonic phase transition of $CsHSO_4$[8], differential scanning calorimetry measurements were performed on $CsHSO_4$ at a rate of ¼ K/min, after a complete set of sensitivity and temperature calibrations were collected. Experimental data collected at this slow heating rate falls within the range of literature values, ΔS = 13.7 J mol^{-1} K^{-1}, for the entropy of the superprotonic phase transition of $CsHSO_4$ with an onset temperature of 141.7°C.

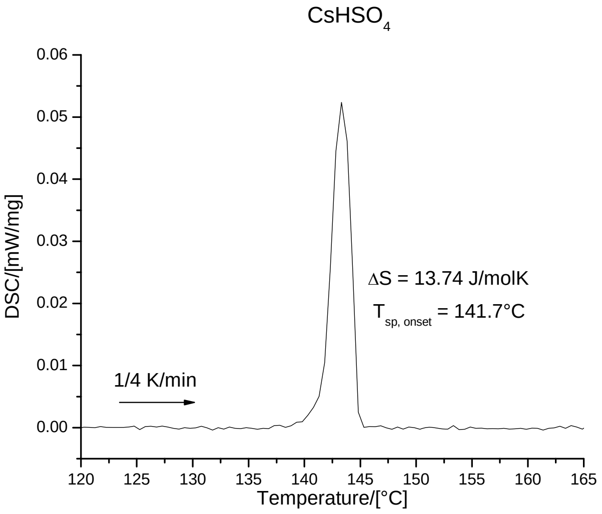

Figure 3-9. CsHSO4 differential scanning calorimetry curve collected at a scan rate of ¼ K/min under flowing N_2

The entropy calculations for each of the three models are based on Pauling's Ice Rules and have been presented in the literature [8]. Chisholm, et al., assumes that the entropy is entirely configurational, arising from sulfate group orientational disorder and disorder in the hydrogen-bond network. Their adaptation of Pauling's Ice Rules provides that there is only one proton per sulfate tetrahedron and only one proton per hydrogen bond, and defects are considered negligible.

Following the formalism set forth in the literature, the configurational entropy

$$S_{config} = R\ln(\Omega)$$

where R is the gas constant (8.314 J/molK) and Ω is the total number of configurations including tetrahedral orientations and hydrogen bonds [8]. Chisholm et al. outlined the number of configurations:

$$\Omega = \begin{pmatrix} \# of \\ proton \\ configurations \end{pmatrix} \times \begin{pmatrix} probability \\ proton \\ site\, is\, open \end{pmatrix}^{(\# of\ protons)} \times \left(\# of\ oxygen\, positions\right).$$

For the Jirak model:

$$\Omega = \begin{pmatrix} 4 \\ 1 \end{pmatrix} \times \left(\frac{3}{4}\right)^{(1)} \times \left(2\right) = 6,\ \ S_{config} = 14.89\frac{J}{mol\, K}.$$

For either the Belushkin or Merinov models, the hydrogen bonding is determined by the tetrahedral orientation and the only contribution to Ω comes from the number of tetrahedral orientations, Ω = 4, and

$$S_{config} = R\ln(4) = 11.52\frac{J}{mol\, K}.$$

Since the room temperature structure of $CsHSO_4$ (and $CsDSO_4$) can be regarded as fully ordered with zero configurational entropy, the entropy of the superprotonic transition is the configurational entropy of the high-temperature phase.

The neutron diffraction refinement results favoring the Jirak structure and measured entropy values are in excellent agreement. The configurational entropy of the Jirack structure, 14.89 J/mol K, is within the range presented the literature and the measurement of 13.7 J/mol K from this work.

3.6 Conclusions

New high-resolution neutron powder diffraction data supports the Jirak model for the high temperature phase of superprotonic conductor $CsDSO_4$. A Hamilton's test for the significance of added refinement parameters cannot support rejecting the hypothesis that there is a single oxygen and deuterium site, as proposed in the Jirak structure.

Aside from refinement statistics, the actual refined parameters of the Jirak structure make the most intuitive sense in terms of thermal parameters. The occupancies of the 8e deuterium site in the Merinov and Belushkin models are reduced from the original occupancy of 0.09 to less than 0.03, resulting in less than 1/5 of a deuterium per unit cell, Z =4. Thermal parameters in the Merinov and Belushkin models for deuterium and oxygen atomic sites are much larger than in the Jirak model.

Pair distribution function analysis illustrates that there is a difference between average and local structure in the superprotonic phase which is a testament to the high mobility of the deuterium atom in the superprotonic phase. Local structure does not seem to conform with great fidelity to the average structure refined by Bragg diffraction.

3.7 References

1. Jirak, Z., et al. A Neutron-Diffraction Study of the Superionic Phase in $CsHSO_4$. Physica Status Solidi a-Applied Research, 1987, **100**(2): K117 – K122.

2. Merinov, B.V. Localization of Hydrogen Atoms in Protonic Conductors with a Dynamical Disordered Network of Hydrogen Bonds: Effect of Anomalous Manifestation of Hydrogen Atoms on Electron-Density Maps. Kristallografiya, 1997, **42**: 906 – 917.

3. Zetterstrom, P. et al. Structure and Proton Conduction in $CsDSO_4$. Solid State Ionics, 1999, **116**(3-4): 321 – 329.

4. Larson, A.C. and R.B. Von Dreele. "General Structure Analysis System (GSAS)", Los Alamos National Laboratory Report LAUR 86-748 (2000), 2001.

5. Toby, B.H. EXPGUI, a Graphical User Interface for GSAS. Journal of Applied Crystallography, 2001, **34**: 210 – 213.

6. Chisholm, C.R.I. and S.M. Haile. X-Ray Structure Refinement of $CsHSO_4$ in Phase II. Materials Research Bulletin, 2000, **35**(7): 999 – 1005.

7. Hamilton, W.C. Significance Tests on Crystallographic R-Factor. Acta Crystallographica, 1965, **18**: 502.

8. Chisholm, C.R.I. and S.M. Haile. Entropy Evaluation of the Superprotonic Phase of $CsHSO_4$: Pauling's Ice Rules Adjusted for Systems Containing Disordered Hydrogen-Bonded Tetrahedra. Chemistry of Materials, 2007, **19**(2): 270 – 279.

Chapter 4 $RbHSeO_4$

The superprotonic structure of $RbDSeO_4$ refined from high-resolution neutron powder diffraction data will be presented. $RbDSeO_4$ and $RbHSeO_4$ are isomorphous at room-temperature; however, an isotope effect alters the superprotonic transition temperature. Previously, attempts at determining the superprotonic structure using X-ray diffraction suffered from a lack of resolution between rubidium and selenium atoms, resulting in a more symmetric structure, as well as an inability to locate hydrogen positions [11]. In this work, $RbDSeO_4$ has been identified to be in the tetragonal $I4_1/amd$ space group and the discussion in Chapter 3 regarding $CsHSO_4$ sulfate tetrahedral orientation will be revisited for this compound. Local structural information available from neutron pair distribution function data in the superprotonic phase suggests slightly diminished long-range order when compared to the lower-symmetry, room-temperature phase. Entropy calculations will be contrasted with experimental data.

4.1 Introduction

Rubidium hydrogen selenate is a superprotonic compound with a unique set of phase transitions. According to Makarova, $RbHSeO_4$ transforms from a triclinic B1 structure (Phase III) to a monoclinic structure B112 (Phase II) at 370K [4], followed by a complicated set of superprotonic phase transitions into the $I4_1/amd$ space group (Phase I) beginning at 448K (in deuterated analog, 427K), and subsequent dehydration. Brach, Jones, and Roziere have shown that the hydrogen atoms in phase II are disordered [1]. Previously proposed structures for the high-temperature phase of $RbHSeO_4$ include I4/mmm, which suffered from the inability of X-ray diffraction to clearly distinguish rubidium (A = 37) from selenium (A =

34) [11]. Along with the ability of identifying crystallographic deuterium sites, neutron diffraction can distinguish between selenium and rubidium as the coherent cross section of rubidium is 6.32 barn and that of selenium is 7.98 barn.

Unfortunately, the phase transition is complex, and so calorimetric measurements of the transition enthalpy have been confused, as only slow scanning rates (¼ K/min) can distinguish the two (or possibly three) phase transitions. Previous work reports 25.3 J/mol K as the enthalpy of the phase transition which is the result of scanning at 1 K/min and being unable to distinguish the superprotonic phase transition from the decomposition transition. The deuterated analog exhibits an isotopic effect of lowering the transition temperature from 448K → 427K which is the first example of this effect in solid acid compounds for the superprotonic phase transition temperature. Solid acid compounds, such as CsH_2PO_4, have large isotopic effects on deuteration for the ferroelectric to paraelectric phase transition which occurs at temperatures lower than room-temperature.

4.2 Synthesis and Characterization Methods

$RbHSeO_4$ powder samples were precipitated out of a solution containing Rb_2CO_3 and excess H_2SeO_4 by heating the solution at 80°C for several hours and then cooling the concentrated mixture to 0°C over an ice block. After vacuum filtering for hours to remove excess selenic acid, powder crystals were rinsed with methanol. If sufficient time is not allowed during filtering, rinsing with methanol will produce a pink tint on the crystals. Do not use acetone to rinse a selenate compound. X-ray diffraction patterns were collected to verify phase purity after original synthesis and deuteration (Phillips X'Pert Pro, Cu Kα radiation, 0.02° steps, 11s/step).

Sample deuteration was achieved (> 99% deuteration) by the following method:

1. Dissolve phase pure solid acid sample, $RbHSeO_4$, in D_2O.
2. Freeze dry resulting solution in a flask isolated from ambient air with a glass valve between flask and freeze dryer.
3. Inject D_2O with a syringe through a rubber diaphragm to cover inlet orifice and isolate sample from ambient air. Make sure all solid acid is redissolved and then freeze dry.
4. Repeat step 3 at least five times to ensure high deuteration level. Check deuteration level with ^1H and ^2H NMR (Figure 4-1).

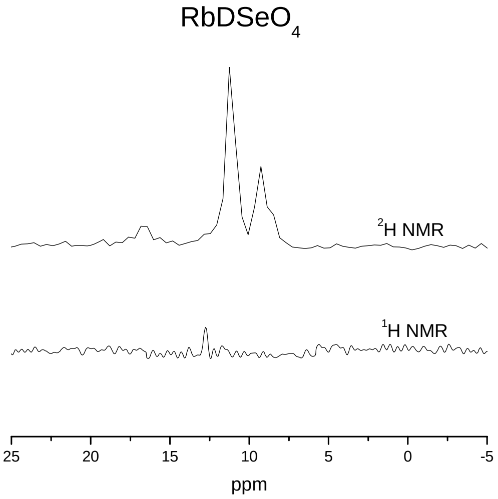

Figure 4-1. Deuteration level verification on $RbDSeO_4$ prior to neutron diffraction experiments. Peak at 13 ppm in the ^1H spectrum indicates structural hydrogen in the sample. This sample was redissolved in D_2O and recrystallized before neutron diffraction experiments.

4.3 Low- and High-Temperature Structure and Refinement Results

High-resolution neutron powder diffraction measurements were collected at the Los Alamos Neutron Scattering Center (LANSCE) on the NPDF instrument. Approximately 7 grams of $RbHSeO_4$ powder solid acid sample were carefully packed in a glove box (Ar atmosphere) into a cylindrical vanadium can and sealed with lead wire. Powder diffraction data were collected for 4 hours in the low-temperature phase (actual collection temperature, T = 333 – 316K), and for 4 hours in the high-temperature phase (T = 440K). Rietveld refinements were completed with the GSAS Rietveld code [2, 3].

4.3.1 Refinement at 333 – 316 K

Neutron diffraction data collected at T = 333 – 316K were used to refine the Makarova (1993) structure, B1 for completeness [4] (Figure 4-2). The least-squares refinement included lattice parameters, U_{ani}, atom coordinates for all atoms, absorption/extinction, scaling, and profile parameters as well as March-Dollase preferential orientation ratios and fractions for the {100} directions (272 refined parameters total). The background was graphically fitted to a 36-term shifted Chebyschev polynomial for each histogram. In the initial stages, each of the atomic coordinates, thermal, and lattice parameters were refined independently and successively updated in subsequent cycles. The final refinement converged to $\chi^2 = 2.864$ for 136 variables (Table 4-2). For estimating standard uncertainties, U_{ani} and atomic coordinates were refined independently. The refinement results represent the standard uncertainties and values from both of these independent refinements (Table 4-1). The atomic coordinates remained nearly identical between refinements; however, U_{ani} parameters vary widely between refinements.

Atom	x	y	z	U_{11}	U_{22}	U_{33}	U_{12}	U_{13}	U_{23}
Rb1	0.99927(30)	0.0034(10)	0.4936(5)	0.051(4)	0.0339(31)	0.036(4)	0.0063(26)	-0.002(4)	-0.0171(29)
Rb2	0.16421(27)	0.5697(11)	0.0869(7)	0.048(6)	0.061(5)	0.094(6)	0.019(4)	0.000(4)	0.004(4)
Rb3	0.83439(29)	0.4160(10)	0.0929(6)	0.053(5)	0.048(5)	0.040(4)	0.0220(35)	0.0107(35)	0.0053(34)
Se1	0.00215(24)	0.0214(9)	0.0009(5)	0.0302(33)	0.0308(32)	0.060(4)	0.0078(27)	-0.004(4)	0.0061(30)
Se2	0.16692(19)	0.6910(10)	0.5751(6)	-0.0034(29)	0.041(4)	0.091(5)	-0.0066(26)	0.0095(25)	-0.0155(30)
Se3	0.83100(21)	0.3037(8)	0.5784(5)	0.052(5)	0.061(4)	0.022(4)	0.0173(34)	-0.0011(31)	0.0221(29)
O1	0.03249(34)	0.2867(11)	0.8673(8)	0.057(7)	0.024(5)	0.067(6)	-0.005(4)	-0.013(4)	0.013(5)
O2	0.97062(33)	0.7002(13)	0.8563(7)	0.041(6)	0.056(5)	0.022(5)	-0.028(4)	0.014(4)	0.012(4)
O3	0.06138(35)	0.9334(12)	0.1141(8)	0.052(6)	0.028(5)	0.073(6)	0.010(4)	0.010(4)	-0.018(4)
O4	0.9355(4)	0.0534(13)	0.1068(9)	0.055(6)	0.035(5)	0.072(6)	0.003(4)	0.017(5)	0.005(4)
O5	0.1933(4)	0.4716(12)	0.7124(9)	0.059(6)	0.012(5)	0.102(8)	-0.005(4)	-0.040(5)	-0.007(4)
O6	0.80313(29)	0.5138(14)	0.7155(8)	0.039(5)	0.092(7)	0.054(6)	0.060(5)	0.013(5)	-0.005(5)
O7	0.2343(4)	0.8922(14)	0.4693(7)	0.085(8)	0.085(7)	0.023(5)	-0.008(5)	-0.003(4)	0.017(5)
O8	0.77166(28)	0.1064(16)	0.4680(9)	0.020(5)	0.096(8)	0.088(7)	0.022(5)	-0.016(4)	0.011(6)
O9	0.13010(27)	0.9198(12)	0.7201(8)	0.008(5)	0.031(5)	0.125(8)	-0.0087(33)	-0.010(5)	0.016(5)
O10	0.86813(28)	0.1002(13)	0.7135(7)	0.047(6)	0.042(6)	0.032(5)	-0.003(4)	0.023(4)	-0.001(4)
O11	0.1072(4)	0.5240(14)	0.4489(7)	0.092(8)	0.063(6)	0.026(4)	0.003(5)	-0.040(5)	0.006(4)
O12	0.89814(34)	0.4641(15)	0.4520(8)	0.056(7)	0.087(7)	0.035(6)	0.007(5)	-0.002(4)	0.005(5)
D1	0.99759(31)	0.5439(13)	0.8807(6)	0.052(5)	0.059(5)	0.044(4)	0.036(4)	-0.015(4)	-0.039(4)
D2	0.15661(30)	0.1348(13)	0.7096(7)	0.024(6)	0.060(6)	0.071(7)	0.007(4)	-0.007(4)	0.011(4)
D3	0.84080(32)	0.8826(12)	0.7131(8)	0.054(6)	0.068(6)	0.066(6)	0.001(4)	0.003(4)	0.030(4)

Table 4-1. Atomic Coordinates and Thermal Displacement Parameters of $RbDSeO_4$ at 333 – 316K

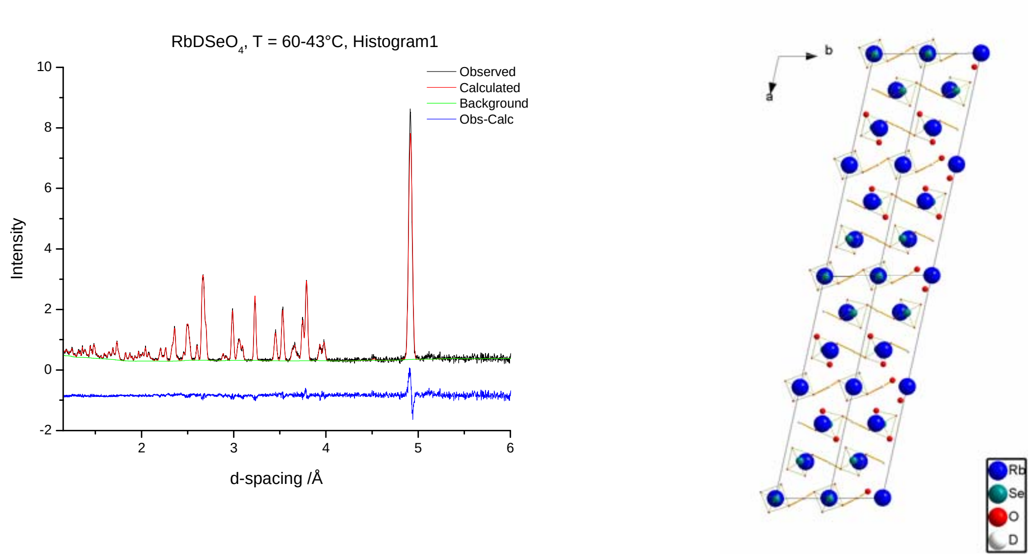

Figure 4-2. (left) Neutron diffraction data refinement, RbDSeO$_4$, T = 333 – 316K (60 – 43°C), bank 1. (right) Crystal structure viewed along the 001 direction. Selenate groups are linked via fully ordered asymmetric, single minimum hydrogen bonds.

4.3.2 Refinement at 440 K

Neutron diffraction data collected at T = 440K were used to refine the Jirak, Merinov, and Belushkin CsHSO$_4$ I4$_1$/amd structures [5-7]. The least-squares refinement began by preparing a generic refinement without oxygen or deuterium positions. The generic least squares refinement included lattice parameters, U_{ani}, atom coordinates for rubidium and selenium atoms, absorption/extinction, scaling, and profile parameters. The background was graphically fitted to a 36-term shifted Chebyschev polynomial for each histogram. In the initial stages, each of the atomic coordinates, thermal, and lattice parameters were refined independently and successively updated in subsequent cycles. The final generic refinements each converged to χ^2 = 8.713 for 6 variables.

	333 – 316 K	440 K
Space group:	B1	I41/amd
a (Å)	19.87118(24)	5.70269(16)
b (Å)	4.63816(7)	5.70269
c (Å)	7.58133(10)	14.1152(7)
α	90.7348(10)	90
β	90.0498(9)	90
γ	102.8105(10)	90
Z	6	4
V (Å)	681.285(10)	459.034(26)
R_p x 100	2.24	1.60 Belushkin 1.72 Jirak 1.60 Merinov
R_{wp} x 100	3.26	2.47 Belushkin 2.72 Jirak 2.46 Merinov
χ^2	2.864	1.676 Belushkin 2.025 Jirak 1.660 Merinov

Table 4-2. Crystal Data and Structure Refinement Parameters for $RbDSeO_4$ at 333 – 316K and 440K

Once the generic refinement was prepared, each structure was subjected to a refinement using the profile parameters and fitted background from the generic refinement. The least-squares refinement on each structure included only the anisotropic thermal parameters for all atoms and atomic coordinates. In the case of the Belushkin and Merinov structures, the fractional occupancy of the split deuterium positions was also refined with the constraint that the structure contain the stoichiometric number of deuteriums (Z=4, $RbDSO_4$, 4 total deuteriums per unit cell). The Merinov structure final refinement converged to χ^2 = 1.66 for 7 variables. The Belushkin structure final refinement converged to χ^2 = 1.676 for 23 variables, while the final Jirak refinement converged to χ^2 = 2.025 for 4 variables (Tables 4-2 & 4-3).

The difference in χ^2 between the three structures is not significant enough to decide which structure is the best description of $RbDSeO_4$, as in the Belushkin and Merinov structures, the split oxygen and deuterium site model adds more parameters for refinement so the χ^2 value is not necessarily a valid comparison of the three structures.

An evaluation on whether or not these added sites are significant to the refinement can offer a solution. Similar to the analysis presented in Chapter 3, the Hamilton test, the Merinov and Belushkin structures split the oxygen and deuterium sites, and either of these models can be used as the unconstrained model [8]. The Jirak model constrains the oxygen and deuterium sites to a single site each.

(Jirak) O and D atoms have a single crystallographic site each: O—32i, D—16f.

(Merinov) The O atoms are split into two sites: 32i and 16h, and the D site is split between a 16f site and a 8e site.

(Belushkin) The O atoms are split into two 32i sites and the D atoms are split into 16f and 8e sites.

The number of parameters refined in these three cases were $m_{Jirak} = 80$, $m_{Merinov} = 91$, and $m_{Belushkin} = 94$. There were 329 reflections. The R factors achieved were $R_{Jirak} = 0.0272$, $R_{Merinov} = 0.0246$, and $R_{Belushkin} = 0.0247$.

Let us test the hypothesis:

H_0: O and D each reside on a single crystallographic site.

To test this hypothesis, the R factor for the restrained model (Jirak) corresponds to the hypothesis and the unrestrained model (Belushkin or Merinov). The appropriate R-factor ratio is

$$\Re = \frac{R_{Jirack}}{R_{Merinov}} = \frac{0.0272}{0.0246} = 1.106$$

$$\Re = \frac{R_{Jirack}}{R_{Belushkin}} = \frac{0.0272}{0.0247} = 1.101 .$$

The dimension of the hypothesis is in the first case, $m_{\text{Merinov}} - m_{\text{Jirack}} = 11$ and in the second case, $m_{\text{Belushkin}} - m_{\text{Jirack}} = 14$, and the number of degrees of freedom for the refinement is $n - m \approx 235$. The appropriate $\Re$ value interpolated from the Hamilton tables,

$$\Re_{11,235,0.005} = 1.021,$$

suggests that the hypothesis that the oxygen and deuterium atoms each occupy a single crystallographic site can be rejected at the 0.005 level. The results of this neutron diffraction experiment are in favor of the split oxygen and deuterium site model of Merinov and Belushkin.

As the split oxygen and deuterium site model is favored in this set of refinements, a consideration of the refined parameters should help determine which of the two possible structures best describes the sulfate and deuterium positions. The refined occupancies of the deuterium sites in the Merinov structure on the 16f and 8e sites approximates a 3 to 1 split of deuteriums in the unit cell on these sites. The Belushkin refined occupancies of the deuterium sites refines to almost ¼ deuterium per unit cell. Thermal parameters between the two structures cannot support one structure over the other, as these parameters in the Merinov structure for the U_{22} component of one oxygen and one deuterium site are excessively large while that of the Belushkin structure is excessively large, in the U_{11} and U_{22} components of an oxygen site (Table 4-3). The distinction between the Merinov and Belushkin models cannot be made with this approach; however, the split oxygen and deuterium model is definitely the best description of the sulfate group disorder in the high-temperature structure.

Jirak Structure

Atom	Site	x	y	z	Site Occ.	U_{11}	U_{22}	U_{33}	U_{12}	U_{13}	U_{23}
Rb	4b	0.5	0.25	0.125	1	0.18733	0.18733	0.18361	0	0	0
Se	4a	0	0.75	0.125	1	0.17766	0.17766	0.12615	0	0	0
O	32i	0.2326(4)	0.7171(9)	0.06563(18)	4	0.31931	0.43307	0.30308	0.156	0.19583	-0.06893
D	16f	0.1838(18)	0.5	0	1	0.74152	0.8	0.0777	0	0	-0.09791

Belushkin Structure

Atom	Site	x	y	z	Site Occ.	U_{11}	U_{22}	U_{33}	U_{12}	U_{13}	U_{23}
Rb	4b	0.5	0.25	0.125	1	0.2212(19)	0.2212(19)	0.1316(34)	0	0	0
Se	4a	0	0.75	0.125	1	0.1541(14)	0.1541(14)	0.1731(32)	0	0	0
O1	32i	0.06125	0.56652	0.20418	2	0.179(9)	0.156(4)	0.175(5)	0.074(5)	0.091(6)	0.132(5)
O2	32i	0.06163	0.45727	0.1583	2	0.314(17)	0.0850(34)	0.556(18)	0.108(9)	-0.007(23)	-0.010(4)
D1	16f	0.25	0.55874	0.25	0.93104	0.80(10)	0.80(5)	0.219(15)	0	-0.075(17)	0
D2	8e	0	0.25	0.10457	0.06894	-0.020(12)	-0.076(6)	0.33(4)	0	0	0

Merinov Structure

Atom	Site	x	y	z	Site Occ.	U_{11}	U_{22}	U_{33}	U_{12}	U_{13}	U_{23}
Rb	4a	0	0.75	0.125	1	0.18036	0.18036	0.20793	0	0	0
Se	4b	0.5	0.25	0.125	1	0.15177	0.15177	0.18841	0	0	0
O1	32i	0.7219(11)	0.2396(21)	0.04054(28)	2	0.50409	0.8	0.10039	-0.4	0.1371	0.07209
O2	16h	0.7392(5)	0.25	0.08296(25)	2	0.09989	0.32386	0.30039	0	0.13588	0
D1	16f	0.6415(11)	0.5	0	0.77508	0.09862	0.8	0.58909	0	0	0.4
D2	8e	0	0.25	0.0573(11)	0.22494	0.46217	0.01849	0.29034	0	0	0

Table 4-3. Atomic Coordinates and Thermal Displacement Parameters of $RbDSeO_4$ at 440K in the Jirak, Belushkin, and Merinov structures

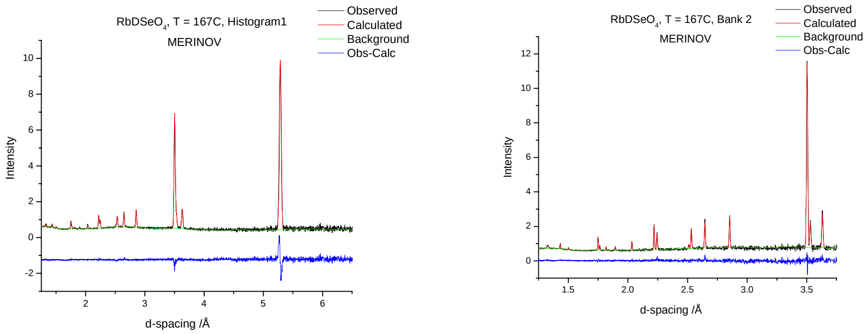

Figure 4-3. Neutron diffraction data refinements of $RbDSeO_4$, T = 440K (167°C), bank 1 and 2 in the Merinov structure.

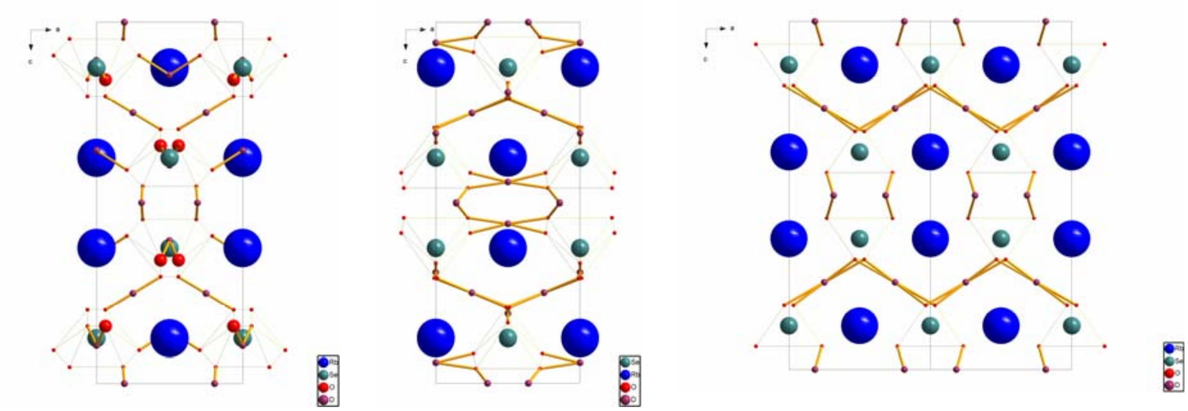

Figure 4-4. Belushkin (left), Merinov (center), and Jirak (right) structures of $RbDSeO_4$

4.4 Pair Distribution Function Analysis

The pair distribution function indicates sharp features commensurate with selenate tetrahedral distances in both the high-temperature and room-temperature phases (Figure 4-5). For the superprotonic phase, PDF peaks at positions longer than 3 Å are broadened beyond what would be expected from the Bragg diffraction refinement.

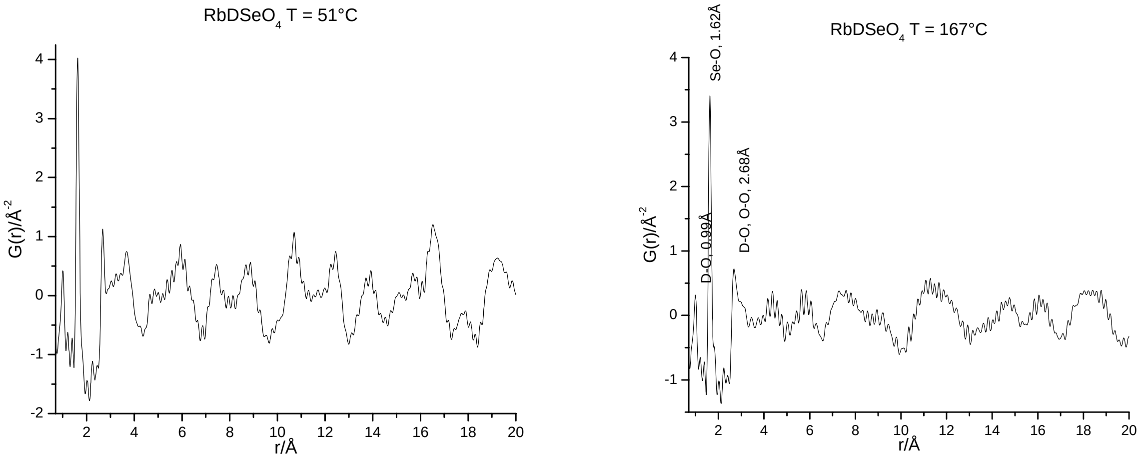

Figure 4-5. Pair Distribution Function for $RbDSeO_4$ at (left) T = 333 – 316K and (right) T = 440K. The high-temperature structure loses long-range correlations.

4.5 Entropy Evaluations

To consider the change in entropy associated with the B1 to $I4_1/amd$ phase transition of superprotonic $RbDSeO_4$, differential scanning calorimetery (DSC) data were collected on both $RbDSeO_4$ or $RbHSeO_4$ and $CsHSO_4$ with the same experimental parameters, calibrations, and scan rate of ¼ K min^{-1}. An approximate value of 10 J/molK was arrived at by closed-volume experiments and regular alumina crucible (covered, ambient pressure) experiments (Figures 4-7 & 4-8). This value can be directly compared to the $CsHSO_4$ value of 13.7 J/molK, as the same calibrations and technique was used for both measurements (Figure 4-6). Comparing DSC peak areas between measurements on $CsHSO_4$ and $RbHSeO_4$ allowed complex peak fittings to be interpreted using the simple $CsHSO_4$ transition and enthalpy value as a standard (Figures 4-6 & 4-7).

Various attempts at separating the multiple phase transitions that $RbDSeO_4$ undergoes has come to a consensus that there are at least two phase transitions, the first of which has a transition enthalpy of approximately 10 J/molK (Figures 4-7 & 4-8). The second transition has a transition enthalpy of between 7.29 – 12 J/molK. Values in the literature for the entropy of the $RbHSeO_4$ phase transition do not resolve the two processes identified in this work at temperatures between ~ 150 – 170°C. Friesel et al, reports an entropy value of 23.4 J/molK with a transition temperature of 447 K [9]. This entropy value would suggest an overall number of configurations, Ω, to be greater than 16, which is unlikely given the symmetry of the superprotonic phase shown in this work. From Friesel's work, the transition temperature of $RbHSeO_4$ has a negative pressure dependence from 0 – 0.4 GPa (Tsp = 159°C, P = 0.4 GPa) and at pressures higher than 0.4 GPa, the transition temperature increases with pressure. The transition temperature's negative pressure dependence could help explain the lower transition temperature in the closed-volume DSC experiment (Figure 4-7); however, at ambient pressures, the deuterated analog continues to exhibit a lower transition temperature than $RbHSeO_4$ (Figure 4-10).

This unusual isotope effect on the transition temperature and the splitting of a single transition into two transitions has been documented in the literature [10] (Figure 4-11). Poprawski measured a transition entropy at 433 K (160°C) of 8 J/molK and 11 J/molK at 449.5 K (176.5°C) by DSC at a scan rate of 1 K/min. Similar measurements on $RbHSeO_4$ yielded a transition entropy of 24 J/molK. This work shows that both $RbDSeO_4$ and $RbHSeO_4$ transform in two major steps if scanned at a slow enough heating rate (1/4 K/min) and that the first step is a superprotonic phase transition which itself is a two-step transition into the $I4_1/amd$ space group through the B2 space group. The second transition is a decomposition or incongruent melt transition, as X-ray diffraction patterns indicate lower symmetry (Figures 4-8, 4-9) through this second transition.

Selenate groups are linked by disordered hydrogen bonds forming one-dimensional zigzag chains in the B2 monoclinic phase of $RbDSeO_4$. The positions of oxygen atoms are fixed and the hydrogen bonds are asymmetric (Figure 4-1). For configurational entropy calculations, this lower-temperature phase is considered to have two configurations for a configurational entropy, $S_{config} = R\ln(2) = 5.76\frac{J}{mol\,K}$. Contrary to expectations from the literature, the transition at T = 155°C is not from the B2 phase to a higher-symmetry phase, but possibly a set of transitions from $B1 \longrightarrow B2 \longrightarrow I4_1/amd$ phase. Differential scanning calorimetry data suggests of a pair of transitions that cannot be clearly resolved by ¼ K/min scan rate (Figure 4-7). Here we attribute the full measured 10 J/molK to the $B1 \longrightarrow B2 \longrightarrow I4_1/amd$ set of transitions, as it is believed at slow scan rates the transitions are indistinguishable. The starting phase in this sequence of phase transitions is the fully ordered B1 phase with zero configurational entropy. On first heating, X-ray diffraction data fails to capture the B2 phase, further supporting the immediate transition sequence B1⟶B2⟶$I4_1$/amd (Figure 4-9). X-ray diffraction data on cooling, however, indicate the B2 phase as seen in Figure 4-9 (right).

As $RbDSeO_4$ has been shown to exist at high temperatures in one of the split oxygen/split deuterium models, the configurational entropy,

$$S_{config} = R\ln(\Omega) = R\ln(4) = 11.5\frac{J}{mol\,K},$$

is the overall transition entropy, ΔS_{sp} , of the superprotonic phase. The calculated configurational entropy value of 11.5 J/molK is in excellent agreement with the measured value of 10 J/mol K.

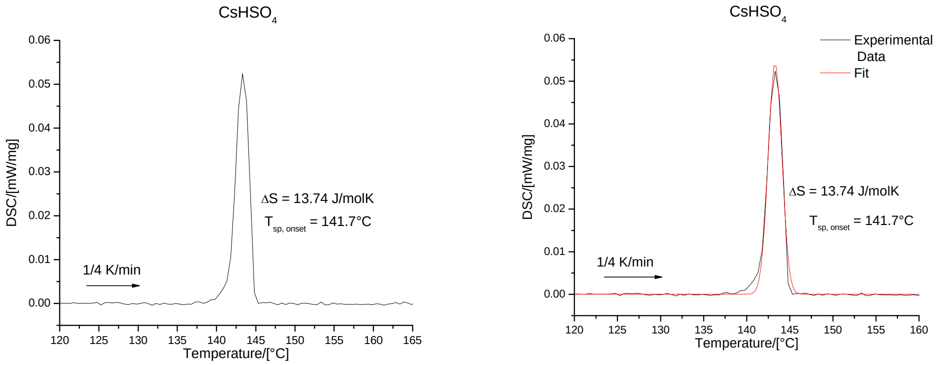

Figure 4-6. $CsHSO_4$ differential scanning calorimetry data used as a standard for interpreting peak area values in fitting the complicated set of transitions in $RbDSeO_4$

Peak Center of Gravity [°C]	Area Fit [W/g °C]	Δ H [J/g]	Tonset [°C]	ΔS [J/molK]
143.29	0.07806	24.79	141.7	13.74

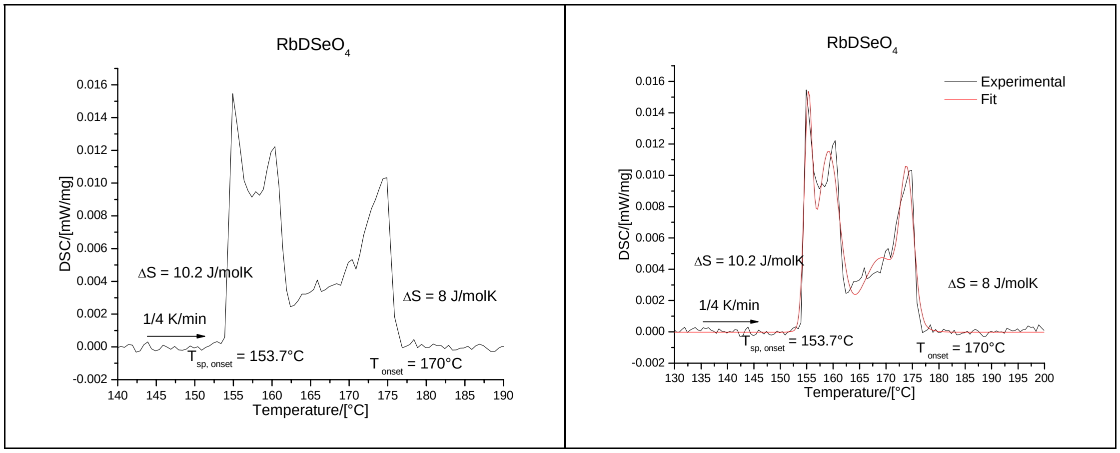

Figure 4-7. RbDSeO$_4$ differential scanning calorimetery data fitted to four peaks. The first two peaks are considered to be due to the transition from the B2 to I4$_1$/amd structure.

Peak Center of Gravity [°C]	Area Fit [W/g °C]	Δ H [J/g]*	Tonset[°C]	ΔS [J/molK]
155.26	0.01816	5.77	153.7	3.11
159.10	0.04132	13.12	158	7.01
169.15	0.02911	9.24	166	4.85
173.97	0.01933	6.14	171	3.18

*Values extrapolated from fit value for CsHSO$_4$ and enthalpy value

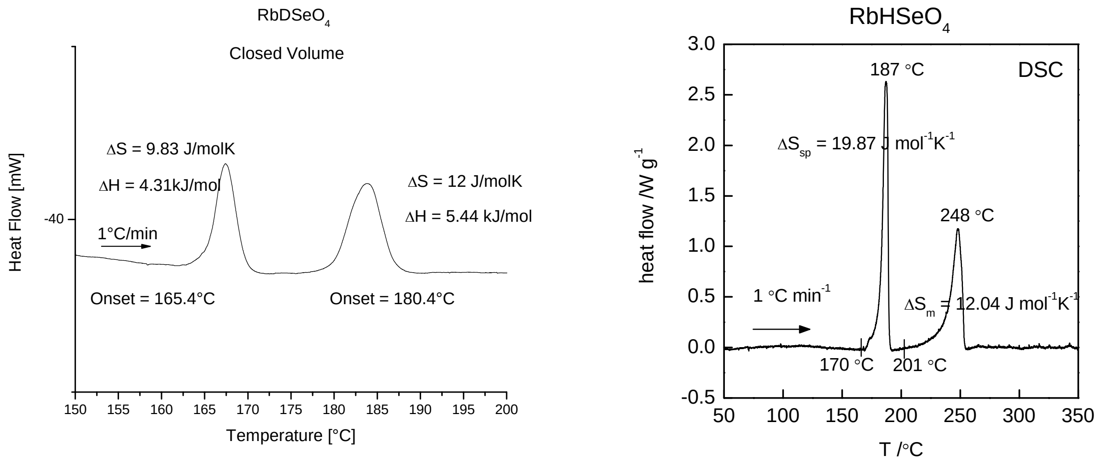

Figure 4-8. RbDSeO$_4$ closed volume versus ambient pressure (RbHSeO$_4$) differential scanning calorimetry data. (left) Closed volume experiments on deuterated samples clearly separate the B1→I4$_1$/amd and decomposition transitions. Previous work on RbHSeO$_4$ was unable to separate these transitions and assigned all of the transition entropy to a single transition as in the ambient pressure, 1K/min DSC scan of RbHSeO$_4$ (right).

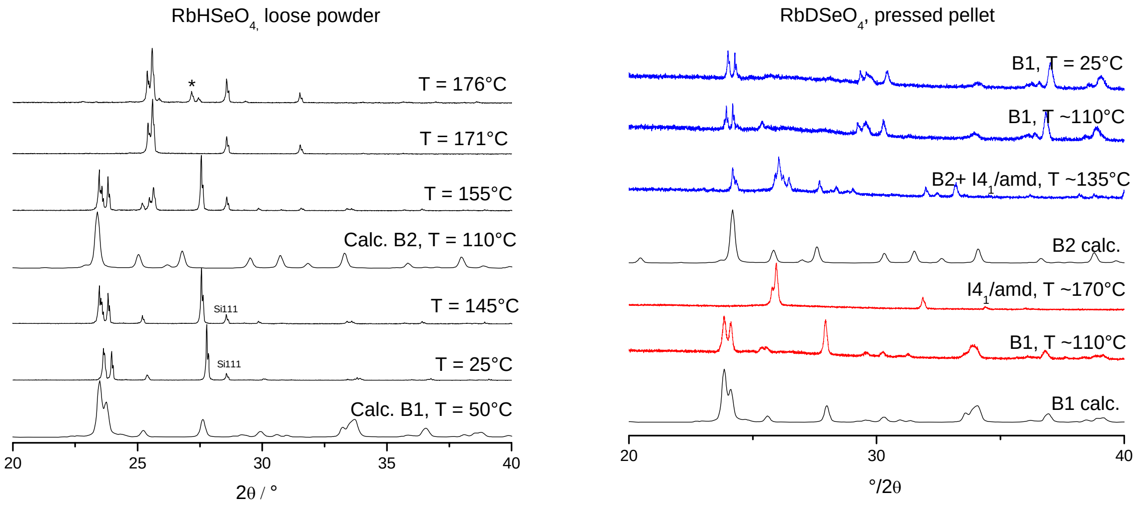

Figure 4-9. (left) RbHSeO$_4$ X-Ray Diffraction Data. The B1 phase is present from T = 25°C to 155°C where the I4$_1$/amd phase emerges. At T = 176°C, RbHSeO$_4$ transitions again to possibly a lower symmetry or possibly phase separation. Calculated patterns of RbHSeO$_4$ B1 and B2 space group are included to illustrate the B1 → B2 transition does not appear on heating. The transition sequence, B1 → I4$_1$/amd is indicated. (right) RbDSeO$_4$ X-Ray Diffraction Data on Pressed Pellet Kapton Sealed Sample. Calculated patterns of RbDSeO$_4$ B1 and B2 space group (shifted to account for sample height error on pellet sample) are included to illustrate the I4$_1$/amd → B2 → B1 transition sequence is detectable on cooling (cooling cycle in blue). First heating cycle (red) shows no evidence of B2 phase. Evidence of the B2 phase is also present in ACIS data.

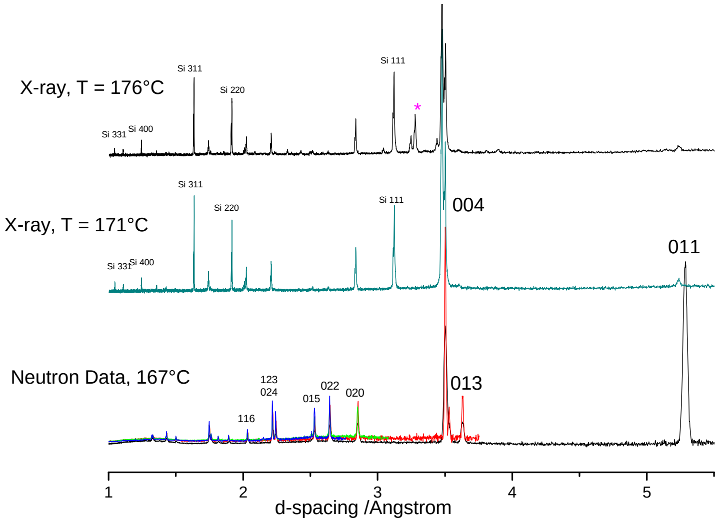

Figure 4-10. Neutron and X-ray data for RbDSeO$_4$ (neutron) and RbHSeO$_4$ (X-ray). Neutron diffraction pattern includes 011 and 013 peaks not present with X-ray diffraction due to the similarity in scattering power of Rb and Se. X-ray diffraction pattern at 176°C shows an additional peaks at 3.23 and 3.27 Å d-spacing indicting the I4$_1$/amd phase exists between two phase transitions from B1 (or B2)→ I4$_1$/amd and I4$_1$/amd ⟶unknown phase of lower symmetry, possibly phase separation or dehydration.

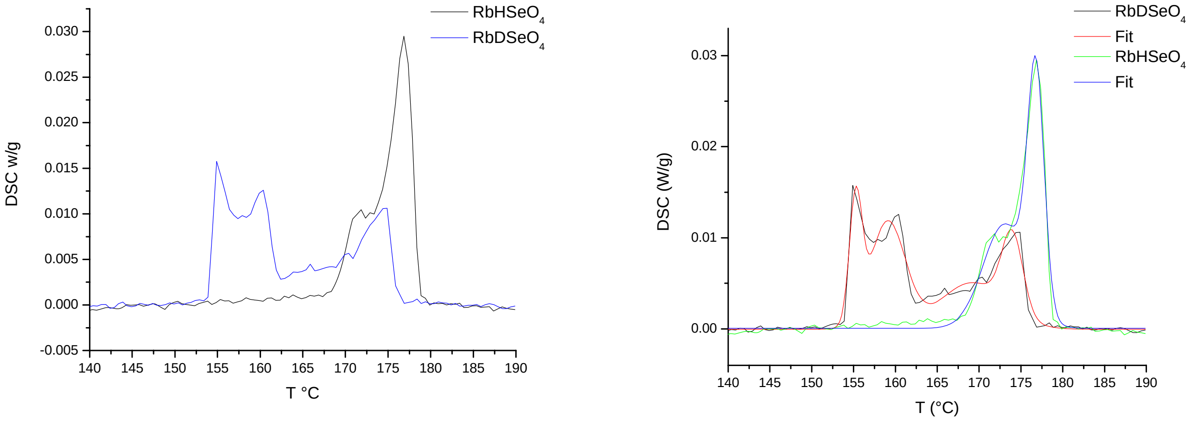

$RbDSeO_4$

Peak Center of Gravity [°C]	Area Fit [W/g °C]	Δ H [J/g]*	T_{onset} [°C]	ΔS [J/mol K]
155.26	0.01816	5.77	153.7	3.11
159.10	0.04132	13.12	158	7.01
169.15	0.02911	9.24	166	4.85
173.97	0.01933	6.14	171	3.18

$RbHSeO_4$

Peak Center of Gravity [°C]	Area Fit [W/g °C]	Δ H [J/g]*	T_{onset} [°C]	ΔS [J/mol K]
173.07	0.05093	15.92	168	7.86
176.79	0.04572	14.29	173	7.29

*Values extrapolated from fit value for $CsHSO_4$ and enthalpy value

Figure 4-11. Isotope effect and transition entropies compared in $RbDSeO_4$ versus $RbHSeO_4$.

4.6 Conductivity

The conductivity of $RbDSeO_4$ has been measured. Due to a possible dehydration/decomposition phase transition at temperatures slightly higher than the B1 ⟶ $I4_1/amd$ transition, the measurement was confined to temperatures 170°C and below. The activation energy in the high-temperature phase is well within the range of values reported for other solid acids. The phase transition from the B1 structure to the B2 structure also yields a small increase in conductivity which is only visible on cycling. The presence of the B2 phase on cycling was confirmed by high-temperature X-ray diffraction on cooling back down from the superprotonic phase (Figure 4-9 (right)). Temperature discrepancies between X-ray diffraction data (Figure 4-9) and conductivity data (Figure 4-12) reflect a difference in heating and cooling rates of 1°C/min for conductivity measurements and hold times of 25 minutes to allow for an X-ray diffraction pattern to be acquired at various temperatures.

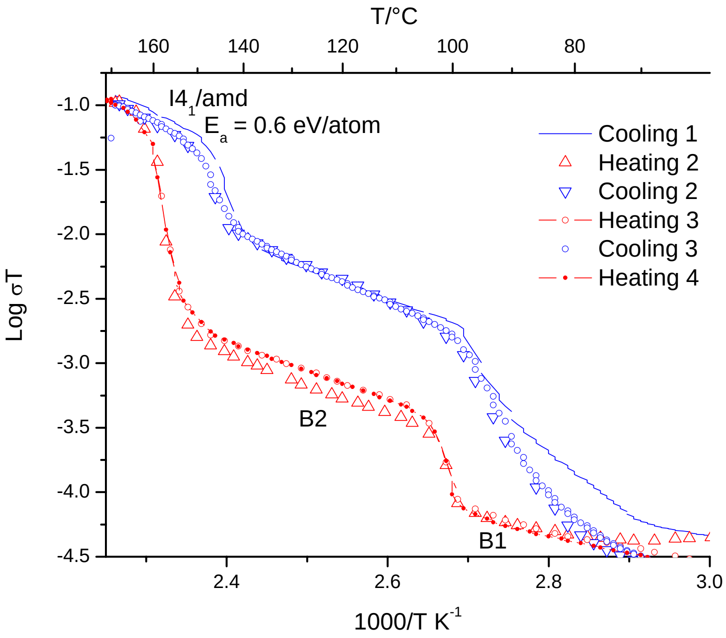

Figure 4-12. Conductivity plot of $RbDSeO_4$ with D_2O humidification in flowing nitrogen

4.7 Conclusions

The superprotonic phase of $RbDSeO_4$ exists in the $I4_1/amd$ structure with split deuterium and oxygen positions. The measured entropy of the transition agrees well with the calculated entropy based on four tetrahedra configurations. The neutron pair distribution function illustrates that the deuterium average position and local position are quite different which further confirms the deuterium mobility in the superprotonic phase. Conductivity and X-ray diffraction measurements confirm the $I4_1/amd \longrightarrow B2 \longrightarrow B1$ transition sequence on cooling despite a lack of evidence of the B2 phase on first heating.

4.8 References

1. Brach, I., D.J. Jones, and J. Roziere. The Crystal-Structure of $RbHSeO_4$ - A Neutron-Diffraction Study of the Para-Electric Phase. Journal of Solid State Chemistry, 1983, **48**(3): 401 – 406.

2. Larson, A.C. and R.B. Von Dreele. "General Structure Analysis System (GSAS)", Los Alamos National Laboratory Report LAUR 86-748 (2000), 2001.

3. Toby, B.H. EXPGUI, a Graphical User Interface for GSAS. Journal of Applied Crystallography, 2001, **34**: 210 – 213.

4. Makarova, I.P. Thermal Vibrations of Atoms and Phase-Transitions in $RbHSeO_4$ and NH_4HSeO_4 Single Crystals. Acta Crystallographica Section B-Structural Science, 1993, **49**: 11 – 18.

5. Jirak, Z., et al. A Neutron-Diffraction Study of the Superionic Phase in $CsHSO_4$. Physica Status Solidi a-Applied Research, 1987, **100**(2): K117 – K122.

6. Merinov, B.V. Localization of Hydrogen Atoms in Protonic Conductors with a Dynamical Disordered Network of Hydrogen Bonds: Effect of Anomalous Manifestation of Hydrogen Atoms on Electron-Density Maps. Kristallografiya, 1997, **42**: 906 – 917.

7. Zetterstrom, P., et al. Structure and Proton Conduction in $CsDSO_4$. Solid State Ionics, 1999, **116**(3 – 4): 321 – 329.

8. Hamilton, W.C. Significance Tests on Crystallographic R-Factor. Acta Crystallographica, 1965, **18**: 502.

9. Friesel, M., B. Baranowski, and A. Lunden. Pressure-Dependence of the Transition to the Proton Conducting Phase of $CsHSO_4$, $CsHSeO_4$ and $RbHSeO_4$ Studied by Differential Scanning Calorimetry. Solid State Ionics, 1989, **35**(1 – 2): 85 – 89.

10. Poprawski, R. Calorimetric Studies of Superionic Phase Transitions in Hydrogen Selenate Crystals. Solid State Communications, 1988, **67**(6): 629 – 631.

11. Boysen, D. Superprotonic Solid Acids: Structure, Properties, and Applications. Ph.D. Thesis. 2004.

Chapter 5 CsH_2PO_4

The existence of a superprotonic phase in CsH_2PO_4 has been debated in the literature. Accurate characterization of CsH_2PO_4 is hampered, as the compound dehydrates without proper humidification in the superprotonic phase. This chapter presents neutron diffraction and neutron pair distribution function (PDF) data, collected in a sealed tube preventing dehydration. The refinement and PDF results show a very clear picture of the superprotonic phase local and average structure. The configurational entropy of the superprotonic phase is discussed with insights from PDF analysis and compared to experimental data.

5.1 Introduction

The superprotonic high-temperature properties of CsH_2PO_4 have been disputed in the literature over the last 10 years. Under ambient conditions, CsH_2PO_4 dehydrates; however, under significant water partial pressure, the superprotonic phase transition is stabilized. Neutron diffraction data was sought to provide resolution on the hydrogen atomic coordinates in an effort to better understand the superprotonic structure.

5.2 Synthesis and Characterization Methods

CsH_2PO_4 powder samples were precipitated out of an aqueous solution containing stoichiometric amounts of Cs_2CO_3 and H_3PO_4 with excessive methanol. The resulting powder was vacuum filtered and dried in an oven at 90°C. X-ray diffraction patterns were collected to verify phase purity after original synthesis and after deuteration (Phillips X’Pert Pro, Cu Kα radiation, 0.02° steps, 11 s/step).

The crystal structure of CsH_2PO_4 in the superprotonic structure is described in the $Pm\bar{3}m$ space group. The hydrogen positions in the unit cell have not been previously determined. The basis of studying proton conductors relies heavily on understanding proton transport and hydrogen bonding. With accurate hydrogen positions, critical hydrogen bond distances can be more precisely evaluated. As hydrogen crystallographic positions are not reliably probed by X-rays, neutron diffraction data was sought to determine the location of the hydrogen atoms in the unit cell. Hydrogen has a tremendously large incoherent cross section (80.26 barns) for neutron collisions while the deuterium isotope of hydrogen is comparatively smaller (2.05 barns). For a neutron diffraction study to be successful on CsH_2PO_4, isotopic exchange from hydrogen to deuterium needs to be accomplished to a high percentage of deuteration. Sample deuteration for this work was achieved (> 99% deuteration) by the following method:

1. Dissolve phase pure solid acid sample, CsH_2PO_4, in D_2O.
2. Freeze dry resulting solution in a flask isolated from ambient air with a glass valve between flask and freeze dryer.
3. Inject D_2O with a syringe through a rubber diaphragm covering inlet orifice which isolates sample from ambient air. Make sure all solid acid is redissolved and then freeze dry.
4. Repeat step 3 at least five times to ensure high deuteration level. Check deuteration level with ^1H and ^2H NMR (Figure 5-1).

Extreme care was taken to isolate CsD_2PO_4 from the atmosphere to avoid isotopic exchange of the deuterated sample with hydrogen in water vapor in ambient air.

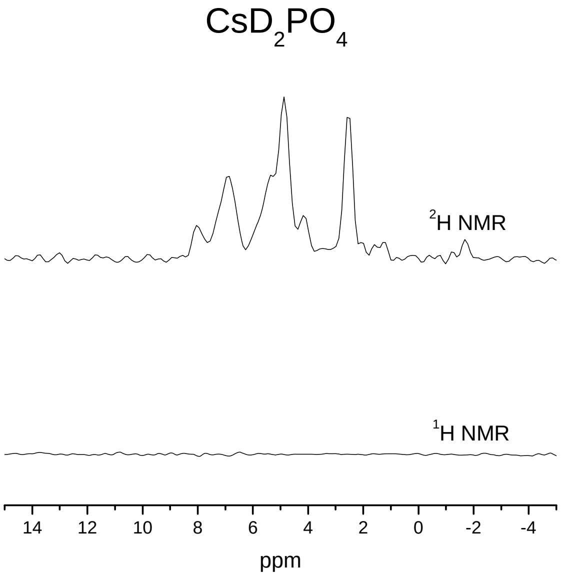

Figure 5-1. Deuteration level check on CsD_2PO_4 neutron sample shows no detectible ^{1}H NMR signal.

5.3 Low- and High-Temperature Structure & Refinement Results

High-resolution neutron powder diffraction measurements were collected at the Los Alamos Neutron Scattering Center (LANSCE) on the NPDF instrument. Approximately 7 grams of CsD_2PO_4 powder solid acid sample were carefully packed in a glove box (Ar atmosphere) into a cylindrical vanadium can and sealed with lead wire. Powder diffraction data were collected for 1.5 hours (T = 325 – 335K), 4.5 (T = 523K), and 6 hours (T = 301 – 305K). Rietveld refinements were completed with the GSAS Rietveld program operated under EXPGUI [1, 2].

5.3.1 Refinements at 301-305 K & 325-335 K

Neutron diffraction data collected at T = 301 – 305K and T = 325 – 335K were used to refine the Preisinger (1994) structure, $P2_1/m$ for completeness (Figure 5-2, Tables

5-1 & 5-2). This room temperature CsH_2PO_4 structure is well-known because this compound has been extensively studied as a ferroelecetric material. The least-squares refinement included lattice parameters, U_{ani}, atom coordinates for all atoms, absorption/extinction, scaling, and profile parameters, as well as March-Dollase preferential orientation ratios and fractions for the {100} directions. The background was graphically fitted to a 36-term shifted Chebyschev polynomial for each histogram. In the initial stages, each of the atomic coordinates, thermal, and lattice parameters were refined independently and successively updated in subsequent cycles. The final refinements converged to $\chi^2 = 3.641$ (T = 301-305K) and $\chi^2 = 2.244$ (T = 325-335K) for 129 variables. Unit cell data reveal an increase in cell volume of 0.41% between 301 – 305 K to 325 – 335 K (Table 5-1).

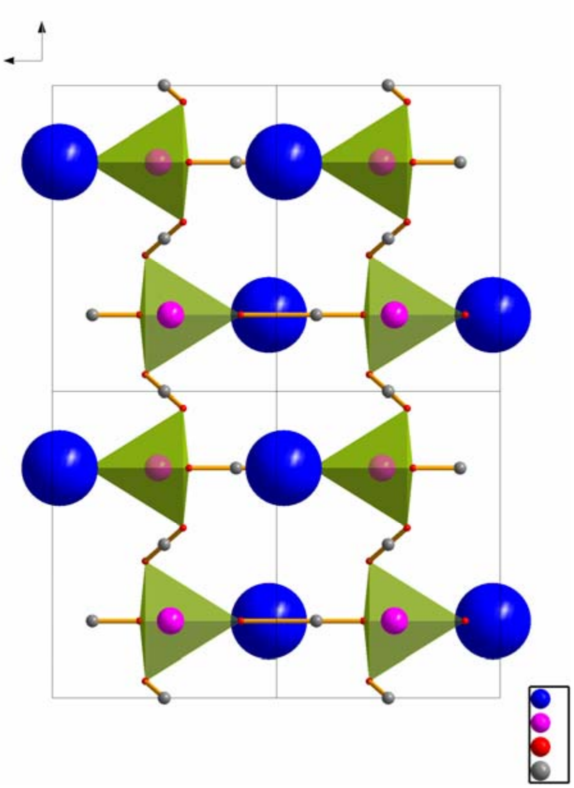

Figure 5-2. CsH_2PO_4 room temperature structure in $P2_1/m$ space group along the [100] direction

	301-305 K	325-335 K	523 K
Space group:	$P2_1/m$	$P2_1/m$	$Pm\bar{3}m$
a (Å)	7.92053(7)	7.92320(13)	4.98425(4)
b (Å)	6.38560(4)	6.40754(7)	4.98425(4)
c (Å)	4.89167(4)	4.88840(6)	4.98425(4)
β	107.7143(7)	107.5353(12)	90
Z	2	2	1
V (Å)	235.6770(20)	236.643(4)	123.8220(30)
R_p x 100	1.55	2.37	1.54
R_{wp} x 100	2.29	3.52	2.47
χ^2	3.641	2.244	1.662

Table 5-1. Crystal Data and Structure Refinement Parameters for CsD_2PO_4 at 301 – 305K, 325 – 335K, and 523K

Temperature	Atom	x	y	z	U_{11}	U_{22}	U_{33}	U_{12}	U_{13}	U_{23}
301-305	Cs	0.26440(20)	0.25	0.03316(30)	0.0318(9)	0.0287(7)	0.0313(7)	0.0	0.0069(8)	0.0
	P	0.23908(20)	0.75	0.52778(29)	0.0287(9)	0.0322(8)	0.0174(6)	0.0	0.0100(7)	0.0
	O1	0.39319(20)	0.75	0.38910(33)	0.0298(9)	0.0471(10)	0.0254(6)	0.0	0.0141(7)	0.0
	O2	0.32206(22)	0.75	0.84342(32)	0.0496(12)	0.0717(11)	0.0202(6)	0.0	0.0142(6)	0.0
	O3	0.12880(19)	0.55437(17)	0.41595(31)	0.0508(9)	0.0340(6)	0.0635(8)	-0.0147(6)	0.0270(7)	-0.0216(6)
	D1	0.35731(19)	0.75	0.17913(29)	0.0448(10)	0.0405(8)	0.0314(7)	0.0	0.0181(6)	0.0
	D2	0.0	0.5	0.5	0.1005(18)	0.0489(11)	0.0459(11)	0.0293(10)	-0.0132(11)	-0.0088(7)
325-335	Cs	0.2667(4)	0.25	0.0364(5)	0.0460(19)	0.0375(11)	0.0425(12)	0.0	0.0099(14)	0.0
	P	0.2380(4)	0.75	0.5284(5)	0.0463(22)	0.0390(13)	0.0304(11)	0.0	0.0146(14)	0.0
	O1	0.39242(34)	0.75	0.3868(5)	0.0438(21)	0.0546(16)	0.0368(11)	0.0	0.0255(14)	0.0
	O2	0.3204(4)	0.75	0.8420(5)	0.0655(26)	0.0862(18)	0.0239(9)	0.0	0.0158(12)	0.0
	O3	0.12684(35)	0.55551(30)	0.4151(5)	0.0691(19)	0.0432(9)	0.0811(14)	-0.0227(12)	0.0377(13	-0.0280(10)
	D1	0.35591(33)	0.75	0.1766(5)	0.0571(19)	0.0485(13)	0.0418(12)	0.0	0.0274(12)	0.0
	D2	0.0	0.5	0.5	0.114(4)	0.0531(17)	0.0585(17)	0.0263(18)	-0.0138(20)	-0.0064(11)
Temperature	**Atom**	**x**	**y**	**z**	**U_{iso}**	**Multiplicity**	**Occupancy**			
523 K	Cs	0.0	0.0	0.0	0.1536(24)	1	1.0			
	P	0.5	0.5	0.5	0.1558(20)	1	1.0			
	O	0.5	0.2260(6)	0.3526(11)	0.1759(33)	24	0.16667			
	D	0.5	0.5	0.0626(23)	0.205(4)	6	0.33333			

Table 5-2. Atomic Coordinates and Thermal Displacement Parameters of CsD_2PO_4 at 301 – 305K, 325 – 335K, and 523K

5.3.2 Refinement at 523 K

Neutron diffraction data collected at T = 523K were used to refine the $Pm\bar{3}m$ structure proposed by Preisinger [3]. The least-squares refinement included background parameters fit to a 10-term shifted Chebyschev for banks 1 and 2 and a 15-term shifted Chebyschev polynomial for banks 3 and 4, cell parameter, U_{iso} for all atoms, atom coordinates for oxygen and deuterium, absorption/extinction, scaling, and profile parameters. Parameters were refined independently initially and successively updated in subsequent cycles. The final refinement converged to a χ^2 = 1.662 for 12 variables (Figure 5-3, Tables 5-1 & 5-2).

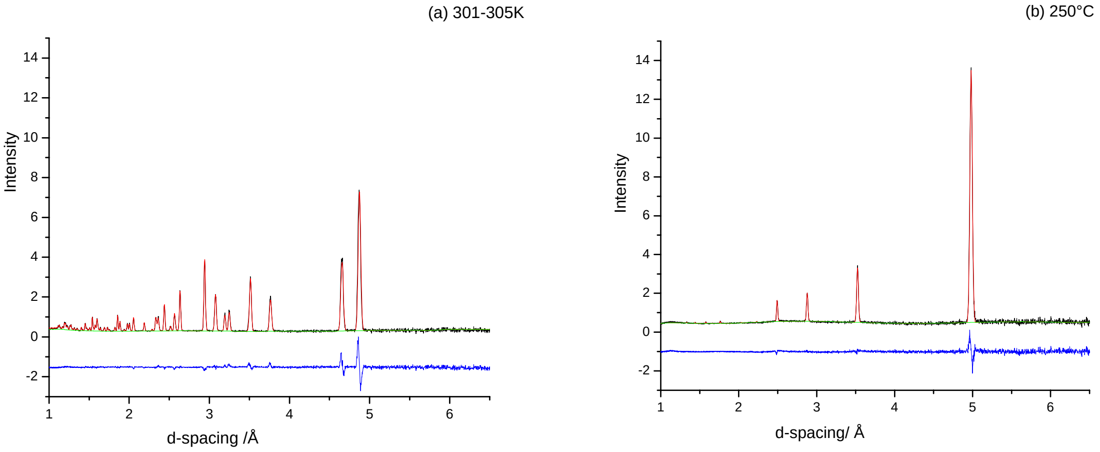

Figure 5-3. Rietveld refinement of powder neutron diffraction data from bank 1 recorded at (a) 301 – 305K and (b) 523K for CsD_2PO_4. Observed (black), calculated (red), background (green), and difference (blue)

Neutron diffraction refinements established the deuterium positions in the CsD_2PO_4 $Pm\bar{3}m$ structure at (½, ½, 0.0626(23)) (Figure 5-4). Oxygen positions have been adjusted from previously reported structures [3, 4].

Neutron diffraction data was also acquired at 550K, at which the superprotonic structure was obtained for the first two hours of data collection. After two hours, the sample degraded into an amorphous material and the overall diffraction pattern and signal to noise degraded with continued collection.

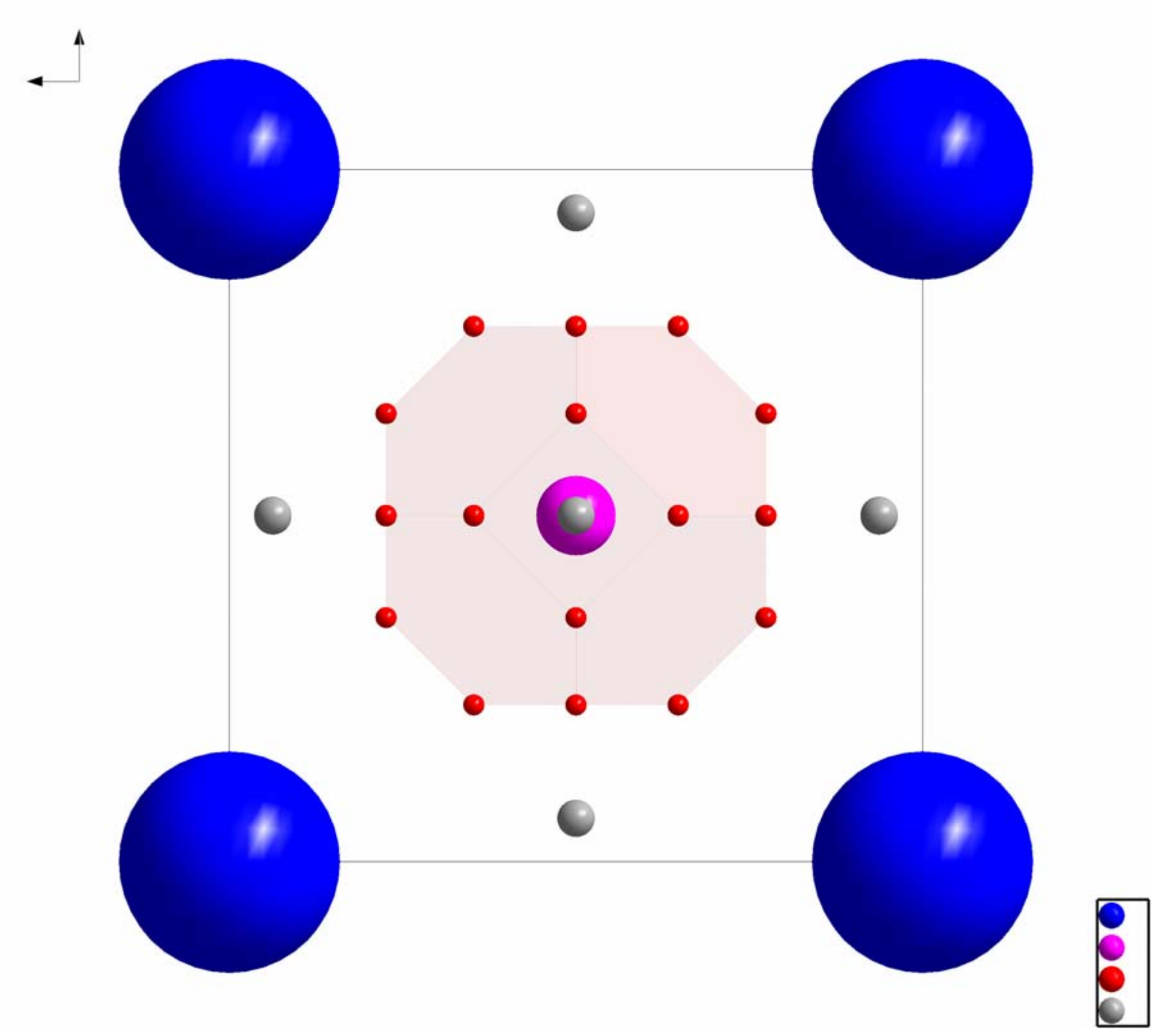

Figure 5-4. CsD_2PO_4 superprotonic structure

5.4 Pair Distribution Function Analysis

The pair distribution function (PDF), G(r), was generated from CsD_2PO_4 neutron diffraction data and illustrates the occurrence of atom pair distances derived from the experimental data. Neutron data obtained of CsD_2PO_4 in the $P2_1/m$ structure produces a pair distribution function with obvious long-range ordering. An examination of the PDF obtained at 30°C has sharp features up to (and possibly beyond) 20 Å which is a span of 4 unit cells (Figure 5-5).

The pair distribution function obtained in the superprotonic phase in the $Pm\bar{3}m$ structure shows broad features outside of the preserved phosphate tetrahedra and hydrogen bonding regime, $r > 3$ Å. The broadness of these features is surprising at first glance given the formally higher symmetry of the superprotonic phase (Figure 5-6).

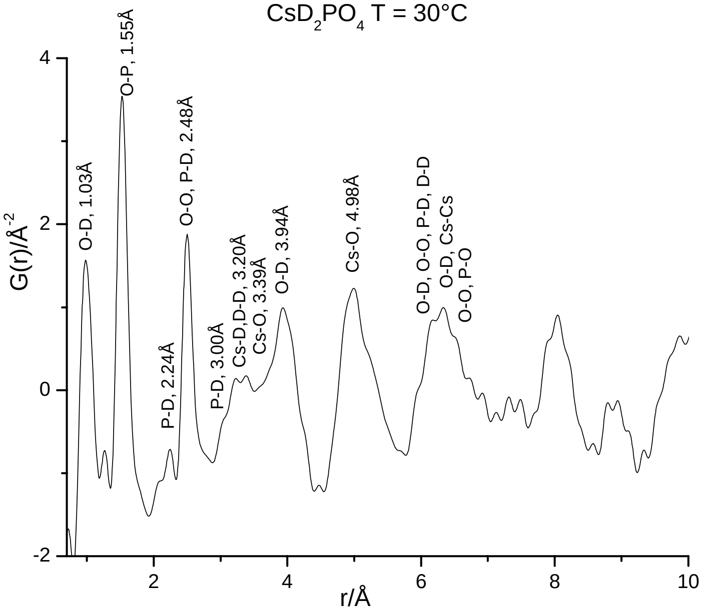

Figure 5-5. CsD_2PO_4 PDF at 30°C in the $P2_1/m$ structure

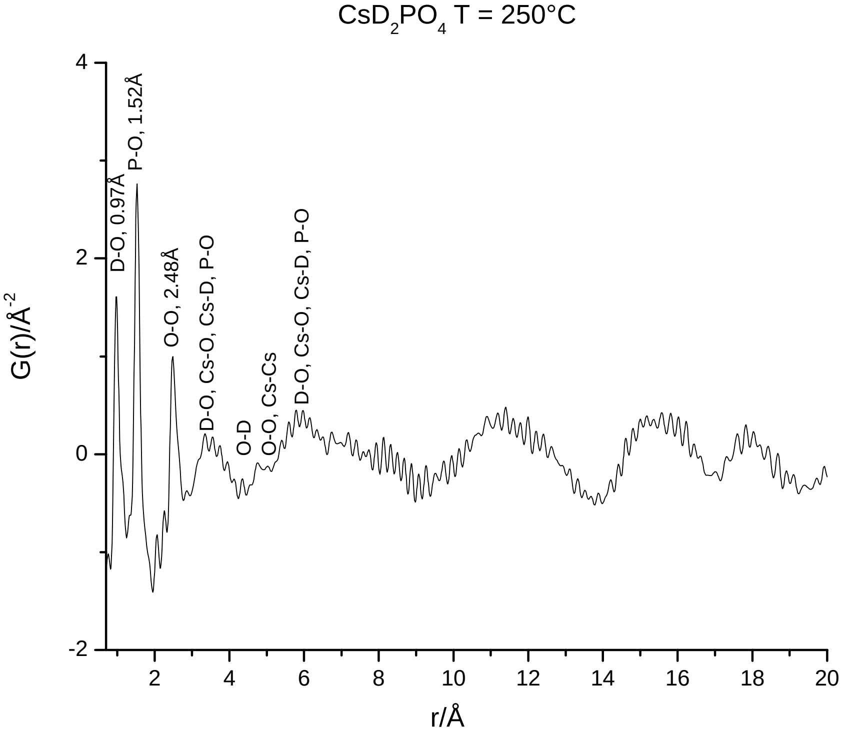

Figure 5-6. CsD_2PO_4 PDF at 250°C in the superprotonic structure

Superprotonic solid acids exhibit liquid-like behavior which undoubtedly enables high proton conductivity. The pair distribution function of superprotonic solid acids is another confirmation of this liquid-like disorder and is a method to better understand proton transport in these unique materials.

5.5 Entropy Evaluations

Previously, Haile et al. [5] evaluated the configurational entropy of CsD_2PO_4 and exposed difficulties in counting the tetrahedral confirmations of the superprotonic solid acid as each tetrahedral unit participates in an average of four hydrogen bonds. Whether or not the orientation of the oxyanion is related to the hydrogen bonds that the group forms has implications on how the available configurations are counted.

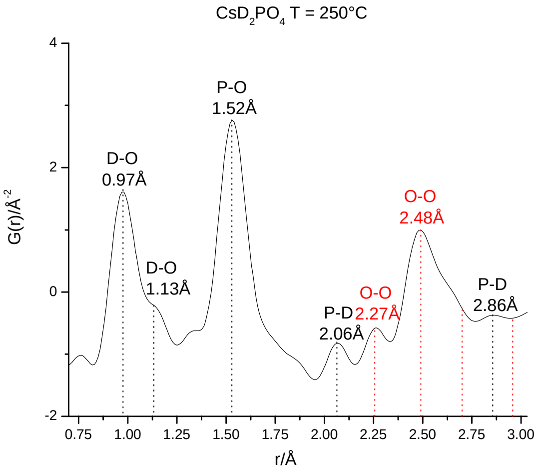

Bond	PDF Bond Length, Å	Bragg Diffraction Structural Refinement Bond Length, Å
D-O	0.97	1.09
D-O	1.13	1.09
P-O	1.52	1.55
P-D	2.06	2.18
O-O	2.27	2.25
O-O	2.48	2.48
P-D	2.86	2.80

Figure 5-7. Pair distribution function of CDP. O-O distances for possible hydrogen bonds are indicated in red. Labeled distances correlate to the refined crystal structure with minor deviations expected from the phosphate tetrahedrons occupying one of the six possible configurations and the deuterium atoms being associated with one oxygen.

As Haile et al. evaluated, the O-O distances formed between oxygen atoms in the superprotonic phase of CsD_2PO_4 ranges from 2.46 to 3.03 Å [5]. Considering the refined oxygen positions presented in this work, the range is 2.25 to 2.95 Å with four hydrogen bond lengths of 2.25, 2.48, 2.68, and 2.95 Å. Prevalent peaks in the pair distribution function support hydrogen bond formation between oxygen atoms with O-O distances of 2.25 and 2.48 Å (Figure 5-7). Utilizing the pair distribution function as a “cutoff” on the length of the hydrogen bonds formed in the superprotonic solid acid, we see that only the two shortest possible bonds should be considered.

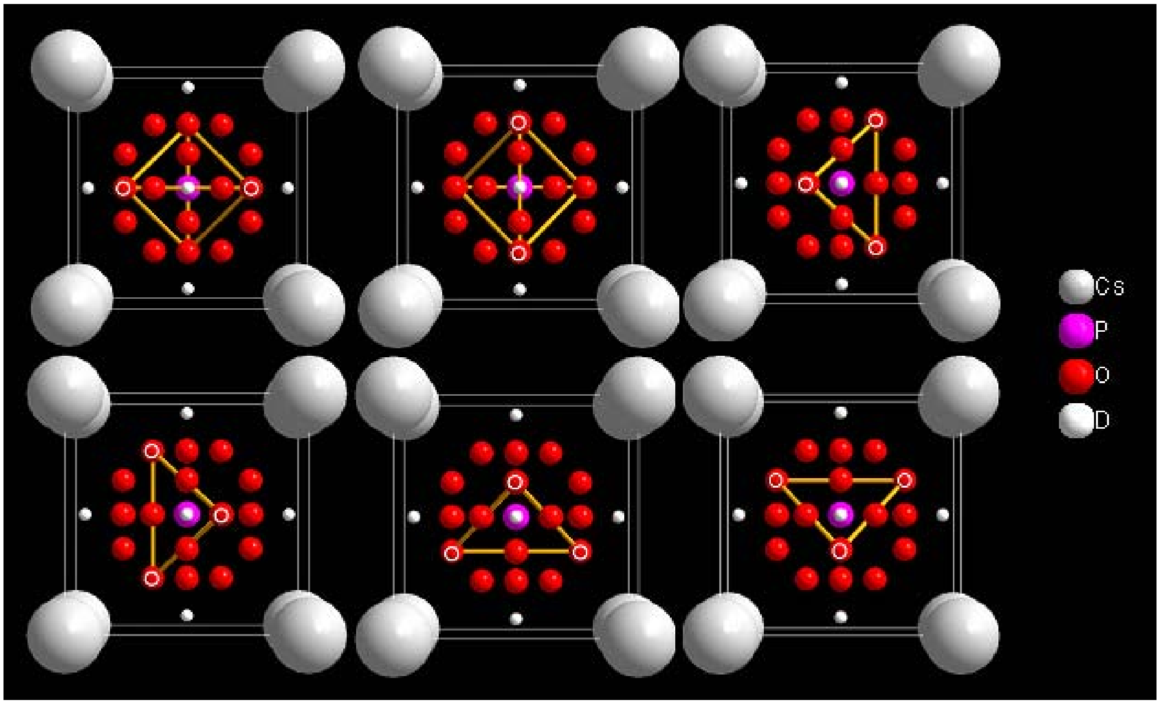

Figure 5-8. Six tetrahedral orientations of CsD2PO4 within the constructs of the Bragg diffraction average structure

Long-range correlations are not strong in the PDF data, and so an enumeration of the total number of configurations available to the phosphate tetrahedron does not necessarily need to be limited to the 6 configurations available in the crystal structure (Figure 5-8), as the only atomic pair distance that is preserved is within the phosphate tetrahedron. This implies that while the average structure of the high-temperature phase of CsD_2PO_4 has definitive bond lengths and orientations, the local structure of the superprotonic phase is structurally more disordered than previously thought.

In light of the PDF, there is no reason why the following two tetrahedral orientations cannot form. The configurational entropy model previously established in the literature should be revisited to account for these other two possible positions (Figure 5-9).

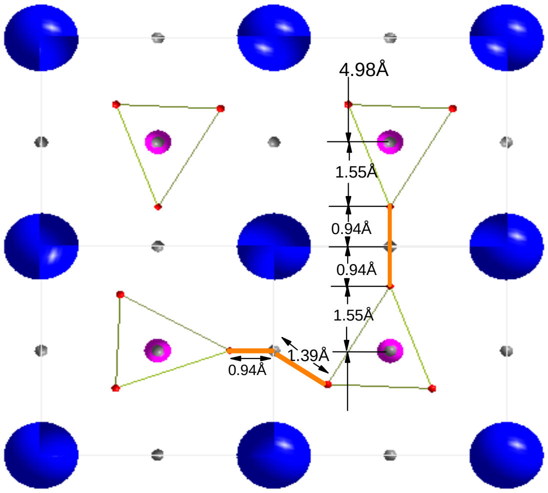

Figure 5-9. Adjacent unit cell face hydrogen bonding not captured in average structure but not prohibited in local structure

Adapting Pauling's Ice rules, Haile et al. outlined the number of configurations,

$$S_{config} = R\ln(\Omega)\,,$$

$$\Omega = \begin{pmatrix} \#of \\ proton \\ configurations \end{pmatrix} \times \begin{pmatrix} probability \\ proton \\ site\,is\,open \end{pmatrix}^{(\#of\ protons)} \times (\#of\ oxygen\ positions)$$

where R is the gas constant (8.314J/molK) and Ω is the total number of configurations including tetrahedral orientations and hydrogen bonds [5]. The contribution to the number of configurations from the hydrogen bond is unambiguously

$$\Omega_H = \begin{pmatrix} 6 \\ 2 \end{pmatrix} \times \left(\frac{4}{6}\right)^{(2)} = 6.67\frac{J}{mol\,K}.$$

Counting the number of tetrahedral orientations for hydrogen bonds formed straight through two unit cells parallel to any unit cell axis, $\Omega_{\text{tetrahedral}} = 4$. For hydrogen bonds formed out of two adjacent unit cell faces, as in Figure 5-8, there are two configurations arrived at from a consideration of the average structure (the top left and center of Figure 5-7) and an additional two configurations as illustrated in Figure 5-8, considering the two ways you can orient the tetrahedra to form an O-O (1.88) plus an O-O (2.33) or alternatively an O-O (2.33) plus an O-O (1.88) (shown in Figure 5-8). The overall number of tetrahedral configurations is 4 for either type of hydrogen bond and so the overall configurational entropy

$$S_{config} = R\ln(4 * \Omega_H) = 27.30\frac{J}{mol\,K}.$$

Subtracting off the lower-temperature disorder, Ω=2 due to hydrogen bond disorder in the P2$_1$/m structure:

$$\Delta S_{sp} = R\ln(4 * 6.67) - R\ln(2) = 21.5\frac{J}{mol\,K}.$$

Previously reported experimental values for the enthalpy of this transition range from 7.6 – 11.9 kJ/mol[5]. All values reported are derived from constant pressure experiments where CDP, prone to dehydration, decomposes shortly after the transition. The enthalpy reported from these constant pressure experiments, even when the dehydration and superprotonic phase transition appear as separate may be an overestimate. The enthalpy value which represents the mode of all values reported estimates the entropy of the transition at 23 J/molK [6]. Closed-volume differential scanning calorimetry data from this work indicates a more modest ΔS = 20.3 J/molK

(Figure 5-10) which is in excellent agreement with the calculated values arrived at drawing greater flexibility in choosing possible tetrahedral arrangements, justified by a loss of long-range order in the PDF (Figure 5-9). As for measurements at constant pressure and constant volume of a condensed phase, it is usually justifiable to ignore the differences between enthalpy and internal energy except at very high pressures. Closed-volume experiments on CDP cannot exceed 2 atms in pressure as the vapor pressure that stabilizes the transition is less than 1 atm and so the difference between internal energy and enthalpy is neglected in this work.

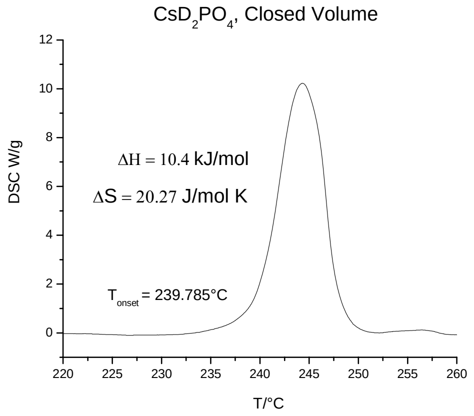

Figure 5-10. CsD_2PO_4 closed-volume DSC

5.6 Pretransition Effects: Three-Site Chemical Exchange via ^{2}H-NMR

CsH_2PO_4 (CDP) and CsD_2PO_4 are isostructural and at room temperature and exist in the $P2_1/m$ space group with two formula units in each cell [7]. The CDP structure has two hydrogen bond lengths of 2.562 Å, H(1) and 2.427 Å, H(2). The O-H(1) …O bonds link tetrahedral PO_4 groups along the a axis and are ordered. The O-H(2) …O bonds form zigzag chains along the ferroelectric b axis and seem to be disordered above Tc = 40°C.

Topic et al. showed using ^{2}H NMR that the two H(1) deuterons are chemically and physically equivalent while the two H(2) deuterons are chemically equivalent but physically nonequivalent in deuterated CDP crystals [8].

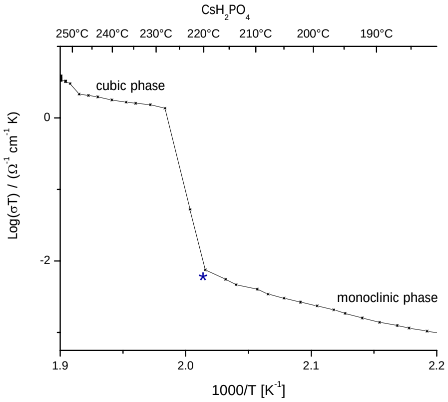

Figure 5-11. ACIS graph of CsH_2PO_4 exhibiting a superprotonic phase transition*.

At temperatures higher than previously studied via ^{2}H NMR, a superprotonic phase transition exists, (Tsp = 230°C), which is characterized by an increase in protonic conductivity by several orders of magnitude (Figure 5-11). This high-temperature superprotonic phase is cubic with CsCl structure, as discussed earlier in this chapter. As the mobility of the proton species is high in this compound, indications of increased motion prior to the phase transition may exist which would include tetrahedral librations, motional averaging of the proton sites, and possibly chemical exchange between the three proton sites.

In this work, we simulate three-site exchange between the single H(1) deuteron and two H(2) deuteron types, in an attempt to describe the exchange frequency between sites prior to the phase transition.

A 500 MHz Bruker NMR (11.7 T) spectrometer was utilized to collect ^{1}H, ^{2}H, and ^{31}P NMR spectra at room-temperature, 150°C, and 185°C. A delay time of 100 seconds was utilized for ^{2}H NMR data collections at 25°C and 150°C. A 2 second delay time was used at 185°C.

The D(1) and D(2) deuterium sites were assigned based on the total fitted area obtained using Origin 7.0 peak fitting module (Figure 5-12). The relative population of the D1:D2a:D2b sites is 2:1:1, corresponding to the 4 deuterium sites per unit cell (Table 5-3). The D(1) deuterium site was assigned to the peak at 4.97 ppm while the D(2) site types were assigned to peaks at 2.54 and 7.15 ppm. The peak fitting was not limited to a simple three-peak model but included seven peaks to fit the room temperature data, due to the complexity of the spectrum.

The quadrupolar coupling constant of the room-temperature and 150°C spectrum was estimated at 90 kHz. At 185°C, the powder pattern collapses to a single sharp peak, however this temperature is below the phase transition, and by X-ray diffraction techniques the crystal is still in the room-temperature structure. The collapse of the powder pattern indicates that the mobility of the deuterium in this structure at this temperature is higher than in the room-temperature structure.

Utilizing Abragam's discussion of destruction of fine structures through motion, an equation was developed (see Appendix) to describe the lineshapes of three-site chemical exchange[9]. A crude iteration through meaningful parameters for jump frequency yielded an estimate on the jump frequency at room temperature and 150°C.

Three-site exchange between frequencies, w(D1), w(D2a), and w(D2b) was modeled assuming Markov process [9]. Since [D1] = [D2a]+[D2b], the probability for a transition from a D1 site into a D2b site or D2a site is ¼. The probability that a D2a or

D2b site will exchange into a D1 site is ½, and the probability that a D2a will exchange to a D2b site is ¼.

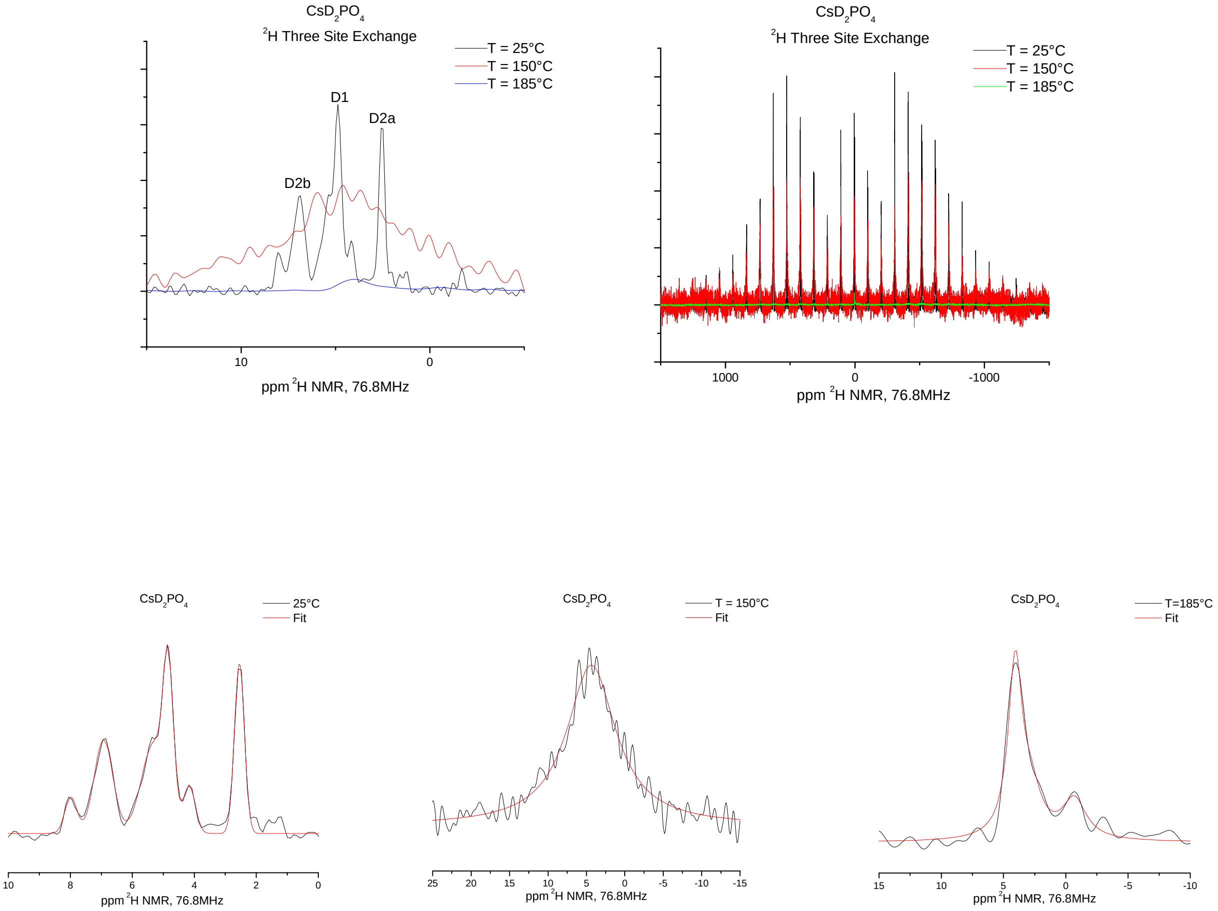

Figure 5-12. CsD_2PO_4 ^2H NMR spectra at 25°C, 150°C, and 185°C. The three ^2H sites present at room temperature coalesce at 150°C. The powder pattern collapses as the ^2H atoms become more mobile.

Temperature/°C	2H Site	Center of Mass/ppm	FWHM/ppm	%Fit Area
25	D1	4.97	1.08	51%
25	D2a	2.54	0.38	23%
25	D2b	7.15	0.72	26%
150	Davg	4.37	7.80	100%
185	Davg	3.75	2.25	100%

Table 5-3. CsD_2PO_4 ^2H NMR Peak Fitting Results for Spectra Collected at 25°C, 150°C, and 185°C. The three ^2H sites were assigned based on three deuterium sites. While the room temperature spectra appears to have more than three sites, this model was chosen based on site assignment in the literature and a simplification to make this model tractable.

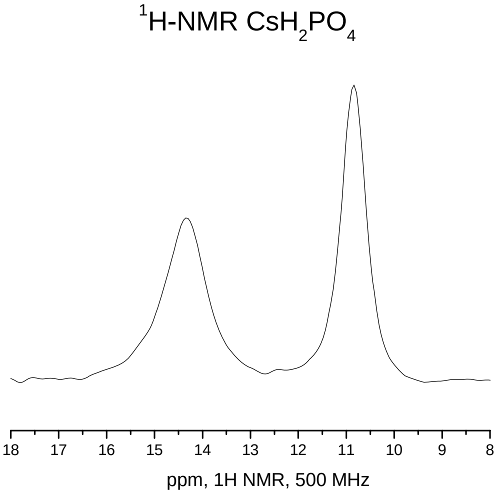

Figure 5-13. CsH_2PO_4 ^{1}H NMR MAS spectrum at room temperature. Unlike ^{2}H NMR spectra, ^{1}H NMR indicates only two proton sites.

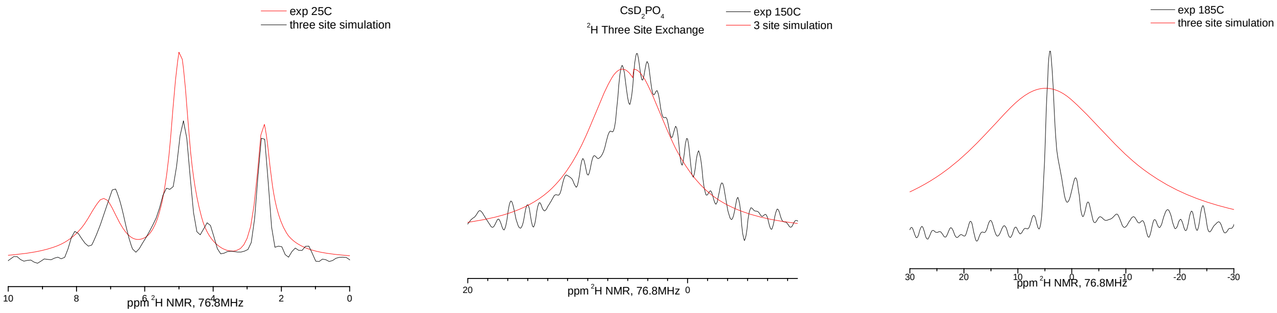

Figure 5-14. CsD_2PO_4 ^{2}H NMR MAS spectra at 25°C, 150°C and 185°C fit using a three-site chemical exchange model developed from Abragam's discussion. Jump frequencies determined from this analysis suggest deuterium exchange is an order of magnitude higher at 150°C than at 25°C. The model breaks down at 185°C, where the sharp peak is impossible to replicate assuming three-site exchange. Changes in the crystal structure or dynamics prior to the superprotonic phase change have altered the three deuterium sites to become more similar.

Temperature/°C	2H Site	Ω /ppm	Jump Frequency Ω /Hz
25	D1	0.5	38.4
25	D2a	0.5	38.4
25	D2b	0.5	38.4
150	Davg	12.5	960
185	Davg’	52.5	4032*

Table 5-4 CsD_2PO_4 ^2H NMR three-site exchange model jump frequency results at 25°C, 150°C, and 185°C.

The simulation approximated lineshapes for room-temperature and 150°C spectra, although improvements can be made on the fitting (Figure 5-14). The jump frequency estimated by this crude fit is 25 times higher than the room-temperature jump frequency (Table 5-4). The broadness of the experimental data is overestimated by the three-site chemical exchange fit, as undoubtedly the three sites have already become more similar due to thermal expansion of the crystal structure. Also, the fit predicts a center of mass for the peak that is at least 1 ppm higher than the actual data. This also suggests that the D2b site has become more similar to the other two sites.

The simulation results at 185°C shows that the sharp feature in the experimental data is not a result of three distinct chemical shifts coalescing. The spectrum at 185°C is a result of the high mobility of all three deuterium sites.

The collapse of the powder pattern (Figure 5-12) clearly shows that the deuterium sites are more mobile even at 185°C, which is well below the transition temperature of 230°C. The three-site chemical exchange model is feasible to 150°C but fails to describe the spectrum at 185°C. The chemical environment of the three distinct deuterium positions at that temperature must be more similar with respect to each other than in the room-temperature spectra, which may explain the sharp single peak, and this similarity may be caused by the higher mobility of each individual site. The jump frequencies obtained from this model illustrate that an order of magnitude increase in exchange frequency can be obtained below the structural phase transition. This three-site exchange method is useful for probing increased deuterium mobility in solid acid compounds prior to the phase transition.

Similar measurements at more temperatures would help explain the dependence of deuterium mobility on temperature and the effect of slight structural changes due to thermal expansion. A thorough analysis of lineshapes, chemical shifts and peak broadening, along with better three-site chemical exchange fitting at several temperatures, will help explain deuterium dynamics prior to the superprotonic phase transition in CsD_2PO_4.

Work on considering the chemical shift anisotropy of ^{31}P NMR signals was fruitless, as it was seen that the phosphorous atom environment is not a good indicator of pretransition effects (Figures 5-15, 5-16). ^{31}P NMR chemical shift anisotropy indicates the symmetry of the phosphorous atomic site. Variable-temperature experiments probing phosphorous signals resulted in an absolute shift of the NMR resonance position, but had little effect on the chemical shift anisotropy (Figure 5-16).

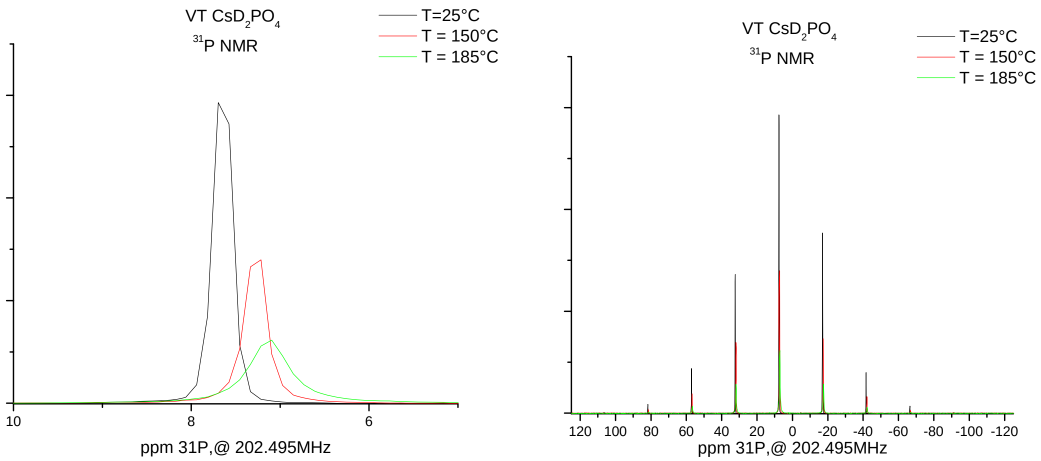

Figure 5-15. CsD_2PO_4 ^{31}P NMR MAS spectra at 25°C, 150°C, and 185°C. The CSA remains unchanged in this temperature regime.

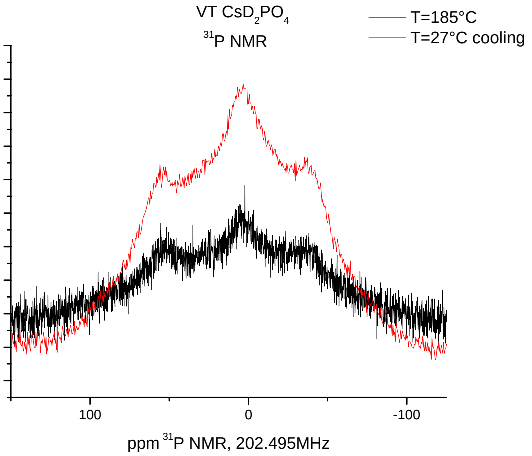

Figure 5-16. CsD_2PO_4 ^{31}P NMR static spectra at 185°C and 27°C after cooling. The chemical shift anisotropy remains unchanged in this temperature regime.

5.7 Conclusions

While some may still debate the high-temperature properties of CsD_2PO_4, high-resolution neutron powder diffraction data has been refined in a $Pm\bar{3}m$ structure assigning deuterium positions and oxygen positions. Pair distribution function data indicates that the number of configurations the phosphate tetrahedra samples is not strictly delimited by the Bragg diffraction average structure. A loss of long-range correlations for any atom pair distance outside the average bond distances of a phosphate tetrahedron and associated hydrogen bond shows that despite a clearly discernable average structure, the phosphate tetrahedron can be displaced from crystallographic positions. Configurational entropy calculations confirm measured entropy values provided unconventional phosphate orientations are allowed.

Pretransitional effects in CsD_2PO_4 show an increase in mobility of the deuterium positions 50°C before the actual superprotonic transition. Curiously, this disorder is not reflected in the chemical shift anisotropy of the phosphorous atom.

5.8 References

1. Larson, A.C. and R.B. Von Dreele. "General Structure Analysis System (GSAS)", Los Alamos National Laboratory Report LAUR 86-748 (2000), 2001.

2. Toby, B.H. EXPGUI, a Graphical User Interface for GSAS. Journal of Applied Crystallography, 2001, **34**: 210 – 213.

3. Preisinger, A.M. and K. W. Bronowska, The Phase Transition of CsH_2PO_4 (CDP) at 505K. Materials Science Forum, 1994, **166**: 511 – 516.

4. Yamada, K., et al. Superprotonic Conductor CsH_2PO_4 Studied by H-1, P-31 NMR and X-Ray Diffraction. Solid State Ionics, 2004. **175**(1-4): 557 – 562.

5. Haile, S.M., et al. Solid Acid Proton Conductors: From Laboratory Curiosities to Fuel Cell Electrolytes. Faraday Discussions, 2007, **134**: 17-39.

6. Boysen, D.A. et al. High-Temperature Behavior of CsH_2PO_4 Under Both Ambient and High Pressure Conditions. Chemistry of Materials, 2003, **15**(3): 727 – 736.

7. Blinc, R. et al. Pseudo-One-Dimensional Ferroelectric Ordering and Critical Properties of CsH_2PO_4 and CsD_2PO_4. Physical Review Letters, 1979, **43**(3): 231 – 234.

8. Topic, B., et al. Deuteron Magnetic-Resonance and Relaxation Study of the Pseudo-One-Dimensional Ferroelectric Transitions in CsD_2PO_4. Physical Review B, 1980, **21**(7): 2695 – 2701.

9. Abragam. Principles of Nuclear Magnetism. Oxford: 1961.

Chapter 6 Cation Size Effect in the $Cs_xRb_{1-x}H_2PO_4$ Solid Solution Series

The goal of this chapter is to identify crystal-chemical features that control superprotonic phase transitions in solid acid compounds. The cation size effect on the magnitude and temperature of the superprotonic phase transition in the $Cs_xRb_{1-x}H_2PO_4$ solid solution series is addressed.

6.1 Introduction

Superprotonic phase transitions, polymorphic transformations at which protonic conductivity increases by several orders of magnitude, appear to be facilitated by large cations, such as Cs and Rb. In particular, CsH_2PO_4, (CDP), exhibits superprotonic conductivity with a transition temperature of 230ºC while RbH_2PO_4,(RDP) exhibits a similar behavior only under pressure [1, 2]. Furthermore, the compounds crystallize in different structures at room temperature, CsH_2PO_4 – monoclinic $P2_1/m$ and RbH_2PO_4 – tetragonal $I\bar{4}_2d$ [3, 4]. The high-temperature structure of the Cs compounds is known to crystallize in the cubic $Pm\bar{3}m$ space group while that of RbH_2PO_4 is unknown. A study of the intermediate system, $Cs_{1-x}Rb_xH_2PO_4$, has been undertaken with the aim of elucidating the precise connection between average cation size and superprotonic behavior.

6.2 Synthesis Procedure and Characterization Methods

Compounds in the $Cs_xRb_{1-x}H_2PO_4$ system were synthesized in increments of x = 0.1. Stoichiometric amounts of CsH_2PO_4 and RbH_2PO_4 were mixed in a thermal bomb with 1-2 mL H_2O to prevent dehydration, and held at 350°C for three hours to allow homogeneous melting. Unlike other solid acid samples which are synthesized by aqueous precipitation by the addition of methanol or acetone, chemical intermediates cannot reliably be produced by powder precipitation. The stoichiometery of an aqueous solution does not necessarily constrain the stoichiometery of powder precipitates which necessitates synthesis of these compounds in the melt where the stoichiometery of the starting material does constrain the stoichiometery after processing. Samples were analyzed via powder X-ray diffraction, differential scanning calorimetry (DSC), AC impedance spectroscopy (ACIS), ^{1}H, ^{87}Rb, ^{133}Cs NMR MAS, Raman and Attenuated Total Reflectance Fourier Transform Infrared Spectroscopy (ATR/FTIR).

6.3 Phase Analysis

Powder samples were phase identified via X-ray diffraction (XRD) analysis at room-temperature on a Phillips diffractometer (X'Pert Pro) using Cu K Kα radiation. Intensities were obtained in the 2θ range between 10 and 90° with a step size of 0.02° and a measuring time of 10.8s at each step (scan speed 0.05 °/s, utilizing a small area detector). Philips X'Pert Plus software was utilized to perform Reitveld refinements to identify chemical intermediate phases and quantify cell parameters [5, 6].

The $Cs_xRb_{1-x}H_2PO_4$ system crystallized into the $P2_1/m$ structure with the exception of $Cs_{0.1}Rb_{0.9}H_2PO_4$ and RbH_2PO_4 (Figure 6-1). A gradual decrease in the cell volume is seen with increasing rubidium content, due to the smaller ionic radius of rubidium in octahedral coordination, 1.61Å, compared to that of cesium, 1.74 Å [7]. The phases synthesized in the $P2_1/m$ phase have an effective cation size range of 1.74 Å for the cesium end member to 1.64Å in the $Cs_{0.2}Rb_{0.8}H_2PO_4$ compound. This results in a reduction of 5.7% of the effective cation size while still preserving the $P2_1/m$ structure.

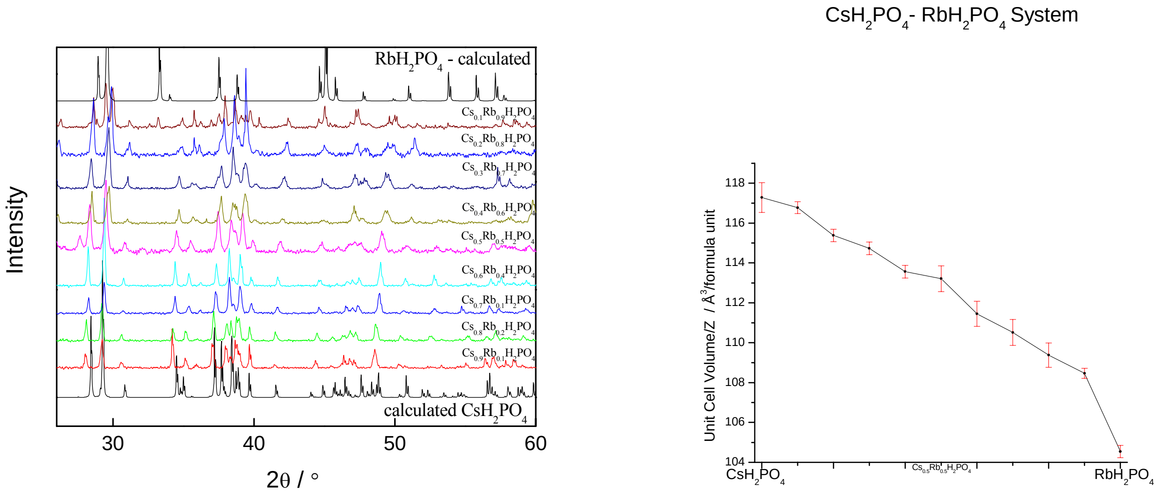

	a, Å	b, Å	c, Å	γ, °	O – O straight	O – O zigzag	O – O Tetra.
CsH_2PO_4	7.90065(8)	6.36890(9)	4.8725(1)	107.74(2)	2.5616	2.427, 2.4171	2.5344, 2.5170, 2.5143
$Cs_{0.9}Rb_{0.1}H_2PO_4$	7.889(1)	6.379(2)	4.873(1)	107.74(1)	2.5619	2.4247, 2.4169	2.5125, 2.5347, 2.5210
$Cs_{0.8}Rb_{0.2}H_2PO_4$	7.857(1)	6.347(1)	4.860(1)	107.79(1)	2.5547	2.4159, 2.4104	2.5245, 2.5083, 2.5019
$Cs_{0.7}Rb_{0.3}H_2PO_4$	7.838(1)	6.337(1)	4.855(1)	107.90(1)	2.5511	2.4121, 2.4085	2.5184, 2.4966, 2.5044
$Cs_{0.6}Rb_{0.4}H_2PO_4$	7.813(1)	6.312(1)	4.8435(9)	108.02(1)	2.5440	2.4060, 2.4035	2.4884, 2.5084, 2.4945
$Cs_{0.5}Rb_{0.5}H_2PO_4$	7.799(2)	6.308(2)	4.838(1)	107.97(2)	2.5416	2.4016, 2.4002	2.5065, 2.4846, 2.4929
$Cs_{0.4}Rb_{0.6}H_2PO_4$	7.766(2)	6.275(2)	4.819(2)	108.35(2)	2.5282	2.3955, 2.3937	2.4741, 2.4875, 2.4799,
$Cs_{0.3}Rb_{0.7}H_2PO_4$	7.747(2)	6.258(2)	4.805(1)	108.40(2)	2.5204	2.3899, 2.3873	2.4796, 2.4732, 2.4680
$Cs_{0.2}Rb_{0.8}H_2PO_4$	7.731(3)	6.230(2)	4.790(2)	108.51(2)	2.5114	2.3852, 2.3810	2.4616, 2.4693, 2.4621
$Cs_{0.1}Rb_{0.9}H_2PO_4$	7.706(2)	6.221(1)	4.783(1)	108.88(1)	2.5045	2.3827, 2.3799	2.4554, 2.4568, 2.4585
RbH_2PO_4	7.579(2)	7.579(2)	7.246(1)	90	2.4882		2.5056, 2.5351

Figure 6-1. (top left) X-Ray diffraction patterns of the $Cs_xRb_{1-x}H_2PO_4$ system. (top right) Unit cell volume per formula unit of the $Cs_xRb_{1-x}H_2PO_4$ system. (bottom) Cell parameters of compounds in the $Cs_xRb_{1-x}H_2PO_4$ system. All compositions adopt the CsH_2PO_4 structure except for $Cs_{0.1}Rb_{0.9}H_2PO_4$ and RbH_2PO_4.

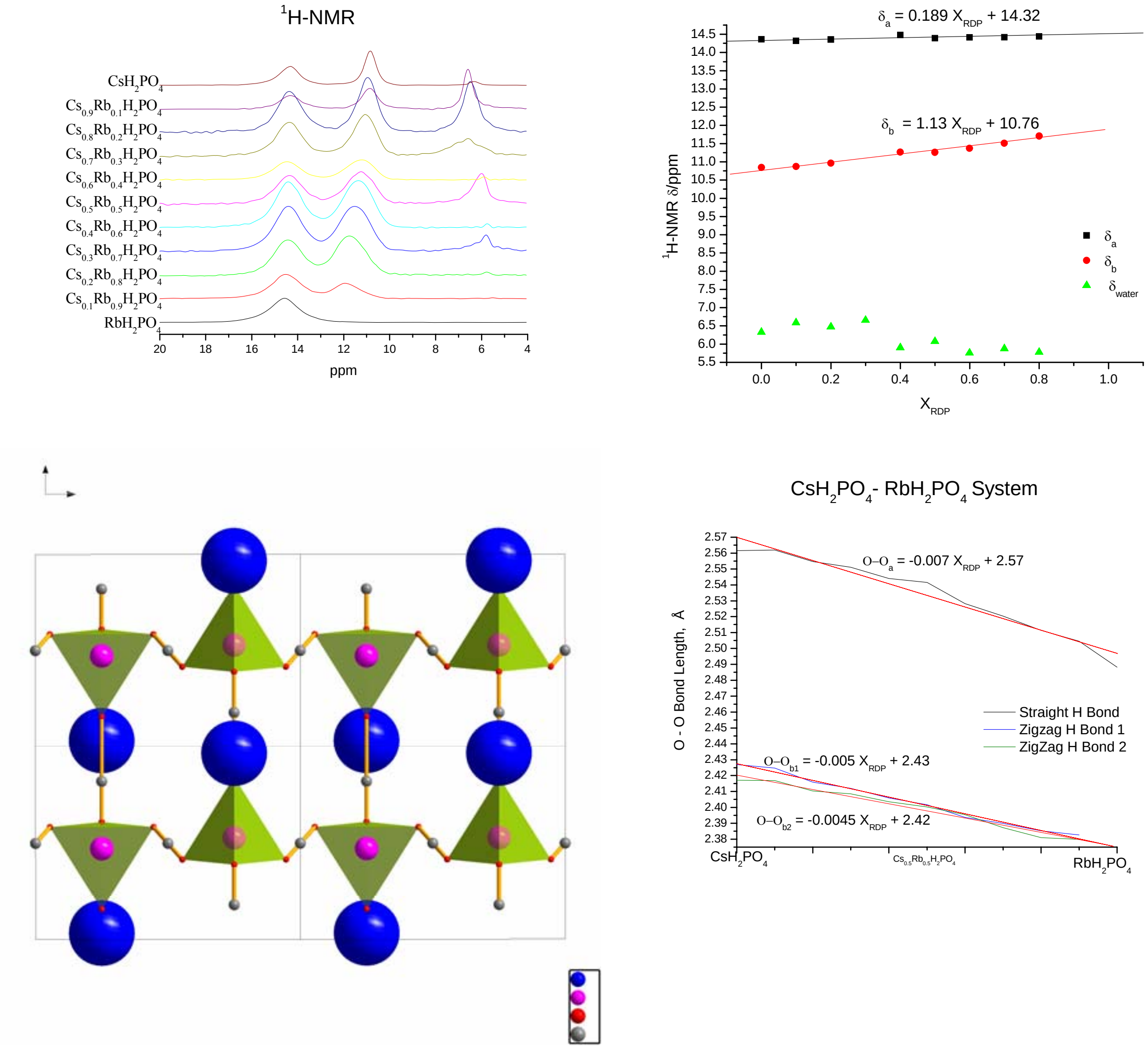

Figure 6-2. (top left) ^{1}H NMR MAS spectra of $Cs_xRb_{1-x}H_2PO_4$ system using TMS as a standard. Two proton resonances are evident at each Cs-containing composition: δ = ~14.4 ppm and δ = 11-12 ppm. Peaks at ~6 ppm are due to surface water. (top right) ^{1}H NMR MAS chemical shifts vs. mole fraction of Rb fitted with a linear trend. Both chemical shifts move towards higher acidity with increasing Rb content. Hydrogen resonance ~14.4 ppm is due to the hydrogen involved in the ordered hydrogen bonds that zigzag along the b-axis. Hydrogen resonance between 11-12 ppm is more sensitive to cation size and represents the disordered hydrogen bond position running parallel to the c-axis. (bottom left) CsH_2PO_4 room temperature structure viewed along the [100] direction. (bottom right) O – O bond length versus composition in the $Cs_xRb_{1-x}H_2PO_4$ system. Linear fits to bond distances reconfirm hydrogen atom assignment of ^{1}H NMR peaks. Disordered hydrogen bond lengths parallel to c-axis are more responsive to Rb incorporation.

^{1}H, ^{87}Rb, and ^{133}Cs NMR line shapes and peak positions for the $Cs_xRb_{1-x}H_2PO_4$ series vary gradually over the compositional range. ^{1}H NMR peaks with chemical shifts of 6 ppm are due to surface water (Figure 6-2). In the $P2_1/m$ CsH_2PO_4 structure, there are two crystallographic hydrogen resonances, $\delta \cong 14.4$ ppm and $\delta = 11 – 12$ ppm (Figure 6-2). The ^{1}H NMR peak at 14.4 ppm is due to the hydrogen involved in the ordered hydrogen bond that zigzags along the b-axis. The peak at 11 – 12 ppm is due to the disordered hydrogen site that participates in hydrogen bonds along the c-axis. This assignment is based on a comparison of the broadness of the ^{1}H NMR peaks, the sensitivity of one ^{1}H NMR peak to effective cation size and the room temperature crystal structure (Figure 6-2).

The ^{1}H NMR resonance at $\delta \cong 14.4$ ppm is broader than the resonance at 11 – 12 ppm. The broadness of the line shape is an indication of the average motion occurring at that proton site. As the $\delta \cong 14.4$ ppm peak is broader, it is expected to be in the ordered, less mobile position along the zigzag hydrogen bond b-axis. The narrower peak at 11 – 12 ppm resides in the disordered proton site that forms hydrogen bonds along the c-axis. In the crystal structure, layers of cations separate layers of phosphate tetrahedra which are hydrogen bonded along the b-axis (zigzag, ordered) and the c-axis (straight, disordered). The cation separation of the phosphate layers affects the hydrogen bonding of the disordered bonds that form along the c-axis almost exclusively. The zigzag hydrogen bonds (^{1}H NMR resonance at $\delta \cong 14.4$ ppm) are isolated between layers of cations and the spacing or size of the cations has a limited effect on their chemical shift and broadness.

The disordered hydrogen site (^{1}H NMR resonance at $\delta = 11 – 12$ ppm), however, is strongly affect by the effective cation size. In a linear fit of ^{1}H NMR chemical shifts versus rubidium content, the chemical shift of the disordered site, $\delta_b = 1.13X_{RDP} + 10.76$, is approximately 6 times more responsive to rubidium content compared to the ordered proton site, $\delta_a = 0.189X_{RDP} + 14.32$ (Figure 6-2). A reduction in the cation size not only broadens the disordered ^{1}H NMR line shape but also moves the resonance to lower chemical shifts. The line shape broadening indicates a loss of mobility in the disordered site which might imply that the spatial difference between the disordered sites is decreasing as the cation layers are shrinking with higher rubidium content. A linear fit of the disordered hydrogen bond length indicates that bond length is more responsive to rubidium incorporation compared to the ordered, zigzag hydrogen bond which confirms the assignment of the ^{1}H NMR peaks (Figure 6-2 (bottom right)).

^{87}Rb, and ^{133}Cs NMR line shapes and peak positions for the $Cs_xRb_{1-x}H_2PO_4$ series vary gradually over the compositional range (Figure 6-3). The ^{87}Rb MAS NMR peak profile for all intermediate rubidium-containing compounds exhibits one rubidium peak position. The RbH_2PO_4 compound ^{87}Rb MAS NMR peak profile shows quadrupolar splitting of a single crystallographic rubidium site in the $I\bar{4}_2d$ space group. The full width at half maximum (FWHM) of the ^{87}Rb NMR peaks is relatively constant over the compositional range.

^{133}Cs NMR peak positions shift to higher ppm and broaden dramatically with increasing rubidium content. Peak profiles for $Cs_{0.7}H_{0.3}PO_4$, and $Cs_{0.1}Rb_{0.9}H_2PO_4$ exhibit significant peak shoulders suggesting the environment of the cesium atom is perturbed by the addition of rubidium into the structure. The presence of the peak shoulder on only a couple of the ^{133}Cs NMR peak profiles is difficult to interpret; however, one interpretation is that these samples are not perfectly homogenous.

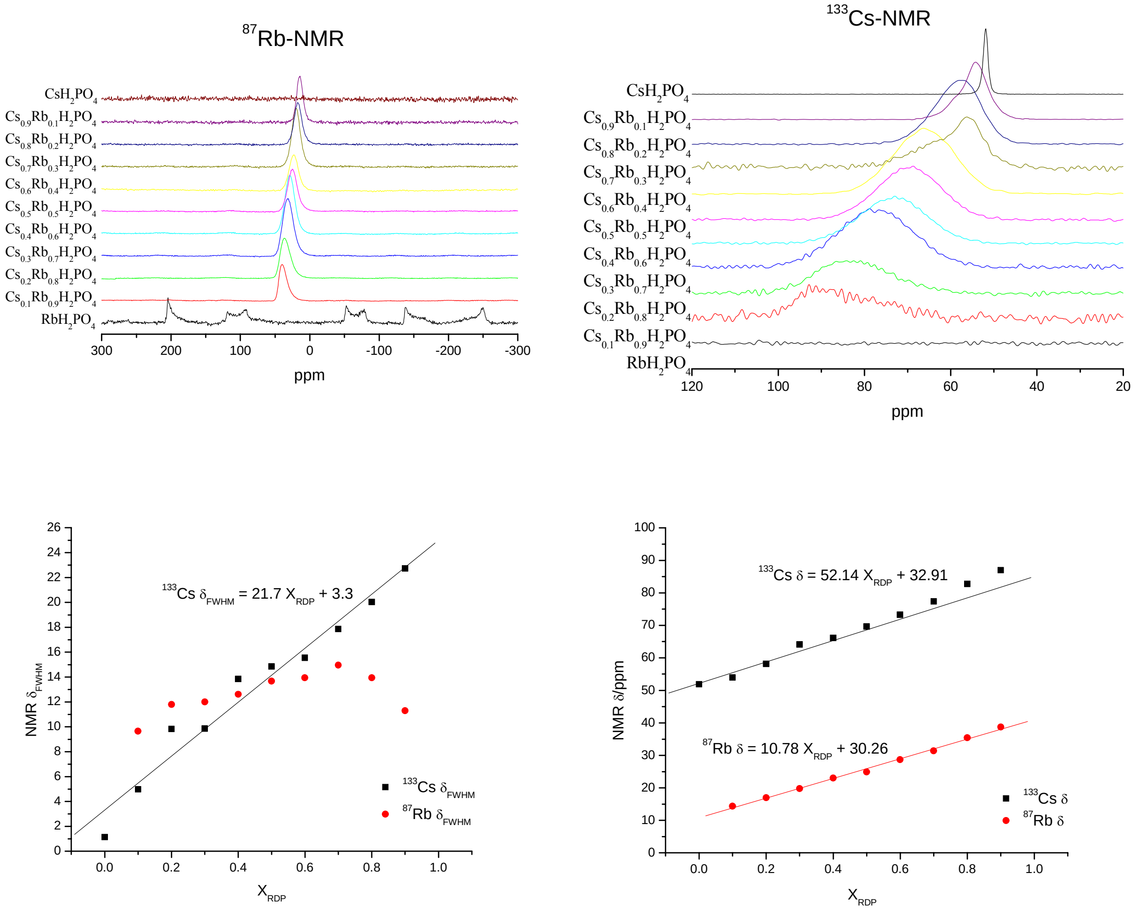

Figure 6-3. (top left) ^{87}Rb NMR MAS spectra of $Cs_xRb_{1-x}H_2PO_4$ system using aqueous $RbNO_3$ as a standard. Peaks shift monotonically downfield (higher ppm) with increasing Rb content. RbH_2PO_4 spectrum suffers from quadrupolar interactions of a single Rb resonance. (top right) ^{133}Cs NMR MAS spectra of $Cs_xRb_{1-x}H_2PO_4$ system using 0.5M CsCl aqueous solution as a standard. Anisotropic broadening is visible with increasing amounts of Rb in the structure suggesting reduced Cs mobility with Rb incorporation. (bottom left) MAS NMR studies reveal a linear dependence of ^{133}Cs δ_{FWHM} on Rb content in the Cs-containing composition range. FWHM is a measure of the anisotropic broadening resulting from reduced Cs mobility. (bottom right) ^{87}Rb and ^{133}Cs NMR MAS chemical shifts vs. mole fraction of Rb fitted with linear trends.

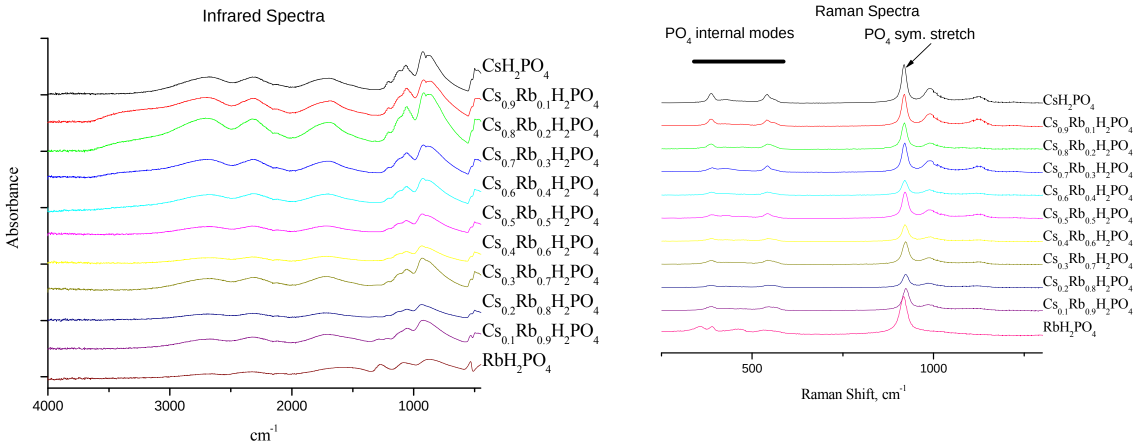

Figure 6-4. (left) Attenuated Total Reflectance FT Infrared data for the $Cs_xRb_{1-x}H_2PO_4$ system indicates insensitivity to Rb incorporation. The broad bands between 2000 to 3000 cm^{-1} suggest that hydrogen bonding is equally strong throughout the entire system. (right) Raman shift data for the $Cs_xRb_{1-x}H_2PO_4$ system. The PO_4 symmetric stretch at 900 cm^{-1} is constant throughout composition range.

Infrared and Raman spectroscopy on powder samples support X-ray diffraction evidence of a single structure for the CsH_2PO_4 – $Cs_{0.2}Rb_{0.8}H_2PO_4$ series (Figure 6-4). Peaks present in the CsH_2PO_4 compound are evident throughout the series except for the RbH_2PO_4 end member. Bands at 920 cm^{-1} in the Raman spectra indicate a symmetric stretch of the PO_4 tetrahedra. Infrared spectra contain very broad bands between 2000 to 3000 cm^{-1} that decrease in intensity with rubidium incorporation. These features suggest that the strength of the hydrogen bonds is not consistent throughout the entire system.

6.4 Thermal Analysis

Differential scanning calorimetry profiles for the $Cs_xRb_{1-x}H_2PO_4$ system were collected at a scan rate of 10K/min in closed-volume containers to minimize dehydration (Figure 6-5). Endothermic peaks which occur at lower temperatures and lower Rb content correspond to the superprotonic transition. Peaks at higher temperatures indicate melting. With increasing Rb content, the temperature gap between melting and the superprotonic transition decreases. The DSC profile for the RbH_2PO_4 end member shows that the superprotonic phase transition and melting transition have coalesced into a single peak. The superprotonic transition temperature remains relatively constant in cesium-rich chemical intermediates, $Cs_xRb_{1-x}H_2PO_4$, $x > 0.5$. For $x < 0.5$, the superprotonic transition temperature increases monotonically.

In this set of experiments, the entropy of the phase transition for CsH_2PO_4 and chemical intermediates, $Cs_xRb_{1-x}H_2PO_4$, $x > 0.2$, averages to 18.22 J/molK. Earlier discussions in this work on the entropy of the superprotonic phase transition for CsH_2PO_4 estimate a value of 21.5 J/molK which agrees well with the experimentally determined values for chemical compounds $Cs_xRb_{1-x}H_2PO_4$, $x > 0.2$. For the rubidium-rich compounds, $Cs_{0.2}Rb_{0.8}H_2PO_4$ and $Cs_{0.1}Rb_{0.9}H_2PO_4$, the DSC peak at lower temperatures overlaps with the melting transition. Peak fitting assigns much lower values to the enthalpy of the lower temperature phase transition which results in entropy values of 6.71 and 5.14 J/molK. The discrepancy in entropy values across compositions suggests that while the room temperature structure of $Cs_{0.2}Rb_{0.8}H_2PO_4$ is homologous to CsH_2PO_4, the high temperature structure of $Cs_{0.2}Rb_{0.8}H_2PO_4$ differs from the $Pm\bar{3}m$ structure of CsH_2PO_4.

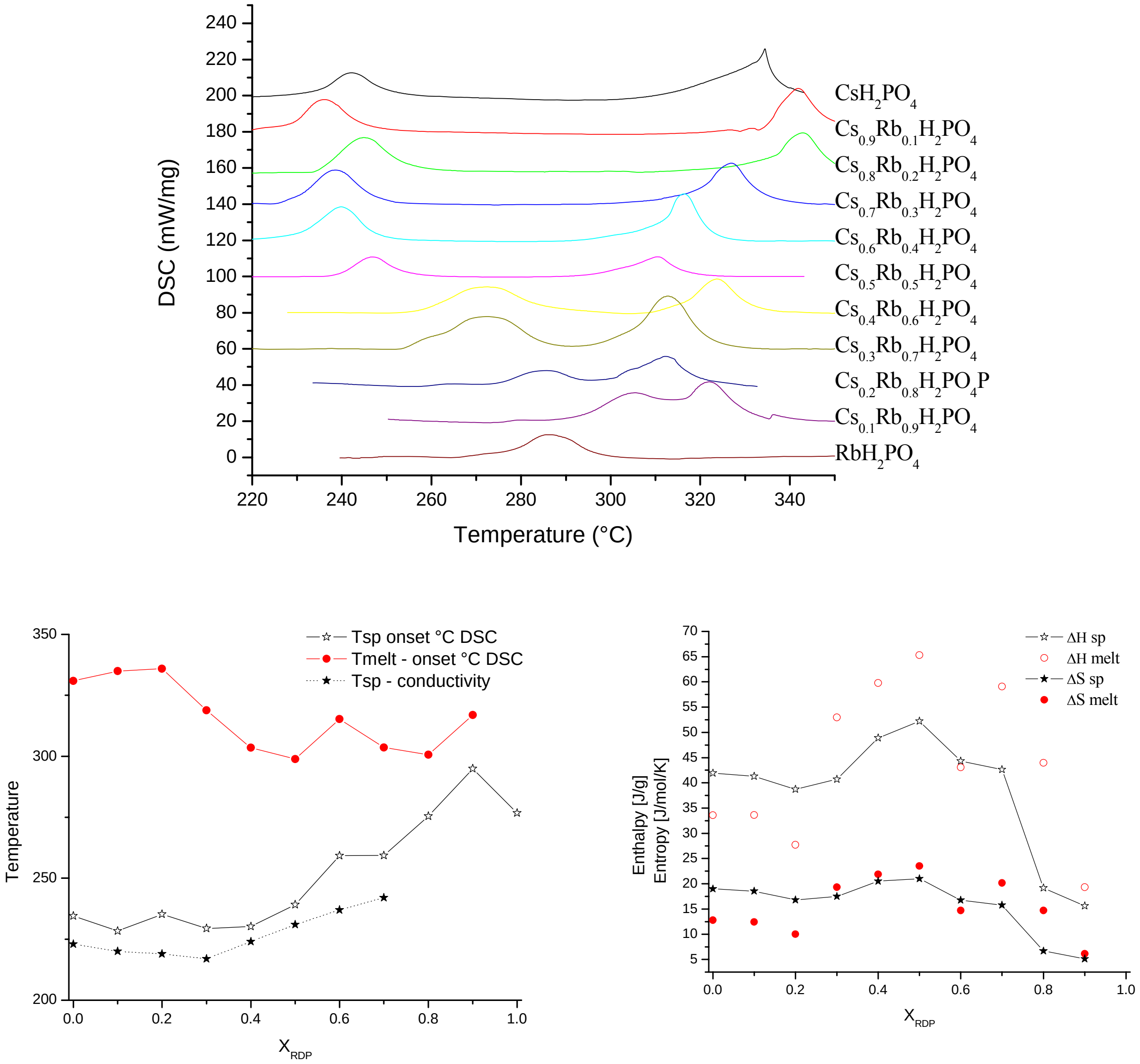

Figure 6-5. (top) Differential Scanning Calorimetry (DSC) for the $Cs_xRb_{1-x}H_2PO_4$ system obtained from samples placed in closed volume containers to minimize thermal dehydration. Endothermic peaks at lower temperatures and lower Rb content correspond to the superprotonic transition. Peaks at higher temperatures indicate melting. With increasing Rb content, the temperature gap between melting and the superprotonic transition decreases. The superprotonic phase transition and melting transition are combined at this heating rate for the RDP end member. (bottom left) Superprotonic transition and melt temperature as a function of Rb content. DSC and ACIS findings concur for x > 0.5, $Cs_xRb_{1-x}H_2PO_4$, the superprotonic transition temperature remains constant. For x < 0.5, superprotonic transition temperature increases monotonically. (bottom right) Entropies and enthalpies of superprotonic and melting transitions. The entropy of the superprotonic phase transition is constant in the system except for $Cs_{0.2}Rb_{0.8}H_2PO_4$ and $Cs_{0.1}Rb_{0.9}H_2PO_4$. All other compositions undergo a similar superprotonic phase transition.

Composition	T_{sp} [°C]	ΔS_{sp} [J/molK]	Tmelt [°C]	ΔSmelt [J/molK]
CsH_2PO_4	234.6	18.98	330.9	12.8
$Cs_{0.9}Rb_{0.1}H_2PO_4$	228.4	18.54	335.0	12.4
$Cs_{0.8}Rb_{0.2}H_2PO_4$	235.2	16.78	335.9	10.0
$Cs_{0.7}Rb_{0.3}H_2PO_4$	229.4	17.48	318.9	19.3
$Cs_{0.6}Rb_{0.4}H_2PO_4$	230.2	20.50	303.5	21.9
$Cs_{0.5}Rb_{0.5}H_2PO_4$	239.2	21.01	298.8	23.5
$Cs_{0.4}Rb_{0.6}H_2PO_4$	259.3	16.74	315.3	14.7
$Cs_{0.3}Rb_{0.7}H_2PO_4$	259.4	15.76	303.6	20.2
$Cs_{0.2}Rb_{0.8}H_2PO_4$	275.4	6.71	300.7	14.7
$Cs_{0.1}Rb_{0.9}H_2PO_4$	294.9	5.14	316.9	6.1
RbH_2PO_4	276.7			

Table 6-1. Temperatures and enthalpies of superprotonic transitions in the $Cs_xRb_{1-x}H_2PO_4$ system

6.5 Conductivity

The conductivity of pressed pellet samples (P = 4 tons, diameter = 10mm, 5 minutes pressing time) were measured under flowing humidified nitrogen. Silver electrodes were painted onto the surfaces of pellet samples from the entire $Cs_xRb_{1-x}H_2PO_4$ system. A.C. impedance data were collected over the frequency range of 20Hz-1MHz using an HP 4284 precision LCR meter at an applied voltage of 200 mV. Zview (Scribner Associates Inc.), a least squares refinement program, was utilized to fit the acquired impedance data to several different equivalent circuits including (RQ), (R1Q1)(R2Q2), (R1)(R2Q2), etc, where R is resistance and Q is constant phase element with impedance $Z_Q = (Y(j\omega)^n)^{-1}$; where $j = \sqrt{-1}$, ω = frequency, Y and n are constants, and n ranges between 0 and 1 [8].

The superprotonic transition was evident in the compositional range of CsH_2PO_4 – $Cs_{0.3}Rb_{0.7}H_2PO_4$ but was extinguished in the $Cs_{0.2}Rb_{0.8}H_2PO_4$ compound (Figure 6-6).

From this result, the effective cation radius which enables a superprotonic transition in the $Cs_xRb_{1-x}H_2PO_4$ system, $R_{sp} \geq 1.649$Å, is a weighted average of the ionic radii based on the composition of the $Cs_{0.3}Rb_{0.7}H_2PO_4$ compound(r(Cs^{VIII}) = 1.74 Å; r(Rb^{VIII}) = 1.61 Å)[7]. This value is an 5.2% decrease compared to the cesium end member cation radius, CsH_2PO_4. The entropy value for $Cs_{0.2}Rb_{0.8}H_2PO_4$ (6.71 J/molK) is much lower than that of chemical intermediates with higher cesium content (18.22J/molK), and so the lack of a superprotonic phase transition for this compound is not surprising. The overall magnitude of the superprotonic phase transition across the compositional range of chemical intermediates exhibiting this transition was relatively constant.

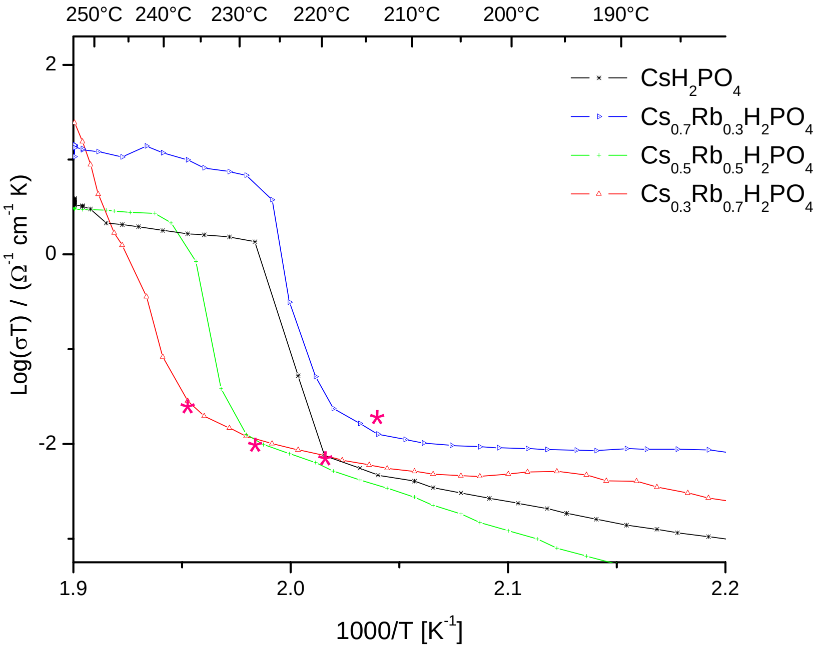

Figure 6-6. Conductivity as a function of temperature plotted in Arrhenius form for selected compositions in the $Cs_xRb_{1-x}H_2PO_4$ system. Each heating cycle is marked with an asterisk indicating the onset of the superprotonic transition. The superprotonic transition temperature increases with Rb content for chemical intermediates, $Cs_xRb_{1-x}H_2PO_4$, x > 0.5.

6.6 Conclusions

The chemical intermediates $Cs_xRb_{1-x}H_2PO_4$ crystallize in the CsH_2PO_4 structure, P2/m, for the compositions CsH_2PO_4 through $Cs_{0.2}Rb_{0.8}H_2PO_4$. Impedance measurements carried out under appropriate water partial pressures (0.3 – 0.7 atm) verifies the transition temperature trend measured by differential scanning calorimetery in closed-volume containers and the presence of a superprotonic transition over CsH_2PO_4 – $Cs_{0.3}Rb_{0.7}H_2PO_4$. Entropy values estimated from DSC scans confirm transitions in $Cs_{0.2}Rb_{0.8}H_2PO_4$ and $Cs_{0.1}Rb_{0.9}H_2PO_4$ have much lower entropy values and these transitions cannot represent the $P2_1/m \longrightarrow Pm\overline{3}m$ transition illustrated by the rest of the series.

For compounds in the series that do exhibit the superprotonic phase, the magnitude of proton conductivity in that phase remains neutral to rubidium incorporation. Altering the effective cation size shows, for this series, a profound impact on transition temperature for compounds with high rubidium content ($x < 0.5$) while preserving the overall conductivity of the high-temperature and low-temperature phases.

X-ray diffraction, thermal analysis, Raman, IR, ^{133}Cs, ^{87}Rb and ^{1}H-NMR spectroscopy all attest to the gradual variation in structural properties across the composition range. The limiting effective cation radius for a superprotonic transition for this series has been determined to be $R_{sp} \geq 1.649$ Å.

6.7 References

1. Boysen, D.A. et al. High-Temperature Behavior of CsH_2PO_4 Under Both Ambient and High Pressure Conditions. Chemistry of Materials, 2003, **15**(3): 727 – 736.

2. Boysen, D.A. et al. Conductivity of Potassium and Rubidium Dihydrogen Phosphates at High Temperature and Pressure. Chemistry of Materials, 2004. **16**(4): 693 – 697.

3. Mattauch, S., G. Heger, and K.H. Michel. High Resolution Neutron and X-Ray Diffraction Studies as a Function of Temperature and Electric Field of the Ferroelectric Phase Transition of RDP. Crystal Research and Technology, 2004, **39**(12): 1027.

4. Preisinger, A.M., K.;Bronowska, W. The Phase Transition of CsH_2PO_4 (CDP) at 505K. Materials Science Forum, 1994, **166**: 511 – 516.

5. Zetterstrom, P., et al. Structure and Proton Conduction in $CsDSO_4$. Solid State Ionics, 1999, **116**(3 – 4): 321 – 329.

6. X'Pert HighScore. 2002, Philips Analytical B.V.: Almelo.

7. Shannon, R.D. and C.T. Prewitt. Revised Values of Effective Ionic Radii. Acta Crystallographica Section B-Structural Crystallography and Crystal Chemistry, 1970, **B 26**: 1046.

8. Johnson, D. ZView. 2000, Scribner Associates, Inc.

Chapter 7 High-Temperature Properties of $Rb_3H(SO_4)_2$ snd Implications for $M_3H(XO_4)_2$ Phase Transitions

Misleading data from a compound in the $M_3H(XO_4)_2$ family, $Rb_3H(SO_4)_2$, has been interpreted in the literature as a superprotonic transition. In this chapter, evidence presented supports the claim that, at high-temperatures (T ~ 200°C),

$$Rb_3H(SO_4)_2\ (s) \leftrightarrow Rb_2SO_4\ (s) + RbHSO_4\ (l),$$

where phase separation from the solid phase into rubidium sulfate and rubidium hydrogen sulfate mimics a superprotonic phase, due to the high proton mobility in the rubidium hydrogen sulfate melt. Contrary to published work, $Rb_3H(SO_4)_2$ does not undergo a superprotonic phase transition under ambient pressure conditions. While investigating the above transition, the incongruent melt of

$$RbHSO_4\ (s) \leftrightarrow Rb_2SO_4\ (s) + H_2SO_4\ (l)$$

was also identified.

7.1 Introduction

Compounds in the $M_3H(XO_4)_2$, (where M = NH_4, K, Rb, Cs and X = S, Se) family exist in the A2/a or C2/c structure and usually transform at higher temperatures into the $R\overline{3}m$ structure (Table 7-1). While some compounds in the $M_3H(XO_4)_2$ family are stable at higher temperature and exhibit superprotonic phase transitions, $Rb_3H(SO_4)_2$, under atmospheric pressure, phase separates into $RbHSO_4$ and Rb_2SO_4. Unfortunately, this phase separation has been misinterpreted as a superprotonic phase transition due to the liquid-like nature of the superprotonic phase. All data collected on $Rb_3H(SO_4)_2$ are misleading. This work presents X-ray diffraction, calorimetry, thermo-mechanical, and impedance spectroscopy data illustrating this phase separation and its similarities to a solid→solid superprotonic phase transition.

7.2 Synthesis Procedure

Crystalline powders of $Rb_3H(SO_4)_2$ were synthesized by dissolving Rb_2SO_4 (Alfa Aesar 99% purity) into deionized (DI) water and adding H_2SO_4 in the molar ration of 3/4:1, respectively. Powder precipitate was formed by adding methanol. The resulting crystals were vacuum filtered and rinsed with additional methanol and dried for a short period of time at 80°C (2 – 3 hours). $RbHSO_4$ crystals were grown by slow evaporation of an aqueous solution of dissolved Rb_2SO_4 (Alfa Aesar 99% purity) and excess H_2SO_4 in the molar ration of 1/2:4/3, respectively. Large crystals resulted and were vacuum dried to get all excess mother liquor off the crystal faces, then rinsed quickly with DI water to remove excess acid, and subsequently with acetone and placed in an oven at 80°C for 12 hours to dry. The Rb_2SO_4 used in the calorimetry part of this work was Alfa Aesar #12872 Puratronic®, 99.975%(metals basis).

Powder samples of $Rb_3H(SO_4)_2$ and $RbHSO_4$ were phase identified via X-ray diffraction (XRD) analysis at room temperature on a Phillips diffractometer (X'Pert Pro) using Cu K Kα radiation. Intensities were obtained in the 2 θ range between 10° and 80° with a step size of 0.004° and a measuring time of 10.8 seconds at each step (scan speed 0.05 °/s, utilizing a small area detector).

Compound	V	$T_{V\leftrightarrow IV}$ [K]	IV	$T_{IV\leftrightarrow III}$ [K]	III	$T_{III\leftrightarrow II}$ [K]	II	$T_{II\leftrightarrow I}$ [K]	I
$K_3H(SO_4)_2$							A2/a		???
$Rb_3H(SO_4)_2$							C2/c	473	Phase separation
$(NH_4)_3H(SO_4)_2$							C2/c	433	$R\bar{3}m$
$Tl_3H(SO_4)_2$ [1, 2]		156		196		239		267	$R\bar{3}m$
$K_3H(SeO_4)_2$ [3, 4]					C2, Cc, P21/c	21(105-D)	C2/c	290	$R\bar{3}m$
$Rb_3H(SeO_4)_2$							A2/a	449	$R\bar{3}m$
$(NH_4)_3H(SeO_4)_2$ [5-8]	C1C1(9)	181	C2/c	276-279		302-305	$R\bar{3}$	332	$R\bar{3}m$
$Cs_3H(SeO_4)_2$			Probably triclinic	50	C2/m	369	A2/a	456	$R\bar{3}m$

Table 7-1. $M_3H(XO_4)_2$ Phase Transitions and Temperatures

7.3 High-Temperature X-Ray

High-temperature scans were achieved using an Anton Paar HTK 1200 oven over a temperature range from room temperature to 270°C. Intensities were obtained in the 2θ range between 10° and 90° with a step size of 0.02° and a measuring time of 30 seconds, scan speed 0.07°/s (for temperatures at which a clear phase was not expected); and alternatively in the 2 θ range between 10° and 90° with a step size of 0.02° and a measuring time of 90 seconds in the high-temperature regime to allow for better signal to noise ratio for refinement purposes (scan speed 0.02°/s). $Rb_3H(SO_4)_2$ was scanned at various temperatures (T=[25°C, 185°C, 200°C, 220°C, 230°C, 240°C, 250°C, 260°C, 270°C, 285°C, after cooling 25°C]), with and without a nickel standard, on loose powder and on a pressed pellet sample. Philips X'Pert Plus software was utilized to perform a Reitveld refinement of the high-temperature phase.

7.3.1 Powder Sample

X-ray powder diffraction scans, T = 205°C, on $Rb_3H(SO_4)_2$ immediately reveal a phase change from the room-temperature phase of $Rb_3H(SO_4)_2$, C2/c, to the orthorhombic Pnam structure of Rb_2SO_4 (Figure 7-1). The by-product of the starting compound, $Rb_3H(SO_4)_2$, phase separating into Rb_2SO_4 leaves a compound of stoichiometry $RbHSO_4$. Under atmospheric pressures, $RbHSO_4$ melts around 200°C [9] which is one possible explanation that no peaks due to $RbHSO_4$ can be detected at 205°C. The absence of amorphous broad features in the diffraction pattern is puzzling, as it is expected that half of the powder sample is molten at temperatures above 205°C. Powder samples from these high-temperature X-ray diffraction experiments are found to crystallize back into the C2/c structure of $Rb_3H(SO_4)_2$ after several days at room temperature.

X-ray diffraction patterns from $Rb_3H(SO_4)_2$ (T = 205°C) and Rb_2SO_4 (T = 220°C) powder samples were both refined into the standardized Webber, 1989, Pnam structure. Thermal expansion of the cell volume to 502.18 Å^3 at 220°C for Rb_2SO_4 agrees well with refined volume (V = 500.697 Å^3) from the $Rb_3H(SO_4)_2$ compound at 205°C (Appendix Tables A-1 and A-2).

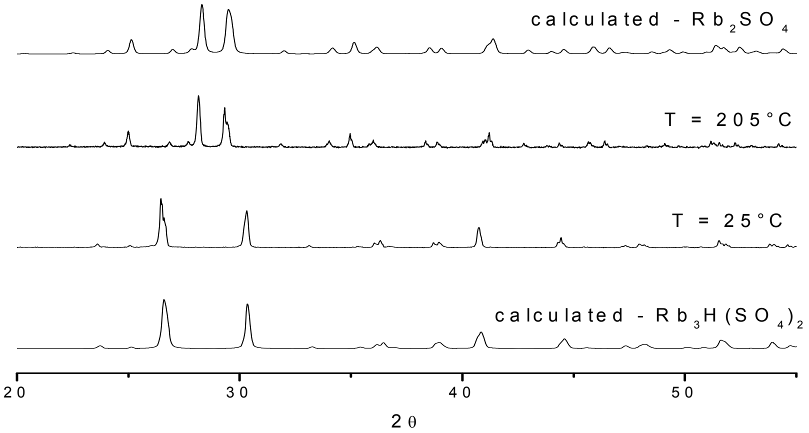

Figure 7-1. X-ray powder diffraction patterns of $Rb_3H(SO_4)_2$ on loose powder sample. The sample was heated to 225°C at a rate of 5K/min and scanned immediately. Scan time at 225°C is six minutes. For temperatures above 205°C, powder diffraction patterns from samples of $Rb_3H(SO_4)_2$ resemble that of Rb_2SO_4.

7.3.2 Pellet and Single Crystal Samples

High-temperature powder X-ray diffraction experiments on pressed powder samples illustrate slightly different behavior from that of powder samples. Despite long equilibration times (~ 4 hours), pellet samples of $Rb_3H(SO_4)_2$ retained diffraction peaks of the original structure at T = 205°C (Figure 7-2). Additional peaks at this temperature are due to the Rb_2SO_4 phase. The persistence of the $Rb_3H(SO_4)_2$ phase in the pressed powder pellet sample, along with the appearance of some diffraction peaks attributed to Rb_2SO_4, can incorrectly be interpreted as a new phase for $Rb_3H(SO_4)_2$.

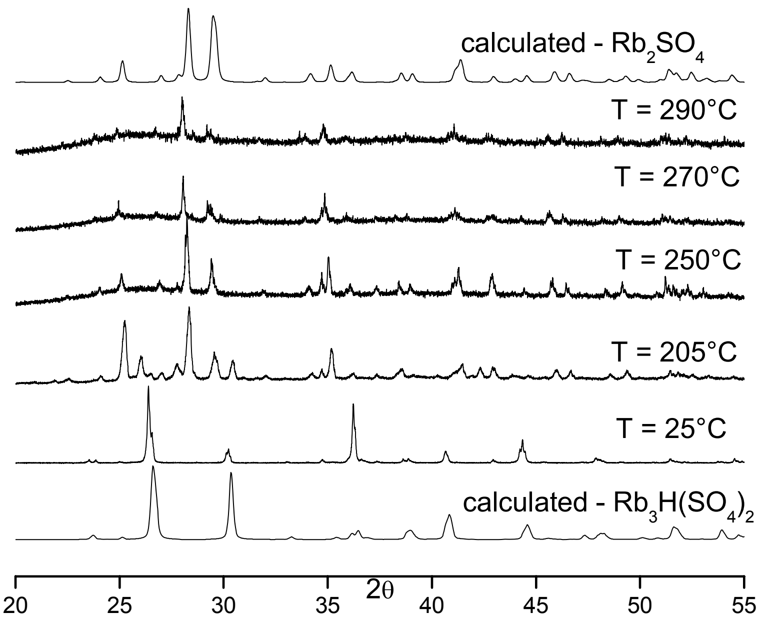

Figure 7-2. X-ray powder diffraction patterns of $Rb_3H(SO_4)_2$ on pressed pellet sample. Phase separation indicated at 205°C shows both $Rb_3H(SO_4)_2$ and Rb_2SO_4 peaks. Sample was allowed to equilibrate at 205°C for approximately 4 hours.

Further confusion in investigating $Rb_3H(SO_4)_2$ results from single crystal samples showing a deceptively simple X-ray diffraction pattern at elevated temperatures (Figure 7-3). This pattern could easily be perceived as a pure, high-symmetry phase. Diffraction patterns of pellet samples of $Rb_3H(SO_4)_2$ and other stoichiometries of pressed powder samples also show this pattern under high pressure and fine-grain-size pellet pressing conditions (Figure 7-4). This misleading pattern is oriented Rb_2SO_4, resulting from phase separation in single crystal $Rb_3H(SO_4)_2$ and pressed powder samples. For comparison, a Rb_2SO_4 pellet sample, pressed at high pressures, P ~ 19 tons, 10 mm diameter, for approximately 6 hours presents a nearly identical X-ray diffraction pattern (Figure 7-3).

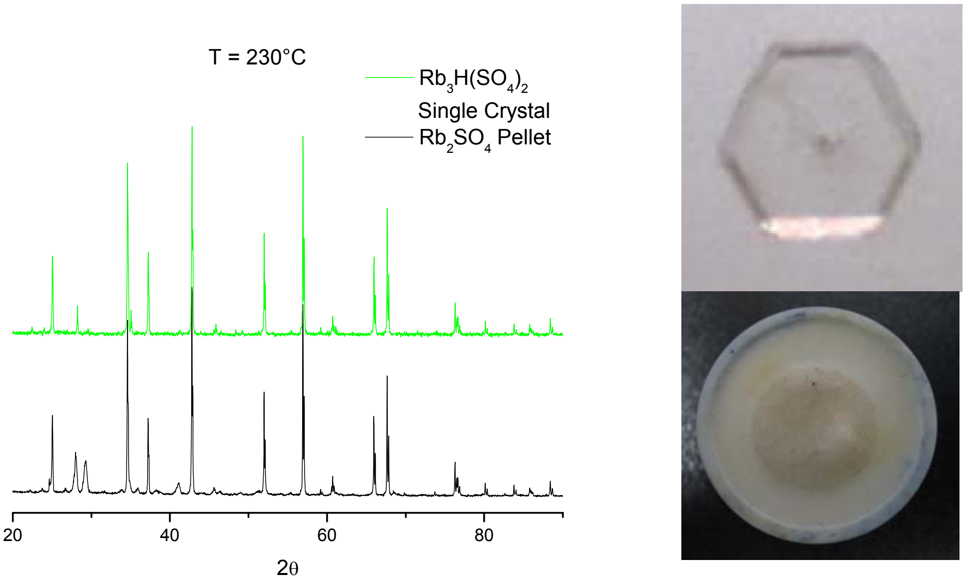

Figure 7-3. X-ray powder diffraction pattern of a single crystal of $Rb_3H(SO_4)_2$ and a pressed powder sample of Rb_2SO_4 show identical structure at 230°C indicating phase separation in the single crystal retains Rb_2SO_4 orientation. Phase separation of $Rb_3H(SO_4)_2$ single crystals does not destroy the morphology of the crystal. Crystal faces appear frosted after phase separation but overall the crystal resembles its original shape and transparency.

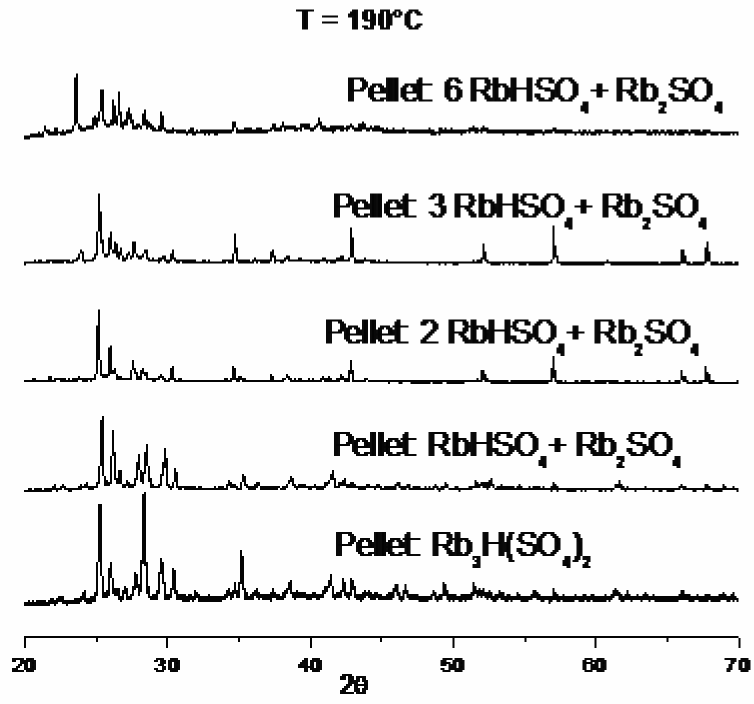

Figure 7-4. X-ray powder diffraction patterns of pressed powder samples of Rb_2SO_4 plus $RbHSO_4$ in various stoichiometric ratios. A clean pattern emerges for the 3 $RbHSO_4$ + Rb_2SO_4 pellet, and to a lesser extent in the 2 $RbHSO_4$ + Rb_2SO_4 pellet, which misleadingly suggests a high symmetry phase. This pattern is identical to the patterns (Figure 7-3) from single crystal $Rb_3H(SO_4)_2$ and a pellet of Rb_2SO_4, indicating oriented Rb_2SO_4 from $Rb_3H(SO_4)_2$ single crystal samples.

7.4 Thermal Analysis

The DSC/TG profile of $Rb_3H(SO_4)_2$ at a scan rate of 5 K/min shows an endothermic peak at 204°C with a corresponding enthalpy of phase transition of 10.42 kJ/mol. The second endothermic peak at 231°C has a corresponding enthalpy of fusion of 8.81 kJ/mol. Thermogravimetric analysis (TGA) detected a 2wt% weight loss, due to the vaporization of water (Figure 7-5).

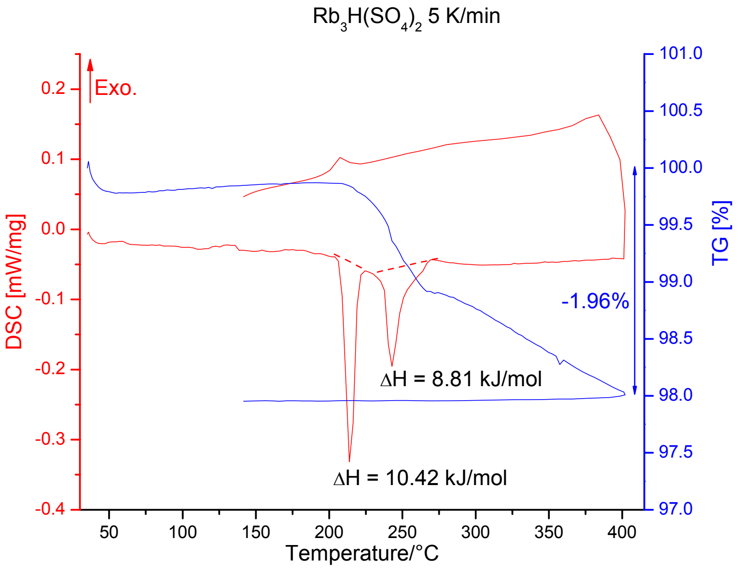

Figure 7-5. Differential scanning calorimetry (DSC) data of $Rb_3H(SO_4)_2$

7.4.1 Powder Sample

Temperature cycling of $Rb_3H(SO_4)_2$ powder samples indicates a reduction in the enthalpy of the transition on subsequent cycles (Figure 7-6). This implies that the $Rb_3H(SO_4)_2$ is decomposing while no weight loss is indicated by the TG scans on cycling. This data supports phase separation at 200°C. One possible explanation of this behavior is on cycling in a powder sample, phase separated $Rb_3H(SO_4)_2$ remains as two separate compounds. By the fourth cycle, the transition has completely diminished.

Another notable feature of the DSC cycles is that the transition temperature is reduced on cycling, further evidence that the transition is not a traditional solid ⟶ solid or even solid⟶liquid phase transition. Phase transition temperatures of solid ⟶ solid or solid⟶liquid phase transitions are generally expected to be reproducible.

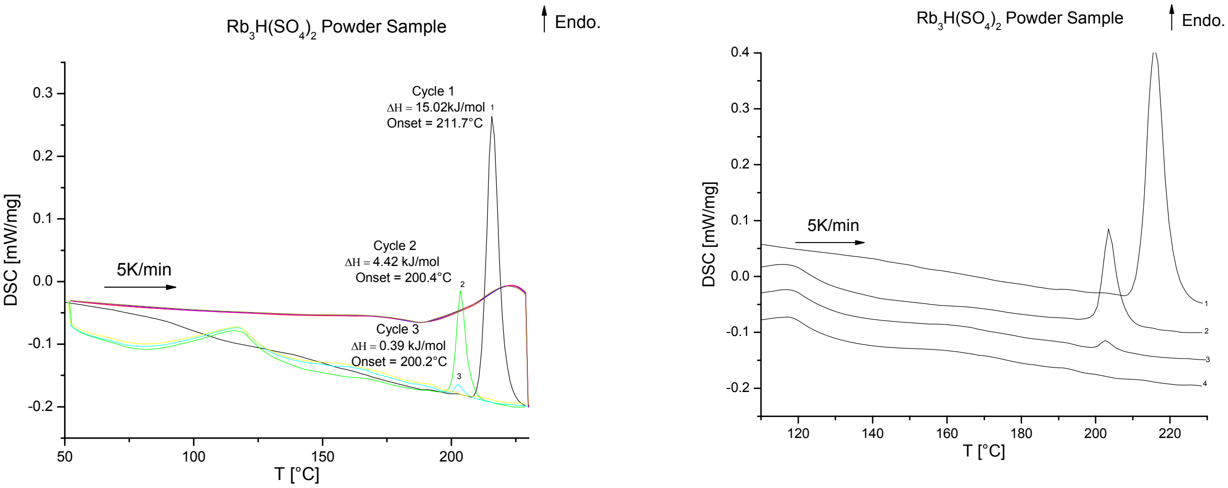

Figure 7-6. Differential scanning calorimetry (DSC) cycles on loose powder samples of $Rb_3H(SO_4)_2$

7.4.2 Pellet Sample

Differential scanning calorimetry on pressed-pellet samples of $Rb_3H(SO_4)_2$ show a similar trend to that seen in loose-powder samples, except to a lesser degree (Figure 7-7). The enthalpy of the phase transition around 200°C decreases and a new endothermic peak appears around 190°C, possibly from $RbHSO_4$ melting. As in the loose-powder sample, the transition temperature is reduced on cycling.

This data shows that pellet samples maintain a significantly larger fraction of the beginning material $Rb_3H(SO_4)_2$ on thermal cycling, which verifies the differences seen in powder and pellet samples under high-temperature X-ray diffraction.

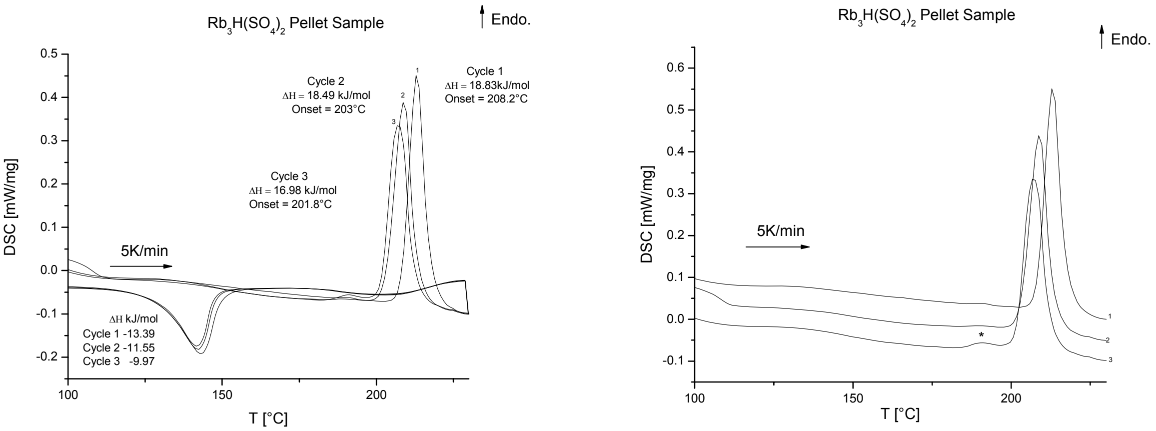

Figure 7-7. Differential scanning calorimetry (DSC) cycles on pressed pellet samples of $Rb_3H(SO_4)_2$

7.5 Phase Transition Temperatures: Extrapolation Down to Zero Heating Rate and $RbHSO_4$ Phase Diagram

A series of DSC experiments at different heating rates was performed on $Rb_3H(SO_4)_2$ and $RbHSO_4$ to determine the precise transition temperature. $RbHSO_4$ shows a transition temperature of 191.12°C at zero heating rate while $Rb_3H(SO_4)_2$ shows a distinct randomness, commensurate with an untypical phase transition (Figure 7-8). Phase separation of $Rb_3H(SO_4)_2$ does not follow a trend with different heating rates. Intuitively, one would expect lower transition temperatures for lower heating rates; however, the scatter in the data does not support this assumption.

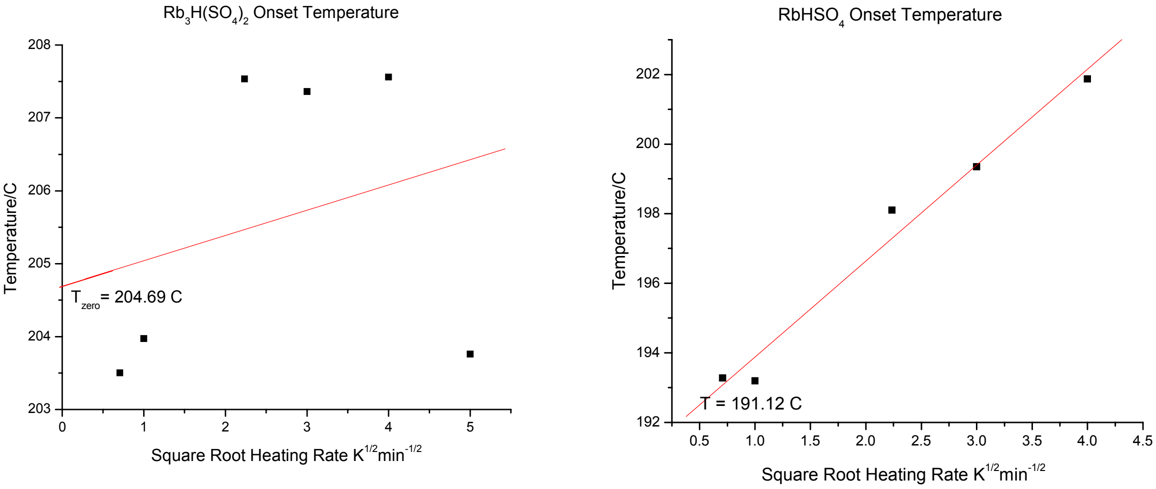

Figure 7-8. Extrapolation down to zero heating rate for (left) $Rb_3H(SO_4)_2$ and (right) $RbHSO_4$ compounds

Different stoichiometries were explored to confirm diffraction data was indicative of a phase separation and not discovery of a new phase (Figure 7-4). No new phases exist from the stoichiometries studied here. Phase separations of $Rb_3H(SO_4)_2$ and $RbHSO_4$ are indicated by horizontal lines on the phase diagram. The details of the phase separation temperatures and order are unclear, as they seem to occur within a few degrees of each other.

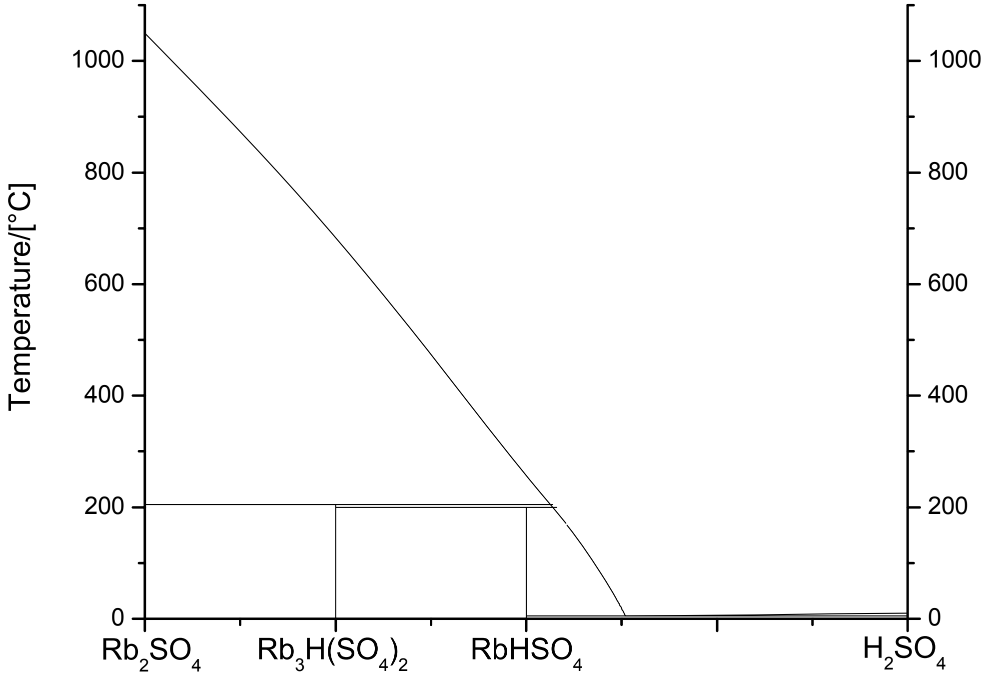

Figure 7-9. Possible phase diagram for Rb_2SO_4-H_2SO_4

7.6 Drop Solution Calorimetry and Enthalpy of Formation

Enthalpies of formation were determined via high-temperature drop solution calorimetry in molten sodium molybdate solvent ($3Na_2O{\cdot}4MO_3$) in a custom built Tian-Calvet microcalorimeter operating at 702°C. The calorimeter and standard procedures have been described previously [10]. 15 mg pellets were pressed from powder samples and dropped from room temperature into solvent. Oxygen gas was simultaneously flushed over the solvent at 100 ml/min to maintain an oxidizing atmosphere. The heat effect is recorded as a voltage change in the thermopile versus time curve. The area under the curve is proportional to the heat effect; the integrated voltage versus time curve was converted to enthalpy by application of a calibration factor based on the heat content of Al_2O_3 pellets of similar mass as the rubidium sulfate samples. The solution calorimetry of sulfates in $2Na_2O.4MoO_3$ solvent at 702°C has been carried out previously [11]. All of the samples in this study dissolved in approximately 40 minutes.

The rubidium sulfate samples dissolved in sodium molybdate solvent ($3Na_2O{\cdot}4MO_3$) at 702°C. The enthalpy of formation ($\Delta H_{f,ox}$) for oxides and enthalpy of formation ($\Delta H^o{}_f$) of the respective samples was calculated through a set of appropriate thermochemical cycles (using Rb_2O, SO_3, and H_2O as reference states) as shown in Table 7-2. The experimental heat of drop solution (ΔH_{ds}) values for oxides and sulfate samples utilized in the thermochemical cycles are presented in Table 7-3. The experimental $\Delta H^o{}_f$, $RbHSO_4$, and Rb_2SO_4 agrees with the reported values [12-14] within experimental errors (Table 7-4). The $\Delta H^o{}_f$ for $Rb_3H(SO_4)_2$ could not be compared, since no reported value was found in literature. Typically, the $\Delta H_{f,ox}$ and $\Delta H^o{}_f$ deduced from high-temperature drop solution experiments have an associated error of about ± 2-3 kJ/mol. However, for these rubidium sulfate samples, the $\Delta H_{f,ox}$ and $\Delta H^o{}_f$ shown in this work suffer a large error propagated from $\Delta H^o{}_f\,(Rb_2O) = -338.90 \pm 8.37$. The high reactivity of rubidium oxide makes it difficult to use directly for high-temperature oxide-melt solution calorimetry. The drop solution enthalpy of Rb_2O can be obtained from calorimetry performed using Rb_2CO_3 with known formation enthalpy. The large error on the calculated $\Delta H_{ds}\,(Rb_2O) = -332.5 \pm 9.0$ is attributed to the large error on $\Delta H^o{}_f\,(Rb_2O)$ [15]. This error further propagates in the $\Delta H_{f,ox}$ and $\Delta H^o{}_f$ rubidium sulfate samples and increases the error bar to 10 kJ/mol, as shown in Table 7-4. However, the error does not propagate in the reactions below. The phase separation of $Rb_3H(SO_4)_2$ is described by the following reaction:

$$Rb_3H(SO_4)_2 \rightarrow RbHSO_4 + Rb_2SO_4$$

The enthalpy of reaction can be described by the following expression:

$$\Delta H_{rx} = \Delta H_{ds}\,(Rb_3H(SO_4)_2) - \Delta H_{ds}\,(RbHSO_4) - \Delta H_{ds}\,(Rb_2SO_4)$$

The calculated ΔH_{rx} is equal to 0.85 ± 2.73 kJ/mol. The reaction enthalpy calculated from our heat of drop solution measurements does not conclusively support or refute our claim that $Rb_3H(SO_4)_2$ phase separates into $RbHSO_4$ plus Rb_2SO_4, as indicated by our x-ray diffraction results, since the value could be slightly negative or slightly positive, given the uncertainties, and the entropy of transition can not be calculated. It is clear, however, that the two phase assemblages are essentially the same in energy.

Reaction	Enthalpy
(1) $Rb_3H(SO_4)_2$ (cr, 298 K) → 3/2 Rb_2O (sol, 975 K) + ½ H_2O (g, 975 K) + 2 SO_3 (sol, 975 K)	$\Delta H_1 = \Delta H_{ds}$ ($Rb_3H(SO_4)_2$)
(2) Rb_2O (cr, 298 K) → Rb_2O (sol, 975 K)	$\Delta H_2 = \Delta H_{ds}$ (Rb_2O)
(3) H_2O (l, 298 K) → H_2O (g, 975 K)	$\Delta H_3 = \Delta H_{rx}$ (H_2O)
(4) SO_3(g, 298 K) → SO_3 (sol, 975 K)	$\Delta H_4 = \Delta H_{ds}$ (SO_3)
3/2 Rb_2O (cr, 298 K) + ½ H_2O (l, 298 K) + 2 SO_3 (g, 298 K) → $Rb_3H(SO_4)_2$ (cr, 298 K)	$\Delta H_{f,ox}$ ($Rb_3H(SO_4)_2$) = - ΔH_1 + 3/2 ΔH_2 + ½ ΔH_3 + 2 ΔH_4
ΔH^o_f ($Rb_3H(SO_4)_2$) = $\Delta H_{f,ox}$ ($Rb_3H(SO_4)_2$) + 3/2 ΔH^o_f (Rb_2O) + ½ ΔH^o_f (H_2O) + 2 ΔH^o_f (SO_3)	
(1) $RbHSO_4$ (cr, 298 K) → ½ Rb_2O (sol, 975 K) + ½ H_2O (g, 975 K) + SO_3 (sol, 975 K)	$\Delta H_1 = \Delta H_{ds}$ ($RbHSO_4$)
(2) Rb_2O (cr, 298 K) → Rb_2O (sol, 975 K)	$\Delta H_2 = \Delta H_{ds}$ (Rb_2O)
(3) H_2O (l, 298 K) → H_2O (g, 975 K)	$\Delta H_3 = \Delta H_{rx}$ (H_2O)
(4) SO_3(g, 298 K) → SO_3 (sol, 975 K)	$\Delta H_4 = \Delta H_{ds}$ (SO_3)
½ Rb_2O (cr, 298 K) + ½ H_2O (l, 298 K) + SO_3 (g, 298 K) → $RbHSO_4$ (cr, 298 K)	$\Delta H_{f,ox}$ ($RbHSO_4$) = - ΔH_1 + ½ ΔH_2 + ½ ΔH_3 + ΔH_4
ΔH^o_f ($RbHSO_4$) = $\Delta H_{f,ox}$ ($RbHSO_4$) + ½ ΔH^o_f (Rb_2O) + ½ ΔH^o_f (H_2O) + ΔH^o_f (SO_3)	
(1) Rb_2SO_4 (cr, 298 K) → Rb_2O (sol, 975 K) + SO_3 (sol, 975 K)	$\Delta H_1 = \Delta H_{ds}$ ($RbHSO_4$)
(2) Rb_2O (cr, 298 K) → Rb_2O (sol, 975 K)	$\Delta H_2 = \Delta H_{ds}$ (Rb_2O)
(3) SO_3(g, 298 K) → SO_3 (sol, 975 K)	$\Delta H_3 = \Delta H_{ds}$ (SO_3)
Rb_2O (cr, 298 K) + SO_3 (g, 298 K) → Rb_2SO_4 (cr, 298 K)	$\Delta H_{f,ox}$ (Rb_2SO_4) = - ΔH_1 + ΔH_2 + ΔH_3
ΔH^o_f (Rb_2SO_4) = $\Delta H_{f,ox}$ (Rb_2SO_4) + ΔH^o_f (Rb_2O) + ΔH^o_f (SO_3)	

Table 7-2. Thermochemical cycles used to calculate enthalpies of formation

Sample	ΔH_{ds} (kJ/mol)*
$Rb_3H(SO_4)_2$	261.06 ± 1.99 (8)†
$RbHSO_4$	109.24 ± 1.11 (12)
Rb_2SO_4	150.97 ± 1.51 (12)
Rb_2O	-332.5 ± 9.0 (8)[a]
SO_3	-217.0 ± 4.1 (8)[b]

* The associated measurement error represents two standard deviations (2σ) of the mean.
[a] Reference [15] and [b] reference [11]
† The value in ( ) represents the number of experiments.

Table 7-3. Enthalpies of drop solution (ΔH_{ds}) of $Rb_3H(SO_4)_2$, $RbHSO_4$, rubidium sulfate, and oxides

Sample	ΔH_f^o (kJ/mol)*	ΔH_f^o (kJ/mol)* (this work)	ΔH_f^o (kJ/mol)* (Lange's Handbook of Chemistry (1992))[12]	ΔH_f^o (kJ/mol)* Glushko and Medvedev [13, 14]
$Rb_3H(SO_4)_2$	-1159.26 ± 10.09	-2602.22 ± 10.09	--	--
$RbHSO_4$	-457.94 ± 9.95	-1166.16 ± 9.95	-1159	-1162.32 ± 2.09
Rb_2SO_4	-700.47 ± 10.00	-1435.22 ± 10.00	-1435.61	-1437.12 ± 0.46
Rb_2O			-339	-338.90 ± 8.37
H_2O			-285.83	-285.83 ± 0.04
SO_3			-395.77	-395.85 ± 0.38

* The associated measurement error represents two standard deviations (2σ) of the mean.

Table 7-4. Enthalpies of formation of $Rb_3H(SO_4)_2$, $RbHSO_4$, rubidium sulfate, and oxides

7.7 Conductivity Studies

The conductivity of pressed pellet samples (P = 4 tons, diameter = 10 mm, 5 minutes pressing time) were measured under wet nitrogen in the temperature range of room temperature to 270°C. Silver electrodes were painted onto the surfaces of the $Rb_3H(SO_4)_2$ sample pellet with silver paint (Ted Pella). A.C. impedance data were collected over the frequency range of 20Hz – 1MHz using an HP 4284 precision LCR meter at an applied voltage of 50 mV. Zview (Scribner Associates Inc.), a least-squares refinement program, was utilized to fit the acquired impedance data to several different equivalent circuits including (RQ), (R1Q1)(R2Q2), (R1)(R2Q2), etc. where *R* is resistance and *Q* is constant phase element with impedance $Z_Q = (Y(j\omega)^n)^{-1}$; where $j = \sqrt{-1}$, ω = frequency, Y and n are constants, and n ranges between 0 and 1.

Impedance spectroscopy scans of $Rb_3H(SO_4)_2$ show jumps in conductivity at T = 205°C, 237°C, and 267°C, the first of which has every appearance of a superprotonic phase transition and is reversible (Figure 7-10). The hysterisis of the transition at 205°C is approximately 25°C, which is not unusual for superprotonic transitions. The activation energy in this phase is 0.598 eV/atom which is within range of reported values for actual superprotonic phase transitions (1/3 – 2/3 eV/atom) and so this data deceptively resembles a sought-after superprotonic phase transition. The transitions at higher temperatures are not reproducible and result in a loss of the lower phase transition at 205°C. The details of these higher-temperature transitions are not clear but are believed to be due to dehydration and plastic deformation of the pellet sample, resulting in a thinner pellet with inherently lower resistance. Heating and cooling cycle 3 show that the pellet at all temperatures is higher in conductivity, which supports the claim that the pellet sample has been deformed in the sample holder.

As phase separation into $RbHSO_4$ and Rb_2SO_4 is the expected transition at ~ 200°C, impedance data was measured on a pellet of $RbHSO_4$ and Rb_2SO_4. Powder X-ray diffraction carried out on the $RbHSO_4$ and Rb_2SO_4 pellet showed dual phase with no reactions. The conductivity plot shows that a phase separation rather than a superprotonic phase transition is a very plausible explanation of the data for $Rb_3H(SO_4)_2$ (Figure 7-10 (right)).

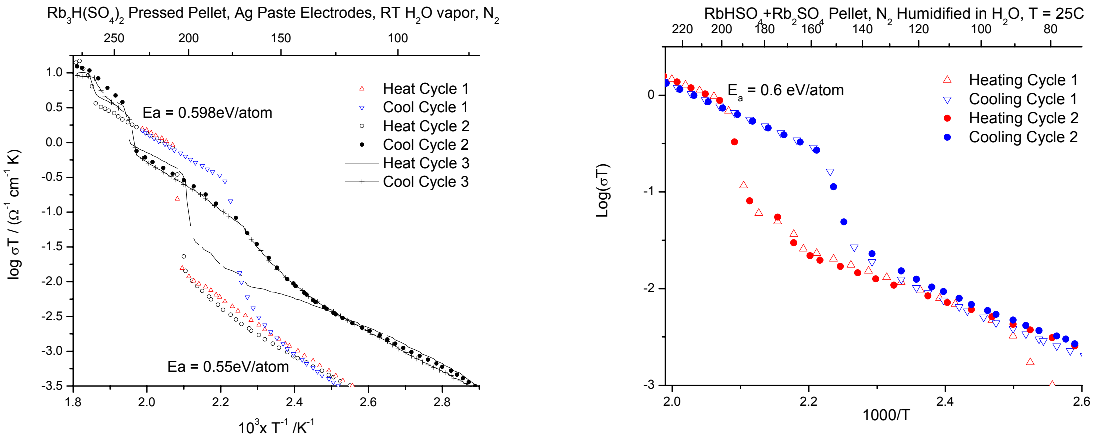

Figure 7-10. ACIS conductivity plot of (left) $Rb_3H(SO_4)_2$ pellet sample and (right) $RbHSO_4$ plus Rb_2SO_4 pellet sample

7.8 Thermo-Mechanical Measurements

A Perkin Elmer TMA 7 Thermomechanical Analyzer was utilized for these thermo-mechanical tests, recording changes in probe position under an applied force at various temperatures. Changes in probe position were used to signify a solid to solid phase transition and a solid to liquid phase transition.

Thermomechanical analysis (TMA) experiments on a $Rb_3H(SO_4)_2$ pressed pellet sample show a rise in probe position, indicative of an increase in volume at ~ 200°C and then a subsequent sharp decrease. The increase in the linear dimension probed at ~ 200°C is approximately 3.45%, which results in an oversimplified volume increase of 11%, assuming cubic symmetry. The ratio of the average of the unit cell volumes of $RbHSO_4$ and Rb_2SO_4 to $Rb_3H(SO_4)_2$ results in an increase of 2.44%. The fact that the linear estimate overshoots the expected volume suggests that the phase separation initially proceeds from $Rb_3H(SO_4)_2\,(s) \longrightarrow RbHSO_4\,(s) + Rb_2SO_4\,(s)$, and only after an increase in temperature does $RbHSO_4$ melt. $RbHSO_4$ TMA experiments indicate a melting transition at 214°C.

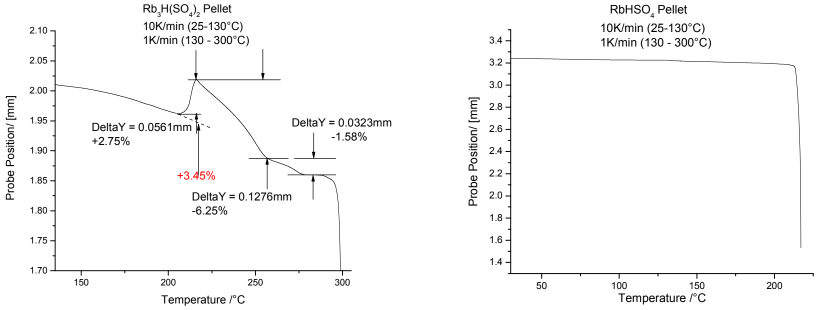

Compound:	**Unit Cell Volume Å^3**
$Rb_3H(SO_4)_2$	**887.56**
$RbHSO_4$	**842.08**
Rb_2SO_4	**488.18**
50% Rb_2SO_4 + 50% $RbHSO_4$	**909.22**

Figure 7-11. Thermomechanical data for $Rb_3H(SO_4)_2$ and $RbHSO_4$ pressed pellet samples

7.9 $M_3H(XO_4)_2$ Phase Transitions

Compounds in the $M_3H(XO_4)_2$, (where M = NH_4, K, Rb, Cs and X = S, Se) family exist in the A2/a structure or C2/c and with some exceptions transform to the $R\bar{3}m$ structure at elevated temperatures. As shown in this chapter, $Rb_3H(SO_4)_2$, is not stable in the $R\bar{3}m$ structure and phase separates into Rb_2SO_4 and $RbHSO_4$, which subsequently phase separate into Rb_2SO_4 and H_2SO_4. Another compound in the $M_3H(XO_4)_2$ system that exhibits properties similar to $Rb_3H(SO_4)_2$, $K_3H(SO_4)_2$, has also been reported as superprotonic [16]. In light of the evidence against the stability of the $Rb_3H(SO_4)_2$ superprotonic phase, $K_3H(SO_4)_2$ will need to be re-examined.

7.10 Conclusions

Despite earlier claims that suggests a superprotonic phase, careful examination of X-ray diffraction data in conjunction with TMA, DSC, and impedance spectroscopy indicate that $Rb_3H(SO_4)_2$ phase separates into $RbHSO_4$ and Rb_2SO_4 at 205°C. $RbHSO_4$ is also found to melt incongruently, $RbHSO_4\ (s) \longrightarrow H_2SO_4\ (l) + Rb_2SO_4\ (s)$. The overall reaction enthalpy of the phase separation is within error of 0 J/mol K. Other compounds in the $M_3H(XO_4)_2$ system, specifically $K_3H(SO_4)_2$, are expected to phase separate as well, in light of this study on $Rb_3H(SO_4)_2$.

7.11 References

1. Matsuo, Y., et al. Trithallium Hydrogen Bis(sulfate), $Tl_3H(SO_4)_2$, in the Superionic Phase by X-Ray Powder Diffraction. Acta Crystallographica Section C – Crystal Structure Communications, 2002, **58**: I92 – I94.

2. Matsuo, Y., K. Takahashi, and S. Ikehata. Phase Transitions in Trithallium Hydrogen Disulfate $Tl_3H(SO_4)_2$. Solid State Communications, 2001, **120**(2 – 3): 85 – 88.

3. Onoda-Yamamuro, N., et al. Neutron Diffraction Study on Hydrogen Bond Structure in $K_3H(SeO_4)_2$ and $K_3D(SeO_4)_2$ Crystals. Journal of Physics – Condensed Matter, 2000, **12**(40): 8559 – 8565.

4. Shikanai, F., et al. Neutron Powder Diffraction Study on the High-Temperature Phase of $K_3H(SeO_4)_2$. Physica B-Condensed Matter, 2006, **385**: 156 – 159.

5. Lukaszewicz, K., A. Pietraszko, and M.A. Augustyniak. Structure of $(NH_4)_3H(SeO_4)_2$ in High-Temperature Phase-I and Phase-II. Acta Crystallographica Section C – Crystal Structure Communications, 1993, **49**: 430 – 433.

6. Pietraszko, A., B. Hilczer, and A. Pawlowski. Structural Aspects of Fast Proton Transport in $(NH_4)_3H(SeO_4)_2$ Single Crystals. Solid State Ionics, 1999, **119**(1 – 4): 281 – 288.

7. Pietraszko, A. and K. Lukaszewicz. Crystal-Structure of $(NH_4)_3H(SeO_4)_2$ in the Low-Temperature Phase-IV. Bulletin of the Polish Academy of Sciences – Chemistry, 1993, **41**(3): 157 – 162.

8. Pietraszko, A., K. Lukaszewicz, and M.A. Augustyniak. Structure of Phase – III of $(NH_4)_3H(SeO_4)_2$. Acta Crystallographica Section C – Crystal Structure Communications, 1992, **48**: 2069 – 2071.

9. Sinitsin, V.V., et al. Superionic Conductivity and P-T Phase-Diagram of $RbHSO_4$. Fizika Tverdogo Tela, 1988, **30**(9): 2838 – 2841.

10. Navrotsky, A. Progress and New Directions in High-Temperature Calorimetry Revisited. Physics and Chemistry of Minerals, 1997, **24**(3): 222 – 241.

11. Majzlan, J., A. Navrotsky, and J. Neil. Energetics of Anhydrite, Barite, Celestine, and Anglesite: A High-Temperature and Differential Scanning Calorimetry Study. Geochimica et Cosmochimica Acta, 2002, **66**(10): 1839 – 1850.

12. Dean, J.A. Lange's Handbook of Chemistry. McGraw-Hill, 1992.

13. Glushko, V., et al. Reference handbooks for thermodynamic properties of materials published by academy of sciences of USSR. High Temperature, 1974, **12**(5): 853 – 858.

14. Glushko, V.P., ed. Termicheskie konstanty veshchestv. Spravochnik. Akademiia nauk SSSR, 1980, 8.

15. Ushakov, S., et al. Thermochemistry of the alkali rare-earth double phosphates, $A_3RE(PO_4)_2$. Journal of Materials Research, 2004, **19**(7): 2165 – 2175.

16. Chisholm, C.R.I. and S.M. Haile. High-temperature phase transitions in $K_3H(SO_4)_2$. Solid State Ionics, 2001, **145**(1-4): 179 – 184.

Chapter 8 Conclusions

Engineering the properties of solid acid materials for fuel cell electrolyte applications requires an understanding of the structural and chemical parameters that support superprotonic phase transitions over melting or decomposition. This work presents clarified structural information for the superprotonic phase of $CsDSO_4$, $RbDSeO_4$, and CsD_2PO_4 with new insights from the neutron pair distribution function and compares configuration entropy derived from these structures (average and local) to experimental data. This work also describes the cation size effect in the $Cs_xRb_{1-x}H_2PO_4$ system as well as identifies a previously misinterpreted high-temperature transition of $Rb_3H(SO_4)_2$.

Of the three best structural models reported in the literature for the superprotonic phase of $CsHSO_4$ (Jirak, Belushkin, and Merinov) [1-3], this work deems the Jirak model as the best description of sulfate disorder. New high-resolution neutron powder diffraction data supports the Jirak model for the high-temperature phase of superprotonic conductor $CsDSO_4$. A Hamilton’s test for the significance of added refinement parameters cannot support rejecting the hypothesis that there is a single oxygen and deuterium site, as proposed in the Jirak structure. Entropy calculations based on the Jirak model agree well with experimental data.

The superprotonic structure of $RbDSeO_4$ has been identified in the $I4_1/amd$ space group. Previously, attempts at determining this structure using X-ray diffraction suffered from a lack of resolution between rubidium and selenium atoms, resulting in a more symmetric structure as well as an inability to locate hydrogen positions. In this work,

$RbDSeO_4$ has been identified to be in the Merinov model (with split deuterium and oxygen positions) of a tetragonal $I4_1/amd$ space group, and entropy calculations based on the Merinov model agree well with experimental data.

Accurate characterization of CsH_2PO_4 shows a very clear picture of the superprotonic phase average structure. High-resolution neutron powder diffraction data has been refined in a $Pm\bar{3}m$ structure assigning deuterium positions and oxygen positions. Pair distribution function data indicates that the number of configurations the phosphate tetrahedra samples is not strictly delimited by the Bragg diffraction average structure. The configurational entropy of the superprotonic phase, with insights from PDF analysis, agrees well with experimental data. Pretransitional effects in CsD_2PO_4 show an increase in mobility of the deuterium positions 50°C before the actual superprotonic transition. Curiously, this disorder is not reflected in the chemical shift anisotropy of the phosphorous atom.

Pair distribution function analysis illustrates that there is a difference between average and local structure in the superprotonic phase, which is a testament to the high mobility of the deuterium atom in the superprotonic phase. Local structure does not seem to conform with great fidelity to the average structure refined by Bragg diffraction.

A study of chemical intermediates, $Cs_xRb_{1-x}H_2PO_4$, provides valuable insight into the nature of the cation size effect on superprotonic phase transitions within an isostructural system. For compounds in the series that do exhibit a superprotonic phase, CsH_2PO_4 – $Cs_{0.3}Rb_{0.7}H_2PO_4$, the magnitude of proton conductivity remains neutral to rubidium incorporation. Altering the effective cation size shows a profound impact on transition temperature for compounds with high rubidium content ($x < 0.5$) while preserving the overall conductivity of the high-temperature and low-temperature phases. X-ray diffraction, thermal analysis, Raman, IR, ^{133}Cs, ^{87}Rb and ^{1}H-NMR spectroscopy all attest to the gradual variation in structural properties across the composition range.

Misleading data from a compound in the $M_3H(XO_4)_2$ family, $Rb_3H(SO_4)_2$, has been interpreted in the literature as a superprotonic transition. Evidence presented supports the claim that at high temperatures (T ~ 200°C),

$$Rb_3H(SO_4)_2\,(s) \leftrightarrow Rb_2SO_4\,(s) + RbHSO_4\,(l),$$

where phase separation from the solid phase into rubidium sulfate and rubidium hydrogen sulfate mimics a superprotonic phase, due to the high proton mobility in the rubidium hydrogen sulfate melt. While investigating the above transition, the incongruent melt of

$$RbHSO_4\,(s) \leftrightarrow Rb_2SO_4\,(s) + H_2SO_4\,(l)$$

was also identified.

Appendix

A.1 Solid Acid Synthesis

A.1.1 Cesium dihydrogen phosphate, CsH_2PO_4

CsH_2PO_4 powder samples were precipitated out of a solution containing stoichiometric amounts of Cs_2CO_3 and H_3PO_4 with excessive methanol (200 mL). Resulting powder was vacuum filtered and dried in an oven at 90°C. Example synthesis amounts: Cs_2CO_3, 30 grams; H_3PO_4(85% assay), 21.23 grams.

A.1.2 Cesium hydrogen phosphite, $CsHPO_3H$

$CsHPO_3H$ powder sample was made by adding Cs_2CO_3 and H_3PO_3 together in stoichiometric amounts. A small amount of DI water was added to completely dissolve mixture. Powders precipitated out by evaporating excess water off at 80°C. Resulting compound is highly deliquescent and must be heated to 80°C – 110°C to prevent being dissolved by the water vapor content in ambient air. Storage in well-maintained desiccator is acceptable. Example synthesis amounts: Cs_2CO_3, 15 grams; H_3PO_3, 7.55 grams.

A.1.3 Cesium hydrogen sulfate, $CsHSO_4$

$CsHSO_4$ powder samples were precipitated out of a solution containing stoichiometric amounts of Cs_2SO_4 and H_2SO_4 with acetone. Example synthesis amounts: Cs_2SO_4, 15 grams; H_2SO_4 (~ 96% assay), 8.43 grams.

A.1.4 Cesium$_x$rubidium$_{1-x}$ dihydrogen phosphate, $Cs_xRb_{1-x}H_2PO_4$

Compounds in the $Cs_xRb_{1-x}H_2PO_4$ system were synthesized in increments of x = 0.1. Stoichiometric amounts of CsH_2PO_4 and RbH_2PO_4 were mixed in a thermal bomb with 1 – 2 mL H_2O to prevent dehydration, and held at 350°C for three hours to allow homogeneous melting.

A.1.5 Potassium hydrogen selenate, $KHSeO_4$

Powder samples of $KHSeO_4$ were prepared in aqueous solution by combining K_2CO_3 and H_2SeO_4 in excess and precipitating by heating at 80°C. Resulting crystals were filtered and subsequently washed with methanol. (Acetone cannot be used to rinse a selenate compound as it reacts with trace amounts of selenic acid and will contaminate the synthesis.) Example synthesis amounts: K_2CO_3, 5 grams; H_2SeO_4 (40% assay), 39.34 grams.

A.1.6 Rubidium hydrogen selenate, $RbHSeO_4$

$RbHSeO_4$ powder samples were precipitated out of a solution containing Rb_2CO_3 and excess H_2SeO_4 by heating solution at 80°C for several hours and then cooling the concentrated mixture to 0°C over an ice block. After vacuum filtering for *hours* to remove excess selenic acid, powder crystals were rinsed with methanol. If sufficient time is not allowed during filtering, rinsing with methanol will produce a pink tint in the crystals. (Do not use acetone to rinse a selenate compound.) Example synthesis amounts: Rb_2CO_3, 30 grams; H_2SeO_4 (40% assay), 150 grams.

A.1.7 Rubidium hydrogen sulfate, $RbHSO_4$

$RbHSO_4$ crystals were grown by slow evaporation of an aqueous solution of dissolved Rb_2SO_4 (Alfa Aesar 99% purity) and excess H_2SO_4 in the molar ration of 1/2:4/3, respectively. Large crystals resulted and were vacuum dried to get all excess mother liquor off the crystal faces, then rinsed quickly with DI water to remove excess acid and subsequently with acetone and placed in an oven at 80°C for 12 hours to dry. Methanol should not be used to wash $RbHSO_4$ crystals. Example synthesis amounts: Rb_2SO_4, 30 grams; H_2SO_4 (96.4% assay), 22.86 grams; $RbHSO_4$ (theoretical yield) 41.02 grams.

A.1.8 Trirubidium hydrogen disulfate, $Rb_3H(SO_4)_2$

Crystalline powders of $Rb_3H(SO_4)_2$ were synthesized by dissolving Rb_2SO_4 (Alfa Aesar 99% purity) into deionized (DI) water and adding H_2SO_4 in the molar ration of 3/4:1, respectively. Powder precipitate was formed by adding methanol. The resulting crystals were vacuum filtered and rinsed with additional methanol and dried for only a short period of time at 80°C. Example synthesis amounts: Rb_2SO_4, 30 grams; H_2SO_4 (96.4% assay), 15.24 grams; $Rb_3H(SO_4)_2$ (theoretical yield) 33.67 grams.

A.1.9 Trirubidium hydrogen diselenate, $Rb_3H(SeO_4)_2$

$Rb_3H(SeO_4)_2$ powder samples were precipitated out of a solution containing Rb_2CO_3 and excess H_2SeO_4 by slow evaporation at 80°C on a hot plate. Adding H_2SeO_4 to Rb_2CO_3 generates heat and so this addition was performed in a beaker surrounded by an ice pack to prevent selenic acid decomposition or evaporation. (Do not use acetone to rinse a selenate compound.) Example synthesis amounts: Rb_2CO_3, 30.03 grams; H_2SeO_4, 94.17 grams.

A.1.10 Rubidium dihydrogen arsenate, RbH_2AsO_4

Rb_2CO_3 and $H_5As_3O_{10}$ were combined in stoichiometric amounts, dissolved in DI water and precipitated with methanol addition. Example synthesis amounts: Rb_2CO_3, 35.54 grams; $H_5As_3O_{10}$, 40 grams.

A.1.11 Thallium hydrogen sulfate, $TlHSO_4$

$TlHSO_4$ crystal samples were grown via slow evaporation in a refrigerator (~ 5 – 10°C) in a solution containing Tl_2SO_4 and excess H_2SO_4. Example synthesis amounts: Tl_2SO_4, 5 grams; H_2SO_4, 8.03 grams.

A.1.12 Deuteration of solid acid samples

Samples for neutron diffraction analysis were deuterated to greater than 99% deuteration by the following method:

1. Dissolve phase pure solid acid sample—$CsHSO_4$, for example—in D_2O.
2. Freeze dry resulting solution in a flask isolated from ambient air with a glass valve between flask and freeze dryer.
3. Inject D_2O with a syringe through a rubber diaphragm to cover inlet orifice and isolate sample from ambient air. Make sure all solid acid is redissolved and then freeze dry.

4. Repeat step 3 at least five times to ensure high deuteration level. Check deuteration level with ^1H and ^2H NMR.

A.2 Melting Point Determinations via Capillary Melting Point Apparatus

A Thomas Hoover Uni-Melt apparatus was utilized to visually confirm melting points for a few compounds in capillary tubes placed in a heated oil bath.

Compound:	Melting Temperature
$KHSeO_4$	215 – 225°C
RbH_2AsO_4	>300°C
$RbHSeO_4$	220 – 227°C
$CoCp_2[H_3PO_4][H_2PO_4]$	143°C
$CsHSO_4$	210 – 215°C
$Rb_3H(SO_4)_2$	274°C*
$RbHSO_4$	210 – 215°C

*Physical appearance of melting does not represent melting of $Rb_3H(SO_4)_2$. As shown in this work, $Rb_3H(SO_4)_2$ phase separates into Rb_2SO_4 plus $RbHSO_4$ and this composite mixture appears to melt at this temperature. $RbHSO_4$, however, melts at lower temperatures which is not clearly discernable when melting $Rb_3H(SO_4)_2$.

A.3 Three-Site Chemical Exchange Mathematica Program

Three-Site Exchange, T = 25°C:

$$\delta_{D1} = 4.97;\ \delta_{D2b} = 7.15;\ \delta_{D2a} = 2.54;\ \Omega = .50;\ \mathrm{FWHM}_{D1} = .58;\ \mathrm{FWHM}_{D2a} = .38;\ \mathrm{FWHM}_{D2b} = .72;$$

$$\mathrm{in}[\delta\_] = \begin{pmatrix} i * \delta_{D1} + \mathrm{FWHM}_{D1} & 0 & 0 \\ 0 & i * \delta_{D2a} + \mathrm{FWHM}_{D2a} & 0 \\ 0 & 0 & i * \delta_{D2b} + \mathrm{FWHM}_{D2b} \end{pmatrix};$$

$$P[\Omega\_] = \begin{pmatrix} \frac{-\Omega}{2} & \frac{\Omega}{4} & \frac{\Omega}{4} \\ \frac{\Omega}{2} & \frac{-\Omega}{4} & \frac{\Omega}{4} \\ \frac{\Omega}{2} & \frac{\Omega}{4} & \frac{-\Omega}{4} \end{pmatrix};$$

$$A[\delta\_, \Omega\_] = \mathrm{in}[\delta] - i \begin{pmatrix} w & 0 & 0 \\ 0 & w & 0 \\ 0 & 0 & w \end{pmatrix} + P[\Omega];$$

$$T[w\_] = (-2\ \ -1\ \ -1).\mathrm{Inverse}[A[\delta, \Omega]].\begin{pmatrix} 1 \\ 1 \\ 1 \end{pmatrix};$$

```
Plot[Abs[Re[T[w]]],{w,0,10}]
```

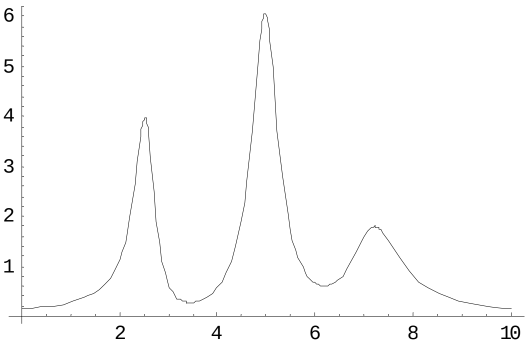

T=150°C:

$$\delta_{D1} = 4.97;\ \delta_{D2b} = 7.15;\ \delta_{D2a} = 2.54;\ \Omega = 12.50;\ \mathrm{FWHM}_{D1} = .58;\ \mathrm{FWHM}_{D2a} = .38;\ \mathrm{FWHM}_{D2b} = .72;$$

$$\mathbf{in}[\delta\_] = \begin{pmatrix} i*\delta_{D1} + \mathrm{FWHM}_{D1} & 0 & 0 \\ 0 & i*\delta_{D2a} + \mathrm{FWHM}_{D2a} & 0 \\ 0 & 0 & i*\delta_{D2b} + \mathrm{FWHM}_{D2b} \end{pmatrix};$$

$$\mathbf{P}[\Omega\_] = \begin{pmatrix} \frac{-\Omega}{2} & \frac{\Omega}{4} & \frac{\Omega}{4} \\ \frac{\Omega}{2} & \frac{-\Omega}{4} & \frac{\Omega}{4} \\ \frac{\Omega}{2} & \frac{\Omega}{4} & \frac{-\Omega}{4} \end{pmatrix};$$

$$\mathbf{A}[\delta\_, \Omega\_] = \mathbf{in}[\delta] - i \begin{pmatrix} w & 0 & 0 \\ 0 & w & 0 \\ 0 & 0 & w \end{pmatrix} + \mathbf{P}[\Omega];$$

$$\mathbf{T}[w\_] = (-2\ \ -1\ \ -1).\mathbf{Inverse}[\mathbf{A}[\delta, \Omega]].\begin{pmatrix} 1 \\ 1 \\ 1 \end{pmatrix};$$

```
Plot[Abs[Re[T[w]]],{w,-30,30}]
```

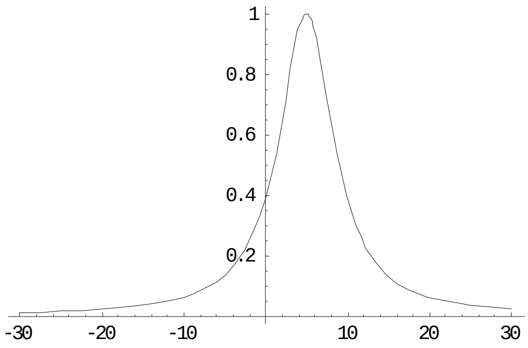

T=185°C:

$\delta_{D1} = 4.97;\ \delta_{D2b} = 7.15;\ \delta_{D2a} = 2.54;\ \Omega = 52.50;\ \mathrm{FWHM}_{D1} = .58;\ \mathrm{FWHM}_{D2a} = .38;\ \mathrm{FWHM}_{D2b} = .72;$

$$\mathrm{in}[\delta\_] = \begin{pmatrix} i*\delta_{D1} + \mathrm{FWHM}_{D1} & 0 & 0 \\ 0 & i*\delta_{D2a} + \mathrm{FWHM}_{D2a} & 0 \\ 0 & 0 & i*\delta_{D2b} + \mathrm{FWHM}_{D2b} \end{pmatrix};$$

$$\mathrm{P}[\Omega\_] = \begin{pmatrix} \frac{-\Omega}{2} & \frac{\Omega}{4} & \frac{\Omega}{4} \\ \frac{\Omega}{2} & \frac{-\Omega}{4} & \frac{\Omega}{4} \\ \frac{\Omega}{2} & \frac{\Omega}{4} & \frac{-\Omega}{4} \end{pmatrix};$$

$$\mathrm{A}[\delta\_, \Omega\_] = \mathrm{in}[\delta] - i \begin{pmatrix} w & 0 & 0 \\ 0 & w & 0 \\ 0 & 0 & w \end{pmatrix} + \mathrm{P}[\Omega];$$

$$\mathrm{T}[w\_] = (-2\ \ -1\ \ -1).\mathrm{Inverse}[\mathrm{A}[\delta, \Omega]].\begin{pmatrix} 1 \\ 1 \\ 1 \end{pmatrix};$$

```
Plot[Abs[Re[T[w]]],{w,-30,30}]
```

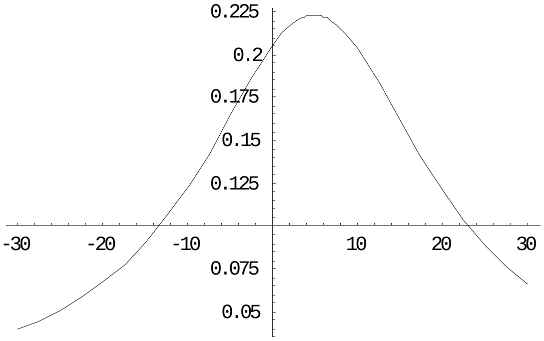

A.4 Refinement of Rb_2SO_4 Structure against $Rb_3H(SO_4)_2$ X-Ray Diffraction Data at 205°C and Rb_2SO_4 X-Ray Diffraction Data at 220°C.

Table A-1. Refinement of Rb_2SO_4 Structure against $Rb_3H(SO_4)_2$ X-Ray Diffraction Data at 205˚C

Structural Data	
Compound Name	Dirubidium sulfate
Chemical Formula	Rb_2SO_4
Molecular Weight/ $g \cdot mol^{-1}$	266.99
Space Group (No.)	P n m a (62)
Publication Authors	Weber, H.J.;Schulz, M.;Schmitz, S.;Granzin, J.;Siegert, H.
ICSD database code	203159
Lattice Parameters	
a/Å	7.8955(7)
b/Å	6.0286(5)
c/Å	10.5190(9)
α/˚	90
β/˚	90
γ/˚	90
Multiplicity, Z	4
Volume, V/ $Å^3$	500.697
Density, $\rho / g \cdot cm^{-3}$	3.54
Measurement Parameters	
Generator Settings	45 kV, 40 mA
Divergence Slit/˚	1.000
Scan-range, 2θ/˚	10.007 – 89.987
Step Size, 2θ/˚	0.017
Scan Time per Step/s	90.15
Scan Type	Continuous
Radiation	Cu *K*α
Temperature, T/˚C	185
Atmosphere	Ambient
Refinement Parameters	
Number of Variables	13

Displacement	0.083(2)
Profile fit	Pseudo-Voigt
Background	Refined
Coefficients for Peak FWHM	
U	0.0000
V	0.0000
W	0.0231(9)
Preferred Orientation	011
Preferred Orientation Parameter	1.090(5)
Asymmetry Parameter	1.01(7)
Refinement Statistics	
R_{exp}/%	2.576
R_p/%	3.217
R_{wp}/%	4.422
R_B/%	2.145
GOF	2.945
d-statistic	0.653

Table A-2. Refinement of Rb_2SO_4 Structure against Rb_2SO_4 X-Ray Diffraction Data at 220˚C

Structural Data	
Compound Name	Dirubidium sulfate
Chemical Formula	Rb_2SO_4
Molecular Weight/ $g \cdot mol^{-1}$	266.99
Space Group (No.)	P n m a (62)
Publication Authors	Weber, H.J.;Schulz, M.;Schmitz, S.;Granzin, J.;Siegert, H.
ICSD database code	203159
Lattice Parameters	
a/Å	7.9061(2)
b/Å	6.0355(2)
c/Å	10.5241(3)
α/˚	90
β/˚	90
γ/˚	90
Multiplicity, Z	4
Volume, V/ $Å^3$	502.182
Density, $\rho / g \cdot cm^{-3}$	3.53
Measurement Parameters	
Generator Settings	45 kV, 40 mA
Divergence Slit/˚	1.000
Scan-range, 2θ/˚	15.002 - 79.994
Step Size, 2θ/˚	0.004
Scan Time per Step/s	19.70
Scan Type	Continuous
Radiation	Cu *K*α
Temperature, T/˚C	220
Atmosphere	Ambient

Refinement Parameters	
Number of Phases	2
Weight Fraction/%	58.7(4)
Number of Variables	20
Displacement	
Profile fit	Pseudo-Voigt
Background	Refined
Coefficients for Peak FWHM	
U	0.0000
V	0.0000
W	0.0116(2)
Preferred Orientation	110
Preferred Orientation Parameter	1.354(5)
Asymmetry Parameter	0.9(1)
Refinement Statistics	
R_{exp}/%	3.333
R_p/%	4.222
R_{wp}/%	6.079
R_B/%	4.802
GOF	3.328
d-statistic	0.213

A.5 $KHSeO_4$ and $RbHSeO_4$ Quantum Chemical and ReaxFF$_{KSeRb}$ Development

Abstract

The equations of state for K, Rb, Rb oxides and K oxides have been calculated. Cluster calculations, condensed phase systems and bond dissociations in the selenic acid system have been calculated at the B3LYP/LACV3P**++ level and have been reproduced using a reactive force field, ReaxFF$_{KSeRb}$. Proton migration barriers have also been calculated and show an 8.8 kcal/mol energy barrier to the transfer of a proton from an oxygen in a $HSeO_4^-$ unit to another oxygen.

A.5.1 Introduction

$RbHSeO_4$ exhibits an order/disorder transition at 187°C from the B112 space group into a tetragonal unit cell whose crystal structure has been solved in this work. This transition has an entropy change of 10 J/mol K and is accompanied by an increase in protonic conductivity. The activation energy for bulk transport in the superprotonic phase has been determined experimentally to be 0.60 eV. $KHSeO_4$, undergoes a transition from Pbca to a trigonal space group although the structure is ambigous, ΔS = 11.753 J/mol K and T = 234°C. The $KHSeO_4$ transition, however, is not accompanied by an increase in protonic conductivity. These transitions and the structural prerequisites that govern the magnitude of a superprotonic phase transition are of great interest for developing new materials for use in fuel cells and sensors. The purpose of this study is to develop a predictive tool to judiciously choose which geometries and compositions may yield a superprotonic phase transition and are valuable to explore experimentally.

QC data was obtained for a range of compression and expansion points for potassium, rubidium, and a few examples of these metal oxides under a pressure range of -2 to 20 GPa. A number of clusters ($RbHSeO_4$, H_2SeO_4, SeO_3, $HSeO_4$, H_2SeO_3…) to describe bond dissociation and bond angle distortion were included in the QC test set used to train ReaxFFKRbSe. In conjunction with QC data, heats of formation of the metal oxides and cohesive energies of the metals were utilized.

A.5.2 Methods

Cluster calculations were performed at the B3LYP/LACV3P**++ level using *Jaguar* software. An ultrafine DFT grid was used and electrostatic potentials were fit to atomic centers. DFT was used to perform QC calculations on crystalline K, Rb, SeO_2, and rubidium and potassium oxides.

A.5.3 Results and Discussion

A.5.3.1 Bond Dissociations

To develop a reactive force field, the energetics and distances associated with bond forming and breaking were considered for an initial set of relevant clusters. To describe the fully dissociated limit of a cluster, higher spin states were evaluated. The structure that corresponded to minimized energy was used to determine the equilibrium bond length. Energy values were determined at every 0.1Å for bond lengths shorter than equilibrium and at intervals of 0.2Å longer than equilibrium.

QC calculations were performed on the singlet and triplet spin states of a RbOH cluster to evaluate the energy barrier of the Rb-OH bond dissociation. From these calculations, the equilibrium bond length was 2.5 Å and the bond dissociation energy was found to be 67 kcal/mol. ReaxFF$_{KSeRb}$ was able to simulate the equilibrium bond distance and calculated a bond dissociation energy of 46.4 kcal/mol.

The K-OH bond dissociation was calculated using the same method as for Rb-OH. The equilibrium bond distance of 2.32 Å was accompanied by a 71.9 kcal/mol dissociation energy. ReaxFF$_{KSeRb}$ determined the bond dissociation to be 56.7 kcal/mol.

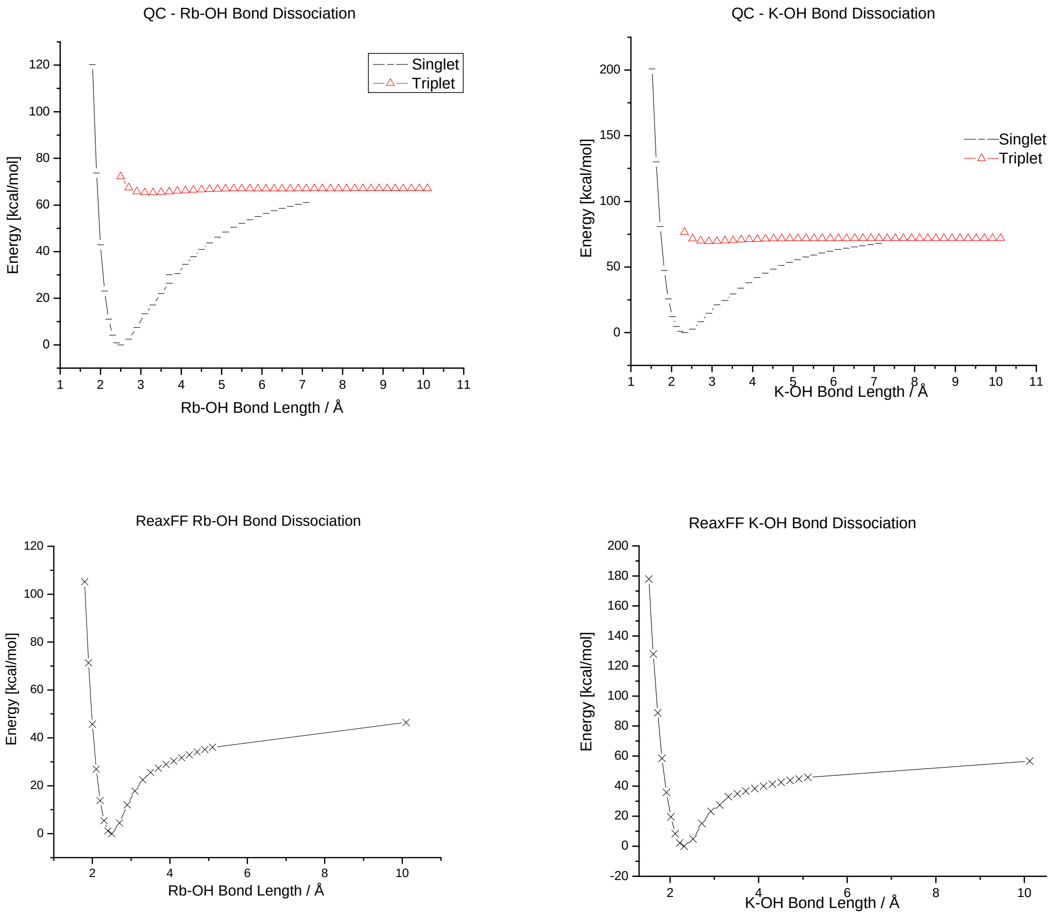

Figure A-1. Quantum Chemical and ReaxFF Rb-OH and K-OH Bond Dissociations.

A.5.3.2 Selenic acid bond dissociations

The selenic acid molecule has two distinct bonds: the Se=O double bond and the Se-OH single bond. QC calculations on higher spin states were not successful. From the data that was obtained, the equilibrium bond length for the Se-OH bond was 1.82 Å associated with a dissociation energy of 67.4 kcal/mol. The Se=O double bond was determined to be 1.65 Å with a dissociation energy of 92.9 kcal/mol. The $\text{ReaxFF}_{\text{KSeRb}}$ yielded values that exhibit a similar bond dissociation trend, however, higher spin state dissociation QC values will need to be obtained for a more accurate model. $\text{ReaxFF}_{\text{KSeRb}}$ indicated a bond dissociation energy of 48.8 kcal/mol for the single bond and 58.8kcal/mol for the double bond.

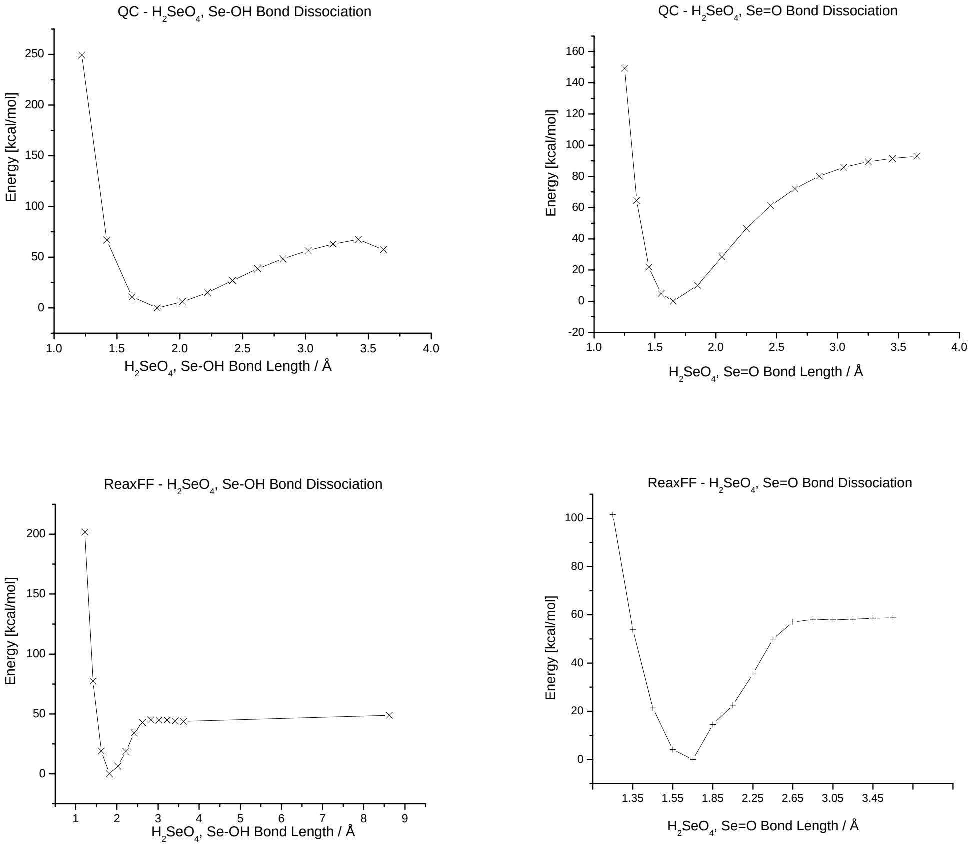

Figure A-2. Quantum Chemical and ReaxFF H_2SeO_4, Se-OH and Se=O Bond Dissociations.

A.5.3.3 Angle Bend Energies

The three bond angles in selenic acid (HO-Se-OH, O=Se-OH, O=Se=O) were explored by distorting the angle out of equilibrium in steps of 5°. ReaxFF$_{KSeRb}$ recreated similar energy vs. bond angle trends for all three angles. Around equilibrium, agreement between ReaxFF$_{KSeRb}$ and QC methods are nearly exact. At the extreme angles, agreement between these two methods was closest for the O=Se=O bond angle (21.4 kcal/mol ReaxFF$_{KSeRb}$ versus 23.5 kcal/mol QC at 163.2°, 40° out of equilibrium). The O=Se-OH bond angle distortion at 161° (55° away from eq.) has an energy of 32 kcal/mol – QC and 18 kcal/mol - ReaxFF$_{KSeRb}$. At 163.5°, the HO-Se-OH bond angle distortion has a energy discrepancy between ReaxFF$_{KSeRb}$ and QC methods of 11.8 kcal/mol (QC – 33.8 kcal/mol and ReaxFF$_{KSeRb}$ – 22.1 kcal/mol).

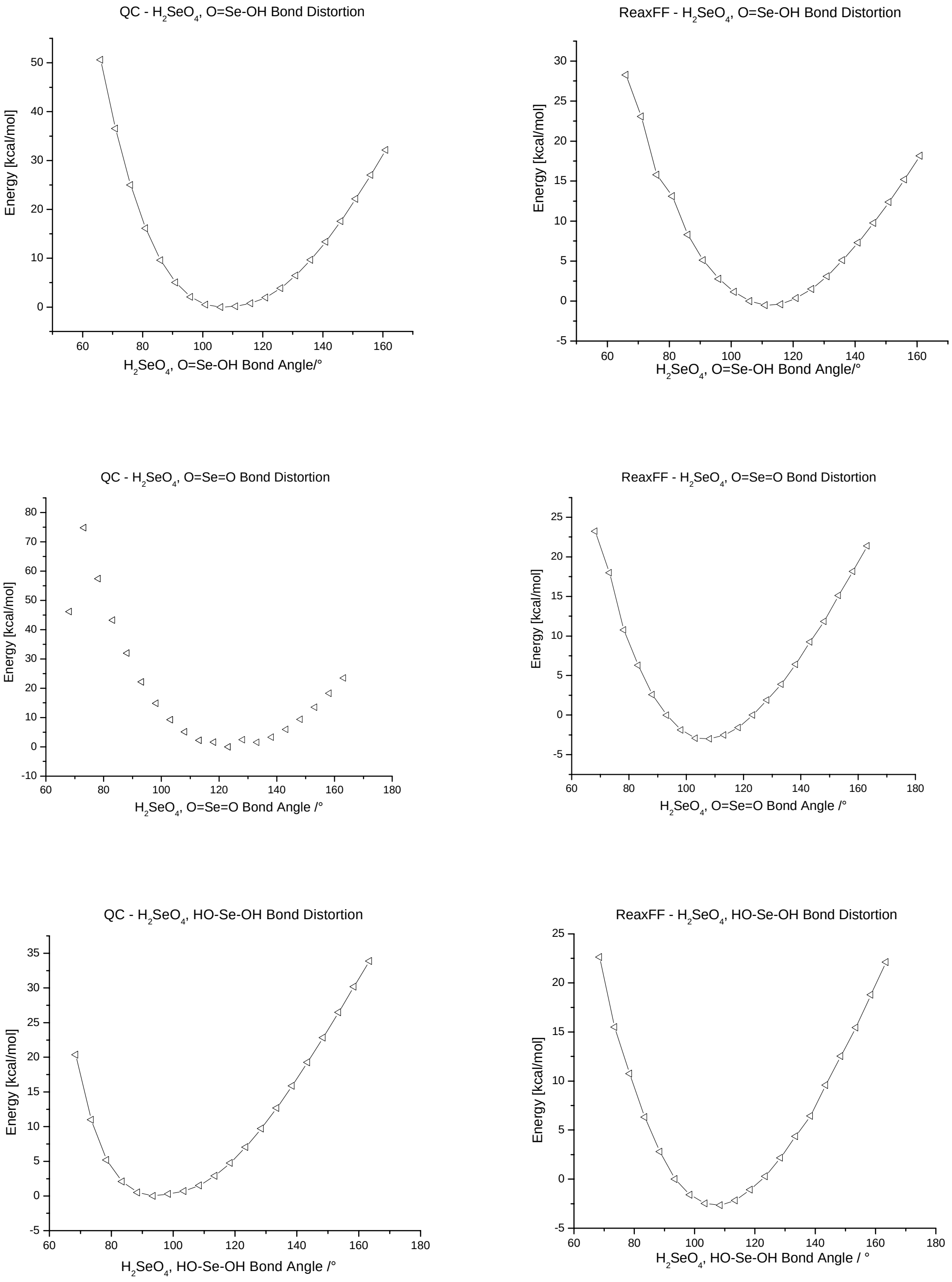

Figure A-3. Quantum Chemical and ReaxFF H_2SeO_4, O=Se-OH, O=Se=O, and HO-Se-OH Bond Angle Distortions.

A.5.3.4 Proton Migration

The energy barrier for proton migration across a $HSeO_4^-$ cluster was calculated by pulling the H atom towards one of the three equivalent oxygen atoms bonded to selenium. The $O^{\cdots}H$ distance was varied from 2.5 Å to 1 Å by 0.25Å. This was repeated in reverse to verify that the barrier was symmetric. ReaxFF$_{KSeRb}$ calculated a energy barrier of 10.6 kcal/mol while QC methods produced a 8.8 kcal.mol barrier.

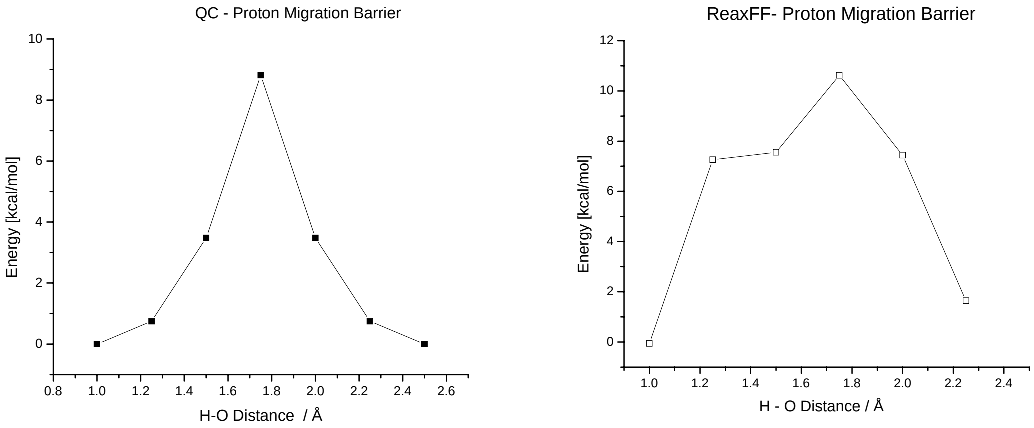

Figure A-4. Quantum Chemical and ReaxFF Proton Migration Barrier.

A.5.3.5 Crystal Data – Metals, Metal Oxides

The ReaxFF$_{KSeRb}$ potential was tested for its ability to predict phase stabilities against K, KO_2, Rb, Rb_2O, Rb_2O_2, and SeO_2 crystal structures. QC energies were obtained for compressions and expansions of several crystal systems. The FCC phase of K and Rb metal has the highest stability compared to BCC, A15, and simple cubic. ReaxFF$_{KSeRb}$ was able to reproduce this trend for K and Rb structures. ReaxFF$_{KSeRb}$

was also able to reproduce the general equation of state (EOS) for two Rb_2O structures.

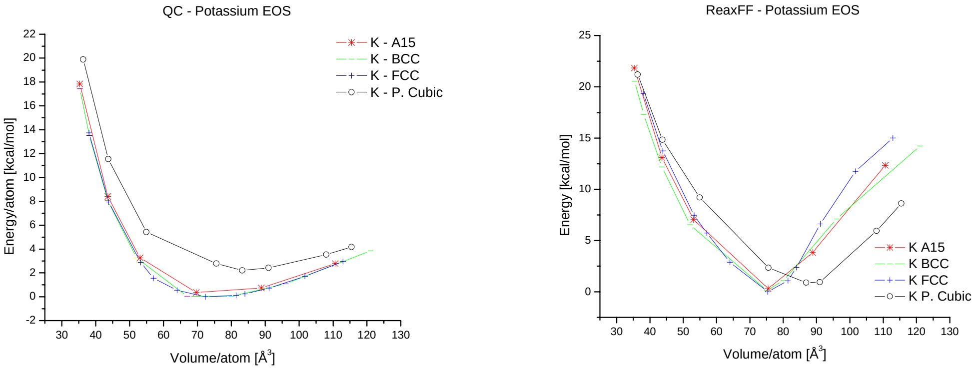

Figure A-5. Quantum Chemical and ReaxFF Equation of state for Potassium.

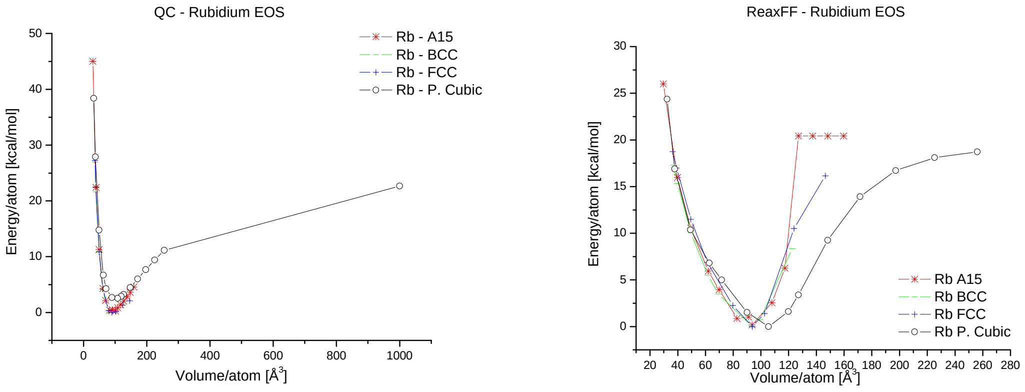

Figure A-6. Quantum Chemical and ReaxFF Equation of state for Rubidium.

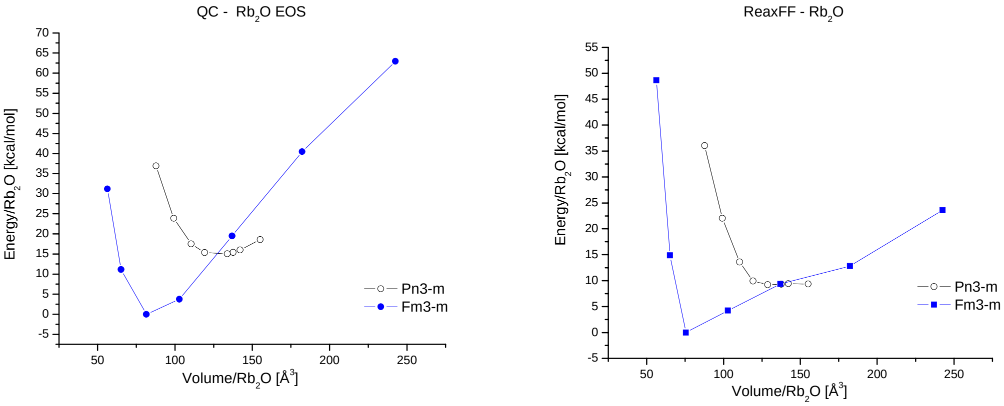

Figure A-7. Quantum Chemical and ReaxFF Equation of state for Rubidium Oxide.

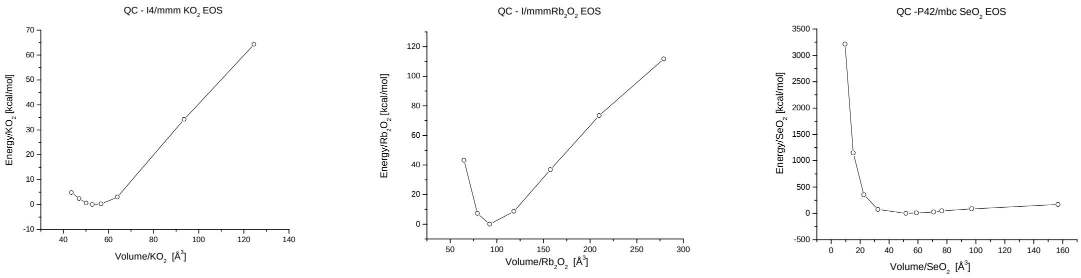

Figure A-8. Quantum Chemical Equations of state for I4/mmm KO_2, I/mmm Rb_2O_2, $P4_2$/mbc SeO_2.

A.5.4 Conclusions

The ReaxFF$_{KSeRb}$ reactive force field has been developed for rubidium and potassium hydrogen selenate systems. ReaxFF$_{KSeRb}$ has been verified on QC data comprised of clusters and condensed phases illustrating reactive and nonreactive aspects of selenic acid, potassium, rubidium and a couple oxide structures. The decent agreement between QC data and ReaxFF$_{KSeRb}$ suggests that more work needs to be done on the QC training set which is not limited to the higher spin states for the selenic acid bond dissociations or QC EOS for high temperature and room temperature structures of $RbHSeO_4$ and $KHSeO_4$.

Future work entails simulating the high temperature structures are by $\text{ReaxFF}_{\text{KSeRb}}$ methods. As experimental data is available to compare to the estimates $\text{ReaxFF}_{\text{KSeRb}}$ can provide for high temperature structures, further simulation work may be compared directly.

A.5.5 Acknowledgements:

The author wishes to express her gratitude to Adri van Duin, Yun-Hee Jang, Boris Merinov, Eugene Heifets and William A. Goddard for supporting this work.